NTNU

Norwegian University of
Science and Technology

Roll Damping Investigation of Two-Dimensional Ship Section with Bilge-Boxes

Muhammad Mukhlas

Abstract

Roll motion is considered as one of the most difficult responses to be mathematically treated, this is due to the importance of the viscous effects. Several parameters may affect the roll motion hydrodynamically. Hence, tedious parameter study needs to be involved when predicting roll motion. Model the problem with "full" Navier-Stokes methods are still considered less effective when doing design-loop, the approaches carry large computational cost even for two-dimensional case. For the conventional ship hull shape, potential flow solver with the semi-empirical formula correction that based on the extensive investigations mainly by Ikeda et al. (1976, 1977b,a, 1978) has been widely adopted by the industry. The unconventional hull shape, on the other hand, needs to rely with the model testing and/or numerical modeling.

Present study investigates the hydrodynamic coefficients of two-dimensional ship section with bilge-boxes both experimentally and numerically. The section represents one of the unconventional hull shapes, which resemble the mid-section of cylindrical floating structures. The forced oscillation equation of motion mathematical model is used to extract the hydrodynamic coefficients in roll. The coefficients are linearized by the so-called equivalent linearized form by assuming the same amount of energy loss during half cycle of roll motion. Consequently, the coefficients are presented as a function of amplitudes and period of oscillations.

The model tests were tested in Ladertanken wave flume, Norwegian University of Science and Technology. 13 forced roll amplitudes were tested at 7 roll periods. Two accelerometers were used to acquire the body motion, and another nine strain gauges to measure the total force and force on the bilge-boxes. In addition, four wave gauges were located at some distance downstream from the model to measure the generated waves system.

Tailor made of Potential Viscous Code for two-dimension roll problem, PVC2D-Roll, was chosen to solve the roll problem in present study. The computation is simplified by assuming linearized free-surface, and neglecting the nonlinear terms on the free-surface condition equations. The body-boundary condition is exact and modeled with Solid Body Rotation mesh deformation technique. This approach only needs the mesh to be fine in the bilge-boxes, hence the computational costs reduce significantly.

It is found that for relatively short bilge-boxes (BB1), PVC2D-Roll captures the quadratic damping with respect to increasing amplitude very well and starts to over predict the results for higher amplitudes. Slope changes were observed in the damping coefficients with respect to amplitude curves for longer bilge-boxes (BB2 and BB3). The results from bilge-boxes' damping coefficients suggest that free-surface effect causes damping coefficients strongly dependent on the amplitude and period.

Added-mass in roll increases with the presence of bilge-boxes. For BB1 case, the added-mass coefficient tend to show independency from oscillation amplitude and period. On the other hand, BB2 and BB3 results exhibit reduced added-mass coefficients with respect to amplitude,

while increases with increasing period. This is also believed mainly due to the viscous flow separation and free surface effect.

Preface

This thesis has been carried out under supervision of Prof. Trygve Kristiansen at the Department of Marine Technology, Norwegian University of Science and Technology. I want to thank him for introducing me to the world of roll motion, his guidance and supervision have been most appreciated. I would also want to thank my co-supervisors, Yanlin Shao and Babak Ommani, for their interest in this topic and valuable discussions.

Great helps have come from SINTEF Ocean and NTNU employees, Trond Innset, Ole Erik Vinje, Torgeir Wahl, Terje Rosten and Markus. I would also like to appreciate SINTEF stipendet for their master thesis funding, the valuable data from the force sensors really give additional insight of my thesis work.

Big appreciation goes to Indonesia Endowment Fund for Education scholarship (LPDP-RI) for their scholarship funding. This has been my dream to study in NTNU, and could not be achieved without help from people of Indonesia through this scholarship. I dedicate this thesis for my beloved country, for the development of maritime technology in Indonesia.

Many people also contribute in giving me inspiration during the work. In particular this goes to Tobias Rasen Borgenhov, my cooperating partner during this one year thesis work. His assistance in the model tests stage really help me a lot. Help also comes from my Indonesian friend, Ivana Irene Helen Adam, her help to proofread my work at the last minute before submission has been very helpful. Lastly, I would also want to present this work to my beloved people, Greatania Juardi, Akhmad Ilham Ramadhan Sabara, Nadya Hafiyya Sabara, Natsir Sabara and Raden Ayu Zawiah. Their presence has been motivated me a lot, and made me stronger.

Trondheim, June 11, 2017

Muhammad Mukhlas

Nomenclature

Abbreviations

$BB1$ Bilge-Boxes 1

$BB2$ Bilge-Boxes 2

$BB3$ Bilge-Boxes 3

CAD Computer Aided Design

$CFLR$ Courant–Friedrichs–Lewy

$FSRVM$ Free Surface Random Vortex Method

FVM Finite Volume Method

$NS2D$ 2-D Navier-Stokes Equations

PVC Potential Viscous Code

$PVC2D - Roll$ Two-Dimensional Potential Viscous Code for Roll

$RC0$ Rounded Corner

RVM Random Vortex Method

SBR Solid Body Rotation

WP Wave Probe

CFD   Computational Fluid Dynamics

DOF   Degree of Freedom

FPSO   Floating Production Storage Offloading

ITH   Ikeda-Tanaka-Himeno

Coordinate Systems

$O_e\ X_e\ Y_e\ Z_e$ Earth-fixed coordinate system

$o_g\ x_g\ y_g\ z_g$ Inertial coordinate system with origin at centre of gravity of the body

OXYZ Inertial coordinate system

oxyz Body-fixed coordinate system

Greek Letters

δ_{ij} Kronecker delta function

η_1 Surge motion

η_2 Sway motion

η_3 Heave motion

η_4 Roll motion

η_5 Pitch motion

η_6 Yaw motion

λ Young's modulus

μ Dynamic viscosity

ν Kinematic viscosity

ω Vorticity / frequency, will be mentioned in text

ϕ Potential function

ρ mass density coefficient

τ_{ij} External stress tensor

φ Generated velocity potential

Matrices

F   External force matrix

M   External moment matrix

P   Angular momentum matrix

V   Velocity matrix

Roman Letters

$\zeta(x,t)$ Free-surface elevation

A_{ij} Added-mass coefficients for the force in i-direction due to the motion in j-direction

B Beam length

B_{BK} Bilge keels damping coefficient

B_E Eddy making damping coefficient

B_e Linear equivalent damping coefficient

B_F Friction damping coefficient

B_L Lift damping coefficient

B_W Wave damping coefficient

C_D Drag coefficient

C_g Group velocity

C_{ij} Restoring coefficients for the force in i-direction due to the motion in j-direction

D Draft depth

e Internal energy per unit mass

f Frequency

g Gravity acceleration

h Water depth

I_{ij} Moment of inertia for the force in i-direction due to the motion in j-direction

k Thermal conductivity or wave number, will be mentioned in the text

KC Keulegan Carpenter number

p Thermodynamic pressure

Re Reynolds number

S Surface

$S(z,t)$ Wavemaker displacement

T Temperature

t Time

U Flow speed

Vectors

$\mathbf{u}$ Velocity vector

$\vec{\eta}$ Rigid body motion vector

$\vec{n}$ Vector normal to the surface

$\overrightarrow{Oo}$ Translatory vector

Contents

List of Figures

List of Tables

Chapter 1

Introduction

Ship responses are the most important aspect that must be determined to have a picture of performance and operability of ship in certain sea condition. Based on the linear potential theory calculation, which assuming ideal fluid condition, the ship responses are predicted reasonably well except for the roll motion. This is due to the damping components of roll motion that mainly come from viscous effect, which is not accounted in potential theory. Due to the nonlinearity that introduced by the fluid viscosity, roll motion has to be investigated by means of model test and Computational Fluid Dynamic (CFD) methods which based on Navier-Stokes equations.

Roll motion is considered as the most difficult response to be mathematically treated. Several parameters affect the motion hydrodynamically, as shown by Ommani et al. (2015) among others, where the change of parameters may give different damping coefficient. Hence, tedious parameter study needs to be involved when predicting the roll motion. The combination between potential flow solver with model test results or empirical models has been considered to be more practical and preferred by the industry. The CFD approaches are still considered less effective when doing the design-loop, the approaches carry large computational cost even for two-dimensional case. Another candidate is the hybrid method introduced by Kristiansen and Faltinsen (2012) that has been proven to reduce the computational time greatly, which only incorporates the important contributing physics from both of potential and viscous flow methods instead of resolving all aspects with CFD.

For the conventional hull type with bilge keels, the semi-empirical formula that based on the results of extensive investigations mainly by Ikeda et al. (1976, 1977a,b) has been existed and can be adopted in the design phase. The unconventional hull shape, on the other hand, needs to rely with either the model test and/or numerical modeling. One of the unconventional hull types that can be found in North Sea is the cylindrical floating structure. This body has a so-called "bilge boxes", rather than bilge keels as its damping device. Therefore, the damping feature for this particular hull shape became an interest and will be further investigated here both numerically and experimentally.

1.1 Cylindrical Floating Structure with Bilge Boxes

As explorations are going to more remote, harsher and deeper area, the needs of economical and reliable marine structures are required. Many novel concepts have been introduced as an promising technology to replace the ship-shaped Floating Production Storage Offloading (FPSO), one of them is cylindrical floating structure.
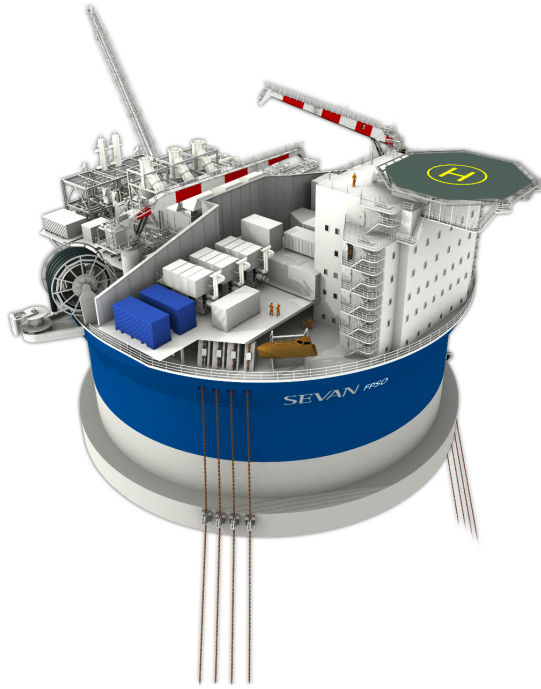
Figure 1.1: One example of cylindrical floating structure (Sevan FPSO) which is equipped with bilge boxes, bilge boxes are the white appendages in the bottom part of the structure

Many advantages are offered by this technology :

1. Symmetry design, hull facing environment with the same shape
2. High capacity of oil storage and deck loads
3. Insignificant bending stresses due to the global load on the hull
4. Excellent motion characteristics
5. Accommodates large number of risers

The bilge boxes play an important role in the hydrodynamics point of view. Firstly, the viscous effects for large floating structures are often considered as secondary, but it is not necessarily the case in the resonant regime. The viscous damping and excitation forces play an important role within the regime. The viscous damping mainly introduced by vortex shedding from the sharp corner of bilge boxes. Secondly, from the study of heave plates of semi-submersible offshore wind turbine platforms (see Moreno et al. (2016)) which has the same principle as bilge boxes, it was found that the heave plates increase the damping and detune the platform from the wave-excitation regime by introducing the changes of added

mass from the vortex shedding mechanism.

Figure 1.2: Illustration of vortex shedding mechanism introduced by the sharp corner of bilge boxes from CFD simulation

1.2   Previous related studies

The investigation of ship roll motion was started by Froude (1861) with his paper "On the Rolling of Ships", where he investigated Brunel's *Great Eastern*. After the trial voyage of the ship in 1865, the "bilge pieces" which came from his idea of the resistance importance to decrease the roll motion were happened to be successful. On the other hand, the presence of bilge keels have made the motion prediction even more difficult with the presence of viscous forces.

Mathematical models that capture physical properties of wave-body interaction with sufficient accuracy were required due to the shortage of computational capacity during 19th century. Then the concept of the so-called "Strip Theory" was introduced, which truncates the ship into several two-dimensional body and solve the problem by means of potential theory. The development of this theory had been contributed by several theoriticians, such as Ursell (1949), Denis and Pierson (1953), Korvin-Kroukovsky and Jacobs (1955), Gerritsma (1958), Tasai (1959) and Salvesen et al. (1970). All the terms in ship's equation of motion with or without forward speed in six degree of freedom (DOF) can be solved with considerable degree of accuracy, except for damping component of roll motion, which was found to be associated with viscous effects.

Due to the inability of strip theory to capture the viscous effects that mainly introduced by flow separation, research of roll motion has mainly focused on experimental method. The most notable work came from the extensive and systematic investigations of roll damping in ordinary ship hull that had been conducted in Japan from 1970 to 1979. The so-called Ikeda-Tanaka-Himeno method (ITH Method) mainly are works by Ikeda et al. (1976, 1977a,b) and summarized in Himeno (1981), and has been widely used as a state-of-the-art prediction formula for roll damping in conventional hull ship both with and without forward speed. The method gives good insight about roll damping physics, the so-called component analysis, breaks down the damping contribution into friction (B_F), eddy (B_E), lift (B_L), naked hull wave

(B_W) and bilge keels damping (B_{BK}) and investigate them separately. Interaction between the components is then assumed to be neglected and in form of linear equivalent damping (B_e). In principle, the roll damping coefficient obtained from the experiment or semi-empirical formula is further used to correct the calculation made by strip theory. Unfortunately, the formula give good agreement only to limited shapes of ship and showed discrepancies for some cases such as identified in the ship with high breadth-to-draft (B/D) ratios. The ship roll damping research then has been continued based on the experimental and numerical methods.

Complications of the ship roll damping are due to its dependency on many aspects. Geometry of the hull is among of them, and the fact was first validated by experimental investigations conducted by Vugts (1968), who discovered the dependency of wave damping to B/D ratios of rectangular ship hull for several frequencies. The wave damping was found to be very small for some range of B/D ratios, and suggests the importance of viscous effects on damping for this range. The discrepancies of hydrodynamic coefficients can also be affected by bilge radius, as shown by Yeung et al. (1998), the added-mass coefficients found to be saturated due to "rounding effects" which was not found in Vugts (1968). One of the experimental and numerical studies of comparison between two-dimensional ship section was done for rounded, sharp and step corner bilge by Yuck et al. (2003), results suggest the different viscous damping from all the three sections with step model and rounded model became the most and least significant respectively. Circular cylinder hull shape with the center of rotation being in the middle of the circle is also well known for no capability in generating waves, as demonstrated by Ommani et al. (2016b) based on experimental data by van't Veer et al. (2015), the drag coefficients (C_D) of bilge keel attached to circular hull are independent of draft and consequently no free surface effect.

Damping due to the bilge keels also has become the most attention within roll motion study. Hydrodynamic effects of bilge keels length and also the attachment position has been investigated, and in general shows roll damping increment with respect to roll amplitude, this is mainly due to the relative velocity between the body motion and fluid which dictates the strength of flow separation. One interesting study of bilge keels was conducted by Thiagarajan and Braddock (2010), they show that damping coefficient saturates for sufficiently long bilge keels. They indicate that for longer bilge keels, the flow separated from bilge keels tip is convected away from the vortex rich region near the hull and consequently the vortex interaction is reduced. Comparison between vertical and horizontal bilge keels was studied by Yu et al. (2005). The added mass coefficients are the same for both configurations, but larger damping for the horizontal bilge keels. This is believed due to the fact that horizontal bilge keels being closer to the free-surface, and that affects the free surface and consequently a larger damping coefficients. Many more studies on hydrodynamics of bilge keels / thin plate oscillating in harmonically flow has been investigated up until now, and Keulegan and Carpenter (1958) are among the one that started this particular research. They established a parameter that indicates the importance of drag force relative to the inertia force based on the free plates experiment in the oscillating current, the so-called KC number, which dictates

the flow topology. The findings are later extended by the study from Sarpkaya and O'Keefe (1996), they investigated the importance of added-mass with the presence of wall based on the bilge keels experiment exposed to oscillating flow in a large U-shaped water tunnel. They also identified significant changes of flow topology and categorized the into three region: KC<1.5, 1.5<KC<4 and KC>4.

Based on the discussion above, it is not surprising if the development of roll damping prediction is conveted to be resolved by numerical methods. One of the numerical approaches which incorporate vortex is the so-called vortex method. Several renowned works related to this area are Vortex Sheet Model by Faltinsen and Pettersen (1987), Discrete Vortex Method by Sarpkaya and Shoaff (1979), Single Vortex Method by Faltinsen and Sortland (1987) and many others. One renowned work of the problem involving flow separation from the body with sharp corners is Random Vortex Method (RVM) (see Yeung et al. (1996, 1998, 2001)).

The increase of computational capacity lately caught the interest of many researchers to solve the problem by means of CFD. CFD was first used for aerodynamics in the airplane, and recently followed by marine industry. Roll motion is one of the marine related problems that can be solved by means of CFD. Today's common practice in industry is to extract the two-dimensional hydrodynamic coefficients from the comparison of both experiments and CFD simulations, and apply the corresponding coefficients to the strip-theory based program. Many different techniques have been used, but the goal is still to approach the Navier-Stokes equations. Some of the works are dedicated to solve ship's roll motion are listed here, but not limited to, Yu et al. (2005) who developed the 2-D Navier-Stokes equations (NS2D), Jaouen et al. (2011) from MARIN on their validation study of in-house code called ReFRESCO, Kristiansen et al. (2014) investigation on the ship with and without bilge keels using the commercial StarCCM+ CFD code, Irkal et al. (2016) study on free decay roll motion with Flow-3D commercial code, and many others.

Latest candidate to resolve the roll motion problem is the hybrid method called Potential Viscous Code (PVC) that developed in Department of Marine Technology, Norwegian University of Science and Technology. It was originated from the investigation of moonpool resonance problem in Kristiansen and Faltinsen (2012) which was later extended in Kristiansen et al. (2013). The method is combining both of the Navier-Stokes and potential flow methods, and solve the important physics of the problem with the combination of both methods. Tailor made version of the code has been developed to solve the roll motion problem of the body with sharp corner, the so-called PVC2D-Roll, which has been under validation studies (see Ommani et al. (2015, 2016b,a)).

1.3 Present study

In the present study, roll in the two-dimensional cylindrical floating structure section equipped with bilge boxes has been investigated both numerically and experimentally. Scale effects on

the model test are considered to be minor importance, since the flow separation occurs from the sharp corners of the model. Both of the present methods has been utilized to complement each other, with the ultimate goal is to establish the correct numerical code to approach the problem. On the other hand, the experimental results cannot be considered as the true solution, and one needs to have critical mind to analyze the bias errors that may occur in the experiment setup.

1.3.1   Statement of problems

The idea of studying some particular unconventional body has been proposed as a master thesis topic, which has the ambition to answer the formulated problems comprise of:

1. How does bilge-boxes that added to a conventional ship shape influence the damping of pure rigid body roll motion?
2. How is the forces of bilge boxes in the case of pure rigid body roll motion?

1.3.2   Limitations and objectives

The study is limited to the two-dimensional body in the still water, without forward speed, wind and current. The motivation of using two-dimensional case is for having detailed and controlled observation of physics and the possibility to extend the study into three-dimensional case in the future. The information obtained of this study will be valuable as a reference regarding the bilge boxes performance in roll motion.

Based on that fact and also the problem formulation, the objectives of present study are:

1. Give an overview of previous work about roll motion both experimentally and numerically
2. Present basic theory that focus on ship motions, wave-fluid interaction in the potential and viscous flow theory
3. Parameter study with the emphasize on the effect of varying bilge boxes length on roll damping with respect to the pure rigid body roll motion has to be done both numerically and experimentally
4. Construct and perform two-dimension forced roll motion model test in the narrow flume tank
5. Perform the numerical study using PVC2D-Roll with identical case as the model test
6. Analyze the obtained forces experienced by the bilge boxes during rigid body roll motion both numerically and experimentally

1.3.3   Structure of the thesis

The structure of the thesis is as follows. Chapter 2 is emphasized on the mathematical formulation of the ship motion, fluid governing equations and also the existed mathematical model to resolve the roll motion.

In Chapter 3 the numerical model that used in the present study is discussed. The information of the basics of numerical approaches, governing equations discretization schemes, convergence studies, and also PVC2D-Roll numerical schemes are briefly discussed.

The model tests construction are presented in Chapter 4, including the mechanical mechanisms, instrumentation, data analysis procedures and finally the discussion of error sources.

In Chapter 5 the results from model tests and PVC2D-Roll are presented and compared. The hydrodynamic damping and added-mass coefficients are evaluated with respect to the bilge-boxes length, roll amplitudes and periods. The analysis of forces and hydrodynamic on bilge-boxes and the comparison with the results from other people works has been endeavored.

Finally, the summary and recommendation to further works is given in Chapter 6.

Chapter 2

Mathematical Model

2.1 General

The problem that will be discussed within this chapter is the quantification of dynamic equilibrium of ship in waves. The most practical and efficient method that has been widely used within ship motion prediction field is strip method that based on linear potential flow theory (see Salvesen et al. (1970) for instance). The main advantages of using the method is the utilization of superposition principle, meaning that the problem can be decomposed into several cross-sections and fundamental effects which can be solved separately.
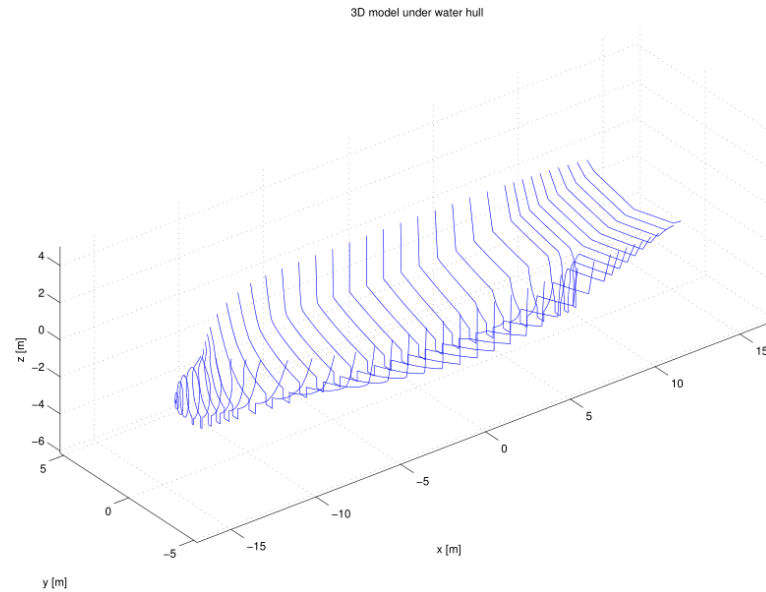
Figure 2.1: Illustration of strip theory that has been commonly used for predicting ship motion (Martinussen (2011))

If one assumes that the problem is linear, the complex seakeeping problem can be divided into two sub-problems that are much more easier and controlled, i.e. radiation and diffraction problems.
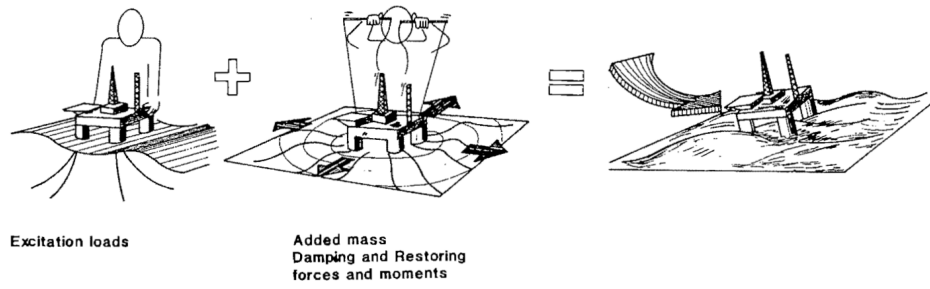
Figure 2.2: Subdivision of wave-body interaction problem from Faltinsen (1993)

1. Radiation problem; the hydrodynamic forces induced by the harmonically oscillating rigid body in the undisturbed surface of an ideal fluid
2. Diffraction problem; the excitation forces that come from the waves to the restrained rigid body

Specifically for the roll motion of ship, which does not hold linearity in nature, the additional empirical formulation (see Himeno (1981)) is usually added to the strip method-based computer program. Recently, the CFD method has also been involved to resolve the complexity of the roll motion which is promising with the development of today's computer.

This chapter is specifically made to give brief information to the reader about the linear two-dimensional surface piercing rigid body forced roll motion. The emphasize of discussion in present study is given to sub-problem 1, hence sub-problem 2 will not be discussed. One may refer to Faltinsen (1993) for more complete description.
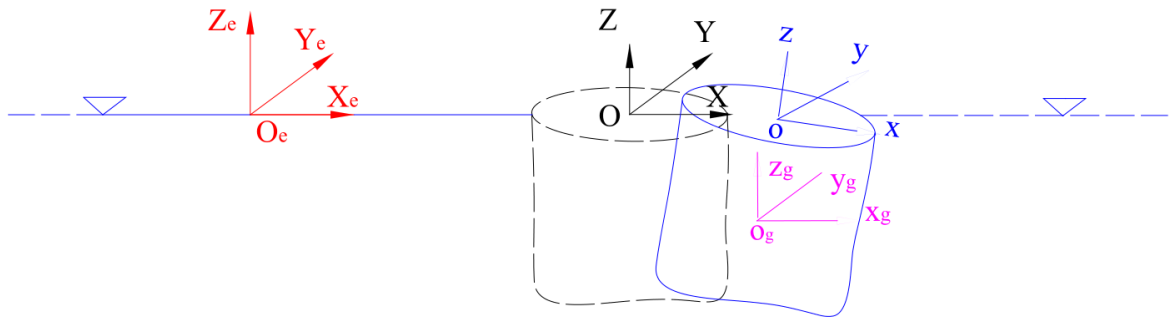
Figure 2.3: Four different coordinate systems that adopted from Shao (2010)

For clarity, four right-handed Cartesian coordinates are defined as reference and will be used throughout the document. All coordinates are illustrated in Fig. 2.3. $O_e X_e Y_e Z_e$ is Earth-fixed coordinate system with the origin at the mean water surface and positive upward, $OXYZ$ is an inertial coordinate system moving with steady forward speed, $oxyz$ is a body-fixed coordinate system with steady and unsteady rigid-body motions of the body, and $o_g x_g y_g z_g$ is an inertial coordinate system with origin at centre of gravity of the body.

2.2   Motion definition

The following derivation is a summary from Shao (2010), for a complete description one may refer to his work.

The description of translatory and oscilatory motion vector can be described in oxyz and o_g x_g y_g z_g relative to the inertial coordinate system OXYZ. For instance for translatory vector $\overrightarrow{Oo}$, it can be described by $\overrightarrow{\eta} = (\eta_1, \eta_2, \eta_3)$ with η_1, η_2, η_3 are surge, sway and heave respectively. The angular displacement (Eulerian angles) will be defined as three subsequent rotations with the centre of angular motion is the origin of OXYZ as roll α_4, pitch α_5, and yaw α_6 (see Fig. 2.3).
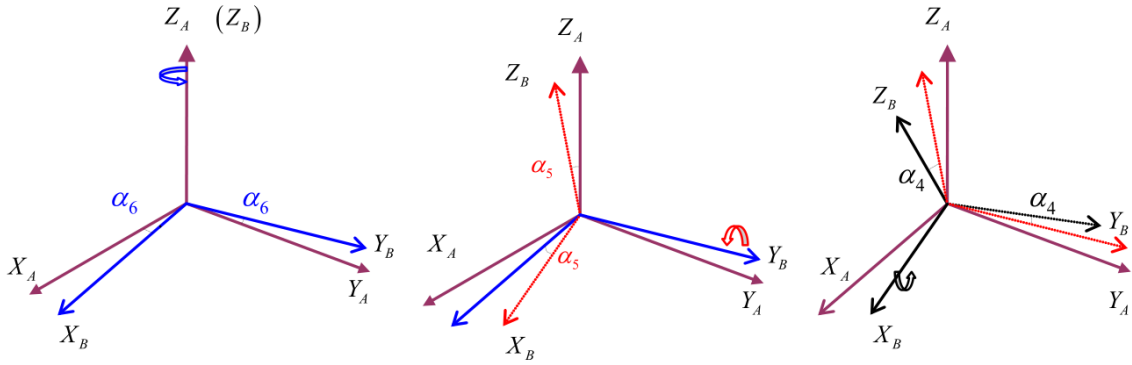
Figure 2.4: The Eulerian angles description adopted from Shao (2010). The rotation α_5 and α_4 is taken from updated axis $X_B Y_B Z_B$

Consequently, the vector transformation description from one reference frame to another can be described by the following form (see Fig. 2.4 for the illustration).

$$\overrightarrow{r_B} = \overrightarrow{O_B O_A} + \mathbf{R}_{A \to B} \overrightarrow{r_A} \tag{2.1}$$

$$\mathbf{R}_{A \to B} = \mathbf{ABC} \tag{2.2}$$

where

$$\mathbf{A} = \begin{bmatrix} cos(\alpha_6) & -sin(\alpha_6) & 0 \\ sin(\alpha_6) & cos(\alpha_6) & 0 \\ 0 & 0 & 1 \end{bmatrix}, \mathbf{B} = \begin{bmatrix} cos(\alpha_5) & 0 & sin(\alpha_5) \\ 0 & 1 & 0 \\ -cos(\alpha_5) & 0 & cos(\alpha_5) \end{bmatrix}, \mathbf{C} = \begin{bmatrix} 1 & 0 & 0 \\ 0 & cos(\alpha_4) & -cos(\alpha_4) \\ 0 & cos(\alpha_4) & cos(\alpha_4) \end{bmatrix} \tag{2.3}$$

It is interesting to note that the product of $\mathbf{R}_{A \to B}$ and $\mathbf{R}_{B \to A}$ is an identity matrix.

The advantage of using the rotation definition in terms of Fig. 2.4, as also explained in Vugts (1970), is due to the character of the motion of ship, which the yaw and pitch amplitudes

are usually small while having considerably larger roll amplitude. If one define the oscillatory motion description in the inertia reference frame as roll η_4, pitch η_5 and yaw η_6, it can be mathematically stated that

$$\eta_4 = \alpha_4 cos(\alpha_5)cos(\alpha_6) - \alpha_5 sin(\alpha_6) \approx \alpha_4 \tag{2.4}$$

$$\eta_5 = \alpha_4 cos(\alpha_5)cos(\alpha_6) + \alpha_5 cos(\alpha_6) \approx \alpha_5 \tag{2.5}$$

$$\eta_6 = -\alpha_4 sin(\alpha_5) + \alpha_6 \approx \alpha_6 \tag{2.6}$$

Another simplification can be made by assuming the Euler angles are small, the transformation matrix is approximated by series of expansion:

$$\mathbf{R}_{A \to B} = \mathbf{I} + \mathbf{R}^{(1)}_{A \to B} + \mathbf{R}^{(2)}_{A \to B} + O(\varepsilon^3) \tag{2.7}$$

Meaning that if one wants to transform from body fixed reference frame oxyz and/or o_g x_g y_g z_g (subscript b) to inertial reference frame OXYZ (subscript i),

$$\mathbf{R}_{b \to i} = \mathbf{I} + \mathbf{R}^{(1)}_{b \to i} + \mathbf{R}^{(2)}_{b \to i} + O(\varepsilon^3) \tag{2.8}$$

where

$$\mathbf{I} = \begin{bmatrix} 1 & 0 & 0 \\ 0 & 1 & 0 \\ 0 & 0 & 1 \end{bmatrix} \tag{2.9}$$

$$\mathbf{R}^{(1)}_{b \to i} = \begin{bmatrix} 0 & -\alpha_6^{(1)} & \alpha_5^{(1)} \\ \alpha_6^{(1)} & 0 & -\alpha_4^{(1)} \\ -\alpha_5^{(1)} & \alpha_4^{(1)} & 0 \end{bmatrix} \tag{2.10}$$

$$\mathbf{R}^{(1)}_{b \to i} = \begin{bmatrix} 0 & -\alpha_6^{(2)} & \alpha_5^{(2)} \\ \alpha_6^{(2)} & 0 & -\alpha_4^{(2)} \\ -\alpha_5^{(2)} & \alpha_4^{(2)} & 0 \end{bmatrix} + \begin{bmatrix} -\frac{1}{2}\left[(\alpha_5^{(1)})^2 + (\alpha_6^{(1)})^2\right] & \alpha_4^{(1)}\alpha_5^{(1)} & \alpha_4^{(1)}\alpha_6^{(1)} \\ 0 & -\frac{1}{2}\left[(\alpha_4^{(1)})^2 + (\alpha_6^{(1)})^2\right] & \alpha_5^{(1)}\alpha_6^{(1)} \\ 0 & 0 & -\frac{1}{2}\left[(\alpha_4^{(1)})^2 + (\alpha_5^{(1)})^2\right] \end{bmatrix} \tag{2.11}$$

Hence, the description of motion in Earth-fixed inertia coordinate can be obtained. The linear

part of motion then can be stated as:

$$\vec{r_i} = \begin{bmatrix} s_1 \\ s_2 \\ s_3 \end{bmatrix} = \overrightarrow{O_iO_b} + \begin{bmatrix} \eta_1 - y\eta_6 + z\eta_5 \\ x\eta_6 + \eta_2 - z\eta_4 \\ -x\eta_5 + y\eta_4 + \eta_3 \end{bmatrix} \tag{2.12}$$

As clearly stated in Eq. 2.12 above, when one assumes small motion and linear, the motion can be described by the superposition of the rigid body motion in six DOF. The corresponding velocities and accelerations can be obtained by derivatives and double derivatives of the motions respectively.

2.3 Excitation-response relations for linear system

In a realistic sea condition, ship is subjected to the irregular waves. One way to determine the response of such dynamic system is to describe the response of the system to the deterministic (non-random) excitation. One bold assumption is to consider linear system, for which each response corresponds to the excitation by a linear differential equation. Since the equation is linear, hence the superposition principle applies. For instance if $y_1'(t)$ is the response to an excitation $x_1'(t)$ and $y_1''(t)$ is the response to the $y_1''(t)$, then the response to the combined $x_1'(t) + x_1''(t)$ is $y_1'(t) + y_1''(t)$. This assumption may only apply for relatively small displacements from equilibrium, which hold true in many cases of ship motions.
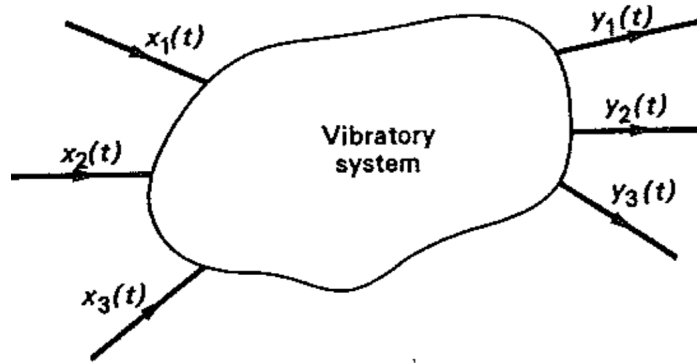
Figure 2.5: Description of linearity in a vibratory system, where the specific response corresponds to the specific excitation Newland (2005)

The well known linear differential equation that relates $y(t)$ and $x(t)$ take form

$$a_n \frac{d^n y}{dt^n} + a_{n-1} \frac{d^{n-1} y}{dt^{n-1}} + ... + a_1 \frac{dy}{dt} + a_0 y = b_r \frac{d^r x}{dt^r} + b_{r-1} \frac{d^{r-1} x}{dt^{r-1}} + ... + b_1 \frac{dx}{dt} + b_0 x \tag{2.13}$$

where a and b are functions of time in general, but may also be considered as constant for the vibrating system that does not change its characteristic with time.

The benefits of assuming such a linear system are:

1. **if** the irregularity of sea condition can be represented by the sum of sinus (harmonic) function as a propagating waves (linear waves theory), then the analysis can be separated for each harmonic excitation. Sum of all the corresponding responses will yield the system responses in irregular waves

2. the so-called frequency domain analysis can be utilized, due to the constant ratio between response and excitation amplitudes in some particular frequency

3. the excitation force can be divided into radiation and diffraction problems (see Fig. 2.2)
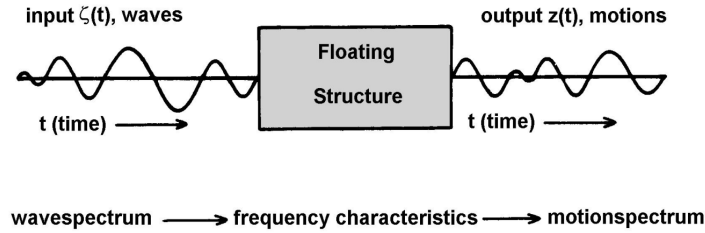
Figure 2.6: Linear relationship between irregular waves excitation and the corresponding responses Journée and Massie (2001)

The motion of an arbitrary rigid body due to some particular excitation can be described by Newton's second law which states the proportionality between momentum of a body with the force applied, and the change of momentum takes place in the direction of the applied force. His statement can be represented in a space fixed system as vector equations in a form of

$$\frac{d}{dt}(m\mathbf{V}) = \mathbf{F} \tag{2.14}$$

$$\frac{d}{dt}(\mathbf{P}) = \mathbf{M} \tag{2.15}$$

where m is the mass of the body, $\mathbf{V}$, $\mathbf{F}$, $\mathbf{P}$, and $\mathbf{M}$ are velocity, external force, angular momentum, and external moment vectors respectively. The mass and its distribution is considered to be constant during a long interval compared to the period of motions.

As a consequence of linear system assumption, the $\mathbf{F}$ and $\mathbf{M}$ vectors is assumed to be separated into two forces; radiation forces and diffraction forces (see Fig. 2.2). Hence the vectors will take form of

$$\mathbf{F} = \mathbf{F_R} + \mathbf{F_D} \tag{2.16}$$

$$\mathbf{M} = \mathbf{M_R} + \mathbf{M_D} \tag{2.17}$$

with the subscripts R and D stand for radiation and diffraction forces.

2.4 Hydrodynamic and hydrostatic forces

As discussed in Section 2.3, the ship motion can be analyzed for each harmonic due to linearity assumption. The reactive forces on the ship due to its harmonically movement can be divided into two parts: hydrostatic and hydrodynamic forces.
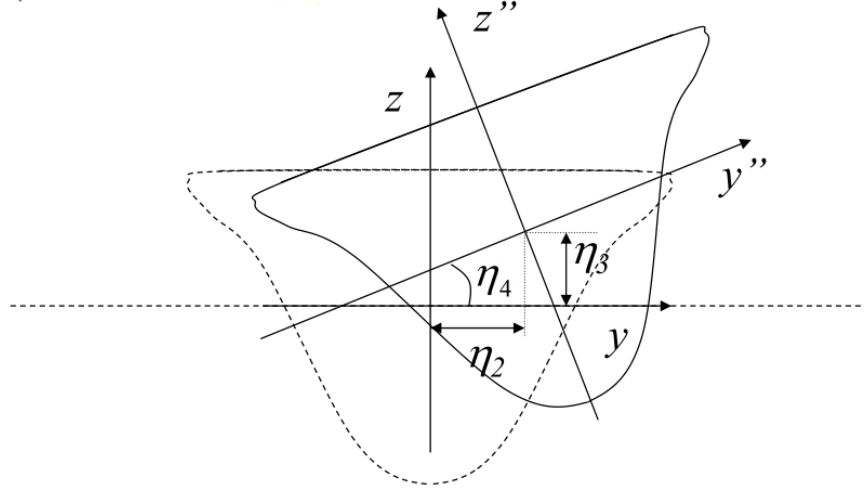
Figure 2.7: Illustration of the changes of submergence part of the body due to roll, sway and heave, which may cause the hydrostatic forces (Greco (2012))

The mean buoyancy of the ship can be assumed to be balanced by its body weight. In the case of rigid body motions, the changes of submerged part of the body create restoring forces/moments due to the pressure differences (see Fig. 2.7). The forces are linear, which are connected to the hydrostatic pressure $p = -\rho g z$, and proportional to the displacement and/or rotation of the body. The forces can be expressed by:

$$F_i = -\sum_{j=1}^{6} C_{ij}\eta_j \tag{2.18}$$

The forced body motion results in oscillating fluid field around the body. The integration of fluid pressures over the body surface gives the hydrodynamic forces and moments. They can be thought as one component in phase with the body velocity and the another one in phase with the body acceleration. They are called damping force and added-mass force respectively, with the corresponding formula:

$$F_i = -\sum_{j=1}^{6} (A_{ij}\ddot{\eta}_j + B_{ij}\dot{\eta}_j) \tag{2.19}$$

In order to find the pressure field and fluid motion, the fluid governing equation should be defined depending on the case of interest. The discussion regarding this topic will be provided in the next Section.

2.5 Fluid governing equations

According to Faltinsen and Timokha (2009), the fluid governing equations can be divided into two methods; Navier-Stokes methods and potential flow methods. The so-called hybrid methods are also available, which combine the potential flow and Navier-stokes methods, e.g. Potential Viscous Code by Kristiansen and Faltinsen (2012). Next Sub Sections will discuss the derivation for both of potential flow and Navier-Stokes methods. Both of them are described in the Earth-fixed inertia reference frame (see Fig. 2.3).

2.5.1 Navier-Stokes methods

This Sub Section gives the brief summary of the Navier-Stokes equations derivation. For the detailed derivation, one may refer to White (2005).

The flow evolution is described by three unknown parameters that vary in space and time; velocity vector $\mathbf{V}$, thermodynamic pressure p and temperature T. By considering uniform and homogeneous composition of fluid, one of the methods to derive the flow equations is to consider the laws of conservation for physical systems in Eulerian description:

1. Conservation of mass (continuity)

$$\frac{D\rho}{Dt} + \rho \ div \ \mathbf{V} = 0 \tag{2.20}$$

2. Conservation of momentum (Newton's second law)

$$\rho\frac{D\mathbf{V}}{Dt} = \rho\mathbf{g} + \nabla\tau_{ij} \tag{2.21}$$

where τ_{ij} is the external stress tensor, which describes the external stress on the sides of element. The body force $\mathbf{g}$ in here is the force that acts on entire mass of element and is assumed only gravity force that works on the system.

3. Conservation of energy (first law of thermodynamics)

$$\rho\frac{De}{Dt} = div(k\nabla T) + \tau_{ij}\frac{\partial u_i}{\partial x_j} \tag{2.22}$$

where e and k are internal energy per unit mass and the thermal conductivity respectively.

Eq. 2.20 and 2.21 are independent of T. If one interest only with p and $\mathbf{V}$, which is the case in this particular study, those two equations are sufficient to be further utilized.

Analogue with Hookean elasticity, Stokes (1845) made assumption of the linear relationship between fluid viscous stress and strain rate with μ (dynamic viscosity) as a constant of proportionality. The other considerations are the fluid is isotrophic (mechanical properties are independent of direction of implication) and the deformation law is reduced into hydrostatic pressure condition when the strain rates are zero. The fluids that obey this are categorized as Newtonian fluid. Consequently, the external stress tensor term in Eq. 2.21 can be represented in terms of velocity-gradient by viscous deformation-rate law, with δ_{ij} is Kronecker delta function.

$$\tau_{ij} = -p\delta_{ij} + \mu\left(\frac{\partial u_i}{\partial x_j} + \frac{\partial u_j}{\partial x_i}\right) + \delta_{ij}\lambda \ div \ \mathbf{V} \qquad (2.23)$$

For the Newtonian fluid, the famous Navier-Stokes equations are obtained by substituting Eq. 2.23 into Eq. 2.21. Which in vector form can be written as:

$$\rho\frac{D\mathbf{V}}{Dt} = \rho\mathbf{g} - \nabla p + \frac{\partial}{\partial x_j}\left[\mu\left(\frac{\partial u_i}{\partial x_j} + \frac{\partial u_j}{\partial x_i}\right) + \delta_{ij}\lambda \ div \ \mathbf{V}\right] \qquad (2.24)$$

If one later assumes incompressible fluid with constant viscosity coefficient, which in most cases water is incompressible, the density term in continuity equation (Eq. 2.20) will be regarded as constant both of in time and space.

$$\nabla \ \mathbf{V} = 0 \qquad (2.25)$$

Finally, the Navier-Stokes equation for Newtonian and incompressible fluid, which the governing equations for this method, can be represented as

$$\rho\frac{D\mathbf{V}}{Dt} = \rho\mathbf{g} - \nabla p + \mu\nabla^2\mathbf{V} \qquad (2.26)$$

2.5.2   Potential flow Methods

The potential flow model is one of the simplest flow models, which assuming the ideal fluid (inviscid and incompressible) and irrotational. The derivation will be discussed within this sub-section.

The concept of ideal fluid comes from the comparison of the importance between inertia forces and viscous forces that can be represented by Reynolds number Re, which in most of marine hydrodynamics problems deal with bulk body (B $\geq$ 1 meter) with the flow speed U greater

than 1 m/s.

$$Re = \frac{UL}{\nu} = \frac{inertia\,forces}{viscous\,forces} \tag{2.27}$$

The kinematic viscosity ν for the water is 10^{-6} m^2/s, and clearly shows the dominance of the inertia force. By neglecting the viscosity term in 2.26, the equations are reduced into first order PDE the so-called Euler equations.

$$\rho \frac{D\mathbf{V}}{Dt} = \rho \mathbf{g} - \nabla p \tag{2.28}$$

Furthermore, the explanation regarding irrotational fluid assumption can better be explained by taking the curl of the Eq. 2.28. The resulting equations are described in vector form as:

$$\frac{D\omega}{Dt} = (\omega.\nabla)\mathbf{V} \tag{2.29}$$

with ω being a vorticity vector. Eq. 2.29 above explains that by following fluid particle, the vorticity is conserved. Meaning that if one assumes irrotational fluid ($\omega = 0$), the fluid always irrotational in space and time. From that relation and mathematical trick, the scalar ϕ (potential function) can be used to describe the fluid velocity in space and time.

$$\omega = \nabla \times \mathbf{V} = \nabla \times \nabla\phi = 0 \tag{2.30}$$

where

$$\mathbf{V} = \nabla\phi = \frac{\partial\phi}{\partial x}\mathbf{i} + \frac{\partial\phi}{\partial y}\mathbf{j} + \frac{\partial\phi}{\partial z}\mathbf{k} \tag{2.31}$$

Compare to the Navier-Stokes method, this method is much easier to solve. The pressure term and potential function are uncoupled. The velocity field of this method is governed by continuity equation Eq. 2.25, which resulting in the so-called Laplace equation.

$$\nabla \cdot \mathbf{V} = \nabla \cdot \nabla\phi = \nabla^2\phi \tag{2.32}$$

The pressure term can be determined by using Euler equations 2.28 with the obtained velocity field.

$$p = -\rho \left[\frac{\partial\phi}{\partial t} + \frac{1}{2}|\nabla\phi|^2 + gz \right] + C \tag{2.33}$$

Equation above is well known as Bernoulli equations, and it is valid for unsteady or steady

potential flow fluid. C in Eq. 2.33 can be related to the ambient pressure or atmospheric pressure.

The advantage of using the potential flow method is the superposition principles may apply. Meaning that the simple potential elements, as long as they satisfy Laplace equation, can be superimposed to describe more complex flow. For further information regarding this, one may refer to White (2010).

2.6   Roll motion

All the motion definitions in Section 2.2 are naturally coupled to each other. Advantage of having starboard-port sides symmetry, as also stated by Salvesen et al. (1970), is that the surge-heave-pitch motions can be decoupled from sway-yaw-roll motions. In beam sea without waves, the sway-yaw-roll can be mathematically formulated by substituting Eq. 2.19 into Eq. 2.14 and 2.15. The corresponding formula are:

$$\sum_{j=4}^{6} M_{kj}\ddot{\eta}_j = F_{rad,k} \text{ for k=4..6} \tag{2.34}$$

if pure roll motion is considered, Eq. 2.34 are reduced into:

$$\left(I_4 + A_{44}\right)\ddot{\eta}_4 + B_{44}\dot{\eta}_4 + C_{44}\eta_4 = F_4 \tag{2.35}$$

Eq. 2.35 above only applies for linear system. As shown by Vugts (1968), for a certain beam to draught ratio of the ship, the two-dimensional roll wave damping $B_{44}^{(2D)}$ will be very small (see Fig. 2.8). This is explained in Faltinsen (1993), mainly because of the pressure forces cancellation between the pressure forces from the ship sides with the one from ship bottom.

Therefore, it becomes an importance to predict the viscous roll damping. In practice, for conventional hull with/without bilge keels, Eq. 2.35 can be modified by introducing the nonlinear term in the damping force as to account viscous effects.

$$\left(I_4 + A_{44}\right)\ddot{\eta}_4 + B_{44}(\dot{\eta}_4) + C_{44}\eta_4 = F_4 \tag{2.36}$$

with the $B_{44}(\dot{\eta}_4)$ term can be represented as a series of expansion in form of:

$$B_{44}(\dot{\eta}_4) = B_1\dot{\eta}_4 + B_2\dot{\eta}_4|\dot{\eta}_4| + B_3\dot{\eta}_4^2 + ... \tag{2.37}$$

Above equations are difficult to solve and involve tedious iterations. One of the methods is to replace the nonlinear term with the equivalent linearized damping coefficient, which assuming
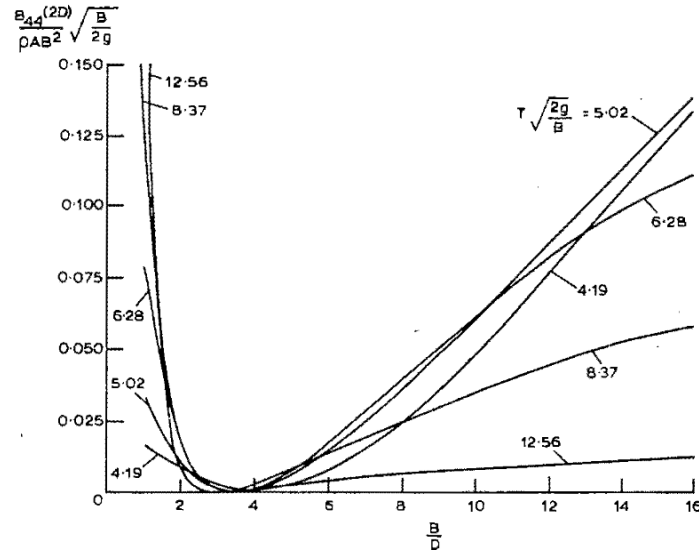
Figure 2.8: Two-dimensional roll wave damping $B_{44}^{(2D)}$ with varying beam to draught ratio and period of oscillations for rectangular cross-sections (Vugts (1968))

the same amount of energy loss due to damping during half cycle of roll motion. For simple harmonic motion the equivalent linear damping (B_e) becomes :

$$B_e = B_1 + \frac{8}{3\pi}\omega\eta_{4a}B_2 + \frac{3}{4}\omega^2\eta_{4a}^2 B_3 \tag{2.38}$$

which are the function of roll frequency and amplitude.

2.7 Radiated wave field in numerical tank

When the water is assumed as an ideal fluid and irrotational, the potential flow velocity ϕ can be used to describe the fluid field in space and time (see Section 2.5.2). This assumption has been proven to be practical for solving wide range of hydrodynamic problem, including free surface waves. According to Falnes (2002), two-dimensional radiated wave field in beam condition created by oscillating body in potential flow theory can be described by the superposition of waves created by each DOF.

$$\phi = \sum_{j=1}^{3} u_j \varphi_j \tag{2.39a}$$

$$u(z,t) = u_0 c(z) e^{i\omega t} \tag{2.39b}$$

$$\varphi(x,z) = X(x)Z(z) \tag{2.39c}$$

where u_0 and φ_j are the oscillation amplitude and the generated velocity potential by the

body oscillation in j^{th} DOF. Furthermore, the principle of variables separation is employed on $\varphi(x, z)$ to solve the Laplace equation:

$$X(x) = c_x e^{ikx} + c_{-x} e^{-ikx} \tag{2.40a}$$

$$Z(z) = c_+ e^{kz} + c_- e^{-kz} \tag{2.40b}$$

The wave generation mechanism by the body oscillation can be thought as a bottom hinged flap or a piston wavemaker for roll and sway motion respectively.
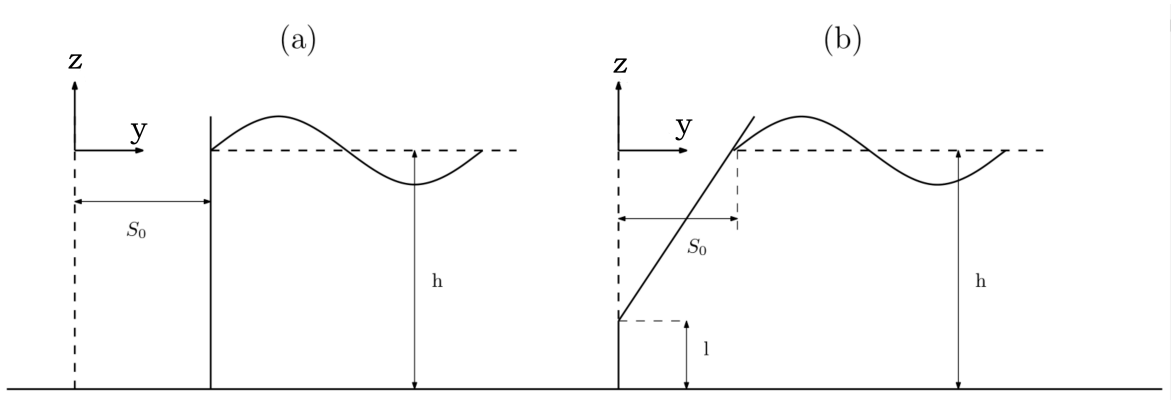
Figure 2.9: Illustration of the body oscillation that can be represented as wavemaker mechanism, where (a) and (b) are for sway and roll motions respectively (Keaney (2015))

where the wavemaker displacement along the vertical axis can be represented as:

$$S(z, t) = S_0 c(z) e^{i\omega t} \tag{2.41}$$

with S_0 is the wavemaker's stroke at z=0 and $c(z)$ being the displacement of the wavemaker over z normalized by S_0.

For piston wavemaker, $c(z)$ is given as:

$$c(z) = \begin{cases} 1, \text{for } -(h-l) < z < 0 \\ \\ 0, \text{for } z < -(h-l) \end{cases} \tag{2.42}$$

while for the flap wavemaker:

$$c(z) = \begin{cases} 1 + \frac{z}{h-l}, \text{for } -(h-l) < z < 0 \\ \\ 0, \text{for } z < -(h-l) \end{cases} \tag{2.43}$$

The vertical distance of piston wavemaker bottom and the tank floor is represented as l in Eq. 2.42. On the other hand in flap wavemaker, l is distance between the tank floor and pivot point, so that it is possible for having virtual hinge below the tank floor.

2.7.1 Boundary value problem

Solution of the Laplace equation for radiated waves depends on the value of the boundary conditions, which will be discussed here.

Kinematic boundary conditions

This boundary conditions apply on the tank floor, wavemaker surface and also free surface. The derivation discussed here are based on the work by Keaney (2015). For an arbitrary functions $G(x, z, t)$, all the boundaries can be described as,

$$G(x) = z + h(x) = 0 \text{ on the tank floor} \tag{2.44}$$

$$G(x) = z - \zeta(x, t) = 0 \text{ on the free surface} \tag{2.45}$$

$$G(x) = x - S(z, t) = 0 \text{ on the wavemaker's surface} \tag{2.46}$$

When one follows particles in Eulerian description, the problem can be mathematically stated by the material derivative. Since the fluid on the boundary moves with boundary, the material derivative of the boundary's surface with respect to time is zero.

$$\frac{DG(x, z, t)}{Dt} = \frac{\partial G}{\partial t} + \frac{\partial \phi}{\partial x}\frac{\partial G}{\partial x} + \frac{\partial \phi}{\partial z}\frac{\partial G}{\partial z} = 0 \Bigg|_{G(x,z,t)=0} \tag{2.47}$$

If vector $\overrightarrow{n}$ is defined as a unit vector on the boundary surface pointing into the fluid, hence Eq. 2.47 can be simplified:

$$-\frac{\partial G}{\partial t} = \overrightarrow{v} \cdot \nabla G = \overrightarrow{v} \cdot \overrightarrow{n} |\nabla G| \Bigg|_{G(x,z,t)=0} \tag{2.48}$$

By subtituting Eq. 2.48 into Eq. 2.44, 2.45 and 2.46, the corresponding kinematic bound-ary conditions are obtained. For flat-bottomed tank and assuming linear free-surface and wavemaker conditions, the boundary conditions are:

$$\frac{\partial \phi}{\partial z} = 0 \Big|_{z=-h} \tag{2.49}$$

$$\frac{\partial z}{\partial t} = \frac{\partial \phi}{\partial z} \Big|_{z=0} \tag{2.50}$$

$$\frac{\partial \phi}{\partial x} = \frac{\partial S}{\partial t} \Big|_{x=0} \tag{2.51}$$

Dynamic free surface boundary condition

This condition describes the water pressure on the free surface, which simply equal to the constant atmospheric pressure. The linearized dynamic boundary conditions can be stated as:

$$g\zeta + \frac{\partial \phi}{\partial t} = 0 \Big|_{z=0} \tag{2.52}$$

For the harmonically oscillating potential ϕ with frequency ω, Eq. 2.50 and 2.52 can be combined:

$$-\omega^2 \phi + g\frac{\partial \phi}{\partial z} = 0 \Big|_{z=0} \tag{2.53}$$

which gives combined free surface boundary condition.

2.7.2 Solution of wavemaker problem

The complete solution of the Laplace equation is the superposition of the unique solutions from Eq. 2.40,

$$\varphi = \sum_{n=0}^{N} X_n(x) Z_n(z) \tag{2.54}$$

Imposing the tank floor boundary condition to the depth function $Z(z)$ in Eq. 2.40b, gives:

$$Z(z) = \sqrt{\frac{4kh}{2kh + sinh(2kh)}} cosh[k(h+z)] \tag{2.55}$$

To simplify the problem, only waves radiation in a positive direction is considered, $X(x)$ in Eq. 2.40a becomes:

$$X(x) = ce^{-ikx} \tag{2.56}$$

with wavemaker kinematic surface condition Eq. 2.51 and $\varphi(x, z)$ in Eq. 2.39c, $X(x)$ can be found as:

$$X(x) = \left[\frac{1}{ikh} \int_{-(h-l)}^{0} c(z)Z(z)dz \right] e^{-ikx} \tag{2.57}$$

$X(x)$ term is found as a function of wavemaker's depth profile, which is not necessarily the case for $Z(z)$. The first term in Eq. 2.57 sometimes referred to as the Biesel coefficient.

The dispersion relation, which relates the waves' angular frequency ω to wave number k, can be found by dividing Eq. 2.56 by $Z(0) = 1$,

$$Z(z) = \frac{cosh[k(h + z)]}{cosh(kh)} \tag{2.58}$$

and applying the combined free surface boundary condition in Eq. 2.53.

$$\omega^2 Z(0) = g\frac{\partial Z(0)}{\partial z} \Rightarrow \omega^2 = gk\frac{sinh(kh)}{cosh(kh)} = gk/tanh(kh) \tag{2.59}$$

It is interest to note that if wave number $k = -im$ were to be imaginary, then $Z(z)$ would become harmonic and $X(x)$ hyperbolic function. Hence the dispersion relation could also become:

$$\omega^2 = -gm_n/tan(m_n h) \tag{2.60}$$

Only one real solution exists for Eq. 2.59, while infinite number of solutions for Eq. 2.60. Notation m_n in Eq. 2.60 indicates the nth wave number, where $m_0 = ik_0$ is for real wave number. Now, the complete solution Eq. 2.54 becomes:

$$\varphi = \sum_{n=0}^{\infty} c_n Z_n(z)e^{-m_n x} \tag{2.61}$$

It is now clear that from Eq. 2.40, that real k represents progressive waves, while for imaginary k gives standing waves on the surface and decay in amplitude exponentially with distance away from the wavemaker (evanescent waves).

2.7.3 Energy relations

According to Newman (1977), the total energy in a volume $\mathbf{\Omega}$ comprises of kinetic and potential energy.

$$E(t) = \rho \iiint_{\mathbf{\Omega}} \left(\frac{1}{2} V^2 + gz \right) d\tau \tag{2.62}$$

with $d\tau$ being a symbol for volume integration.

By solving boundary value problem by imposing Eq. 2.49 and Eq. 2.52 to the bottom and free surface respectively. In addition, the condition for oscillating body and far-field condition also has to be imposed:

$$U_n = \frac{\partial \phi}{\partial n} \text{ on the body surface} \tag{2.63}$$

$$U_n = 0 \text{ for far-field condition } S_{+\infty} + S_{-\infty} \tag{2.64}$$

Furthermore, the time derivative of Eq. 2.62 can be written as:

$$\frac{dE}{dt} = \int_{SB} (p - p_0) U_n ds - \rho \int_{S_{+\infty}+S_{-\infty}} \frac{\partial \phi}{\partial t} \frac{\partial \phi}{\partial n} ds \tag{2.65}$$

with $(p - p_0)$ is the pressure changes on the body, which can be equally stated in terms of linear roll motion by:

$$\int_{SB} (p - p_0) U_n ds = \frac{d\eta_4}{dt} (A_{44} \frac{d^2\eta_4}{dt^2} + B_{44} \frac{d\eta_4}{dt} + C_{44}\eta_4 - \rho g V) \tag{2.66}$$

The average energy in one period for period harmonic motion, and by representing the velocity potential as the outgoing waves, the damping on the oscillating body from the radiated waves follows:

$$B_{33} = \rho \left(\frac{A_4}{|\eta_4|} \right)^2 \frac{g^2}{\omega^3} \tag{2.67}$$

with A_4 being the waves amplitude generated by the oscillating body.

Chapter 3

Numerical Modeling of Forced Roll Oscillation

3.1 General

As already discussed in Chapter 2.6, the Navier-Stokes methods which accounts the fluid viscosity are preferred to solve the roll damping problem of the structure with sharp corner. In general, there are several possible methods to approximate the Navier-Stokes equations (see Section 2.5.1) for the problems that incorporate free surface. A brief overview of them are given in Kristiansen and Faltinsen (2012), which are illustrated in Fig. 3.1 below.

(a) Sketch of a numerical wavetank

(b) One-Fluid formulation, smoothed interface between air and water.

(c) Sharp interface, geometry conforming grid

(d) Fixed domain, pertutbation of potential
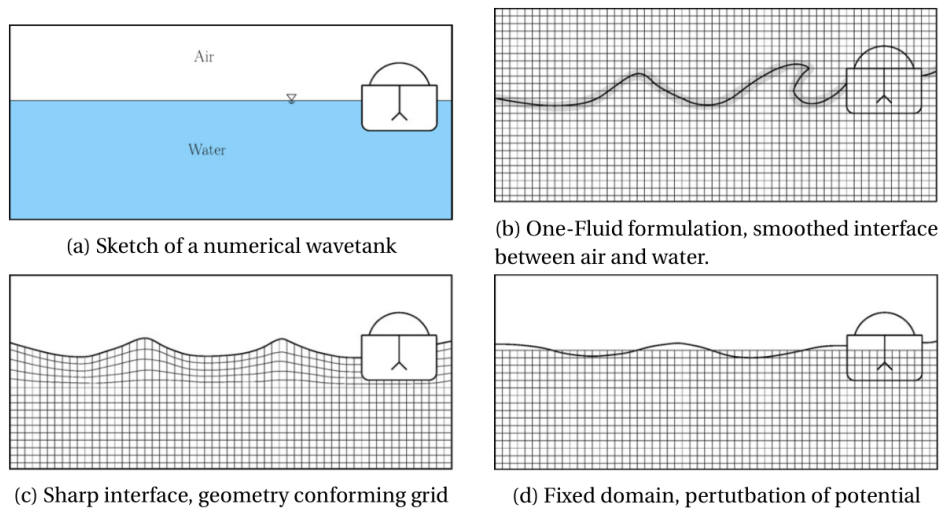
Figure 3.1: Possible numerical implementations of the wave tank problem with free surface Kristiansen and Faltinsen (2012)

The choice of the numerical methods depends on the problem that one deals with. For instance, the problem of ship that oscillates with really small motion due to excitation forces from linear waves, one may choose the scheme (d) from Fig. 3.1 since the scheme represents the correct physics. One may also use scheme (b), which is preferable for highly nonlinear waves

case, but that would be computationally intensive without significant difference of results.

Navier-Stokes method can be distinguished into two types: grid and gridless methods. Grid methods are already illustrated previously in Fig. 3.1, which may be fixed (Eulerian description) or boundary fitted (Lagrangian description). On the other hand, the gridless methods follow the individual fluid particles in time. The summary of Navier-Stokes method is given in Fig. 3.2 below. For more detailed explanation, one may refer to Faltinsen and Timokha (2009).
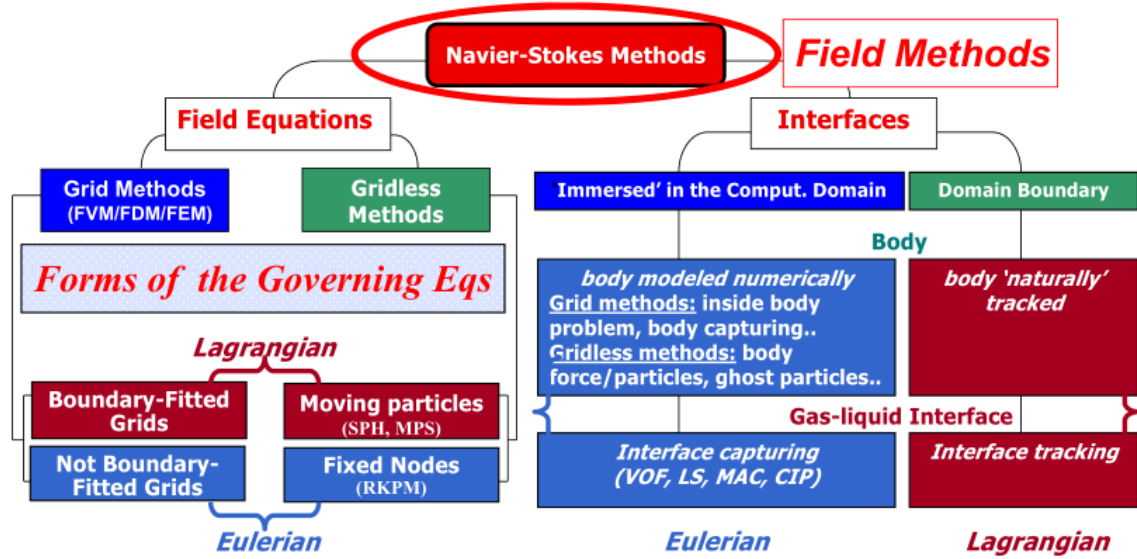
Figure 3.2: Overview of Navier-Stokes methods including the types of field equations and the feature of the interfaces Faltinsen and Timokha (2009)

The previously discussed numerical schemes are part of the CFD methods, the methods simulate the discretized fluid flow in a very small domain of space and time. The flow equations are based on the derived Navier-Stokes equations with Eulerian description (see Section 2.5.2). Finite Volume Method (FVM) based solver with dynamic meshes that based on OpenFOAM®, PVC2D-Roll, is used in present study. Thorough description regarding CFD can be found in several literature, among of them is Ferziger and Peric (2001) which discussed the basis of this chapter.

3.2   Finite Volume Method

Brief description of how FVM solves the Navier-Stokes equations will be given in this section, for more complete derivation one may refer to Jasak (1996). Recall the Eq. 2.26 for Newtonian incompressible fluid, and by neglecting the body force term the equation can also be expressed as:

$$\underbrace{\frac{\partial \mathbf{u}}{\partial t}}_{\text{temporal term}} + \underbrace{\nabla.(\mathbf{uu})}_{\text{convection term}} - \underbrace{\nabla.(\nu\nabla\mathbf{u})}_{\text{diffusion term}} = \underbrace{\frac{\nabla p}{\rho}}_{\text{source term}} \tag{3.1}$$

The discretization of above equation in FVM method is divided into : time and space discretization.

According to Patankar and Baliga (1981), since time is a parabolic coordinate, the time discretization is done by imposing the initial condition and march the solution in time by the prescribed time-step.

Space needs to be discretized into a finite number of non-overlapping convex polyhedral with flat faces throughout the computational domain (see Fig. 3.3), so-called control volume. Every variables values are stored in control volume centre, and they will be interpolated to the volume faces by the chosen interpolating schemes.
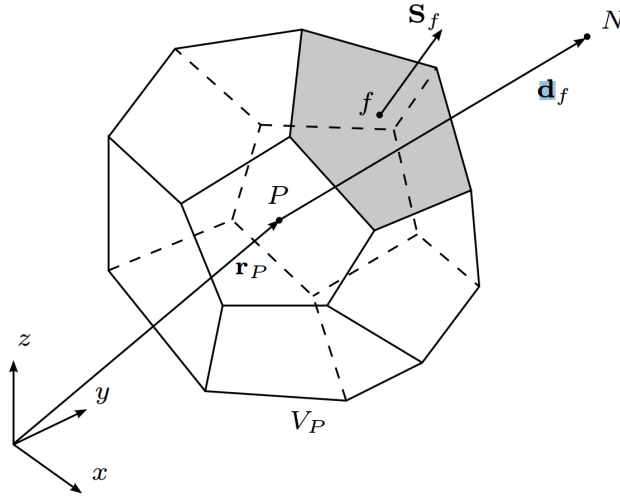
Figure 3.3: Polyhedral with arbitrary number of corners control volume cell with centre P and volume V_P . N is the neighbouring cell centre, which is $\mathbf{d}_f$ away from P. $\mathbf{S}_f$ is the cell faces normal vectors. (Jasak (1996))

FVM approach the problem by solving the discretized integral forms of Eq. 3.1 and the discretized of 2.25 over a control volume V_P around point P. The order of discretization needs to be equal or higher than the order of equations, which in this case is second order accurate in space and time.

$$\int_t^{t+\Delta t} \left[\int_{V_{CV}} \frac{\partial \mathbf{u}}{\partial t} dV + \int_{V_{CV}} \nabla.(\mathbf{uu}) dV - \int_{V_{CV}} \nabla.(\nu \nabla \mathbf{u}) \, dV \right] = \int_t^{t+\Delta t} \left(\int_{V_{CV}} \frac{\nabla p}{\rho} dV \right) \tag{3.2}$$

As mentioned before, all the terms on the above equation are need to be discretized. Assumptions of the scheme are chosen by the user, as long as the equations are second order or higher accuracy. The results are a system of algebraic equations of all the control volumes in computational domain.

3.3 PVC2D-Roll solver

PVC2D-Roll is the tailor-made numerical PVC code that has been developed based on hybrid approach (see Kristiansen and Faltinsen (2012)) specifically for roll motion, which combine both of potential and Navier-Stokes methods. Computing roll motion by means of CFD requires great computational effort due to the needs of mesh deformation technique to model nonlinear body-boundary condition, and also high resolution mesh to capture the waves that propagate out of from the rolling body. PVC2D-Roll simplifies the problem by adopting potential methods to model propagating waves, and Navier-Stokes methods to capture flow-separation from the ship bilge keels / bilge boxes. This code has been under a series of validation studies, for instance, Ommani et al. (2015, 2016b,a), which has proven to be quite promising to resolve the ship roll motion.

For present study, the submerged computational domain is fully modeled as Navier-Stokes domain which based on the one that derived in section 2.5.1 and 3.2. The free surface conditions are linearized (see fig. 3.1 (d)), means that it is one-phase computational domain and bounded in the interface between water-air (z=0). The wave elevation is simulated through the boundary condition as discussed in 2.7. No turbulence model is applied.

3.4 Solid Body Rotation mesh deformation technique

CFD methods need to do the iterative calculations based on the initial and boundary conditions. Boundary conditions itself could be approximated as fixed or deforming. As discussed previously, mesh deformation technique is needed to resolve roll damping problem. Brief explanation regarding the Solid Body Rotation mesh deformation technique that based on OpenFOAM®will be given in this chapter, for more thorough understanding please refer to Bos (2009).
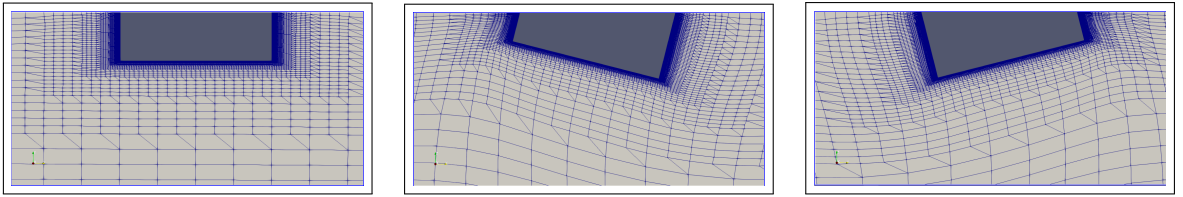
Figure 3.4: Solid Body Rotation technique in the roll motion case. The meshes are deformed by the changes of body boundaries

When the boundaries are deforming, it is important to preserve the internal mesh point according to the domain shape, no negative cell volumes, and quality (orthogonality and skewness)

Present mesh deformation technique is based on modified pseudo-solid equation available at OpenFOAM®. The mesh deformation equation itself is based on the linear elasticity

equation, which modified to allow rotations. The so-called solid body rotation stress (SBR stress) can be expressed as following:

$$\nabla \cdot (\gamma \nabla \mathbf{x}) + \nabla(\gamma(\nabla \mathbf{x} - \nabla \mathbf{x^T})) - \lambda \mathbf{tr}(\nabla \mathbf{x}) = \mathbf{0} \tag{3.3}$$

with $\mathbf{x}$ being the position of mesh internal point, tr is the trace, and λ can be connected to the property of elastic material (Young's modulus). γ itself, diffusivity, can be regarded as stiffness which depends on the distance (r) from the moving boundary. Based on Bos (2009) works, m=2 was used to maintain robustness and proved to have smooth and efficient mesh motion.

$$\gamma(r) = \frac{1}{r^m} \tag{3.4}$$

Solving the SBR equation Eq. 3.3 leads to sparse system of equations that can be solved by using standard iterative technique.

3.5 Case numerical modeling

3.5.1 General

The forced roll simulation of ship mid section with bilge boxes are considered in this present study. The inertial Earth-fixed reference frame Oxyz and body-fixed reference frame Rx'y'z' is used, where R is the centre of rotation. The conventional seakeeping coordinate system is adapted, where starboard is on the left part of the Fig. 3.5. Centre of rotation is represented as point R and does not coincide with mean water line.
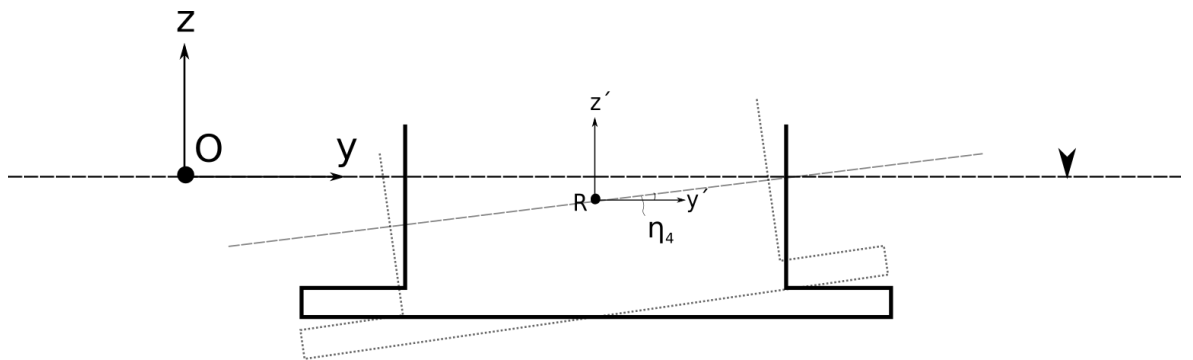
Figure 3.5: Coordinate system adapted in the numerical model

The body is forced to harmonically oscillate in roll with the given amplitude and frequency. The linear ramp is adopted at the beginning for 5 forcing period to minimize the transient solution. The corresponding oscillatory motion including its linear ramp can be mathematically

described by Eq. 3.5

$$\eta_4 = \alpha\eta_{4a}sin\left(\frac{2\pi}{T}t\right), \quad \alpha = \frac{t}{5T} \quad \text{for t} \leq 5\text{T, and } \alpha = 1 \text{ for t} > 5\text{T} \tag{3.5}$$

The motion is considered linear, where the response are proportional to the excitation. The nonlinear damping term takes the linearized equivalent form (see Section 2.6). The roll moment that acting on the body can be decomposed into added-mass (A_{44}), damping (B_{44}) and linear restoring (C_{44}) terms. The steady-state part can be expressed as:

$$A_{44}\ddot{\eta}_4 + B_{44}\dot{\eta}_4 + C_{44}\eta_4 = -M_4 \tag{3.6}$$

where η_4, $\dot{\eta}_4$ and $\ddot{\eta}_4$ are the rotation, angular velocity and acceleration of the body respectively. The M_4 term, forces acting on the body, is obtained from the disturbed fluid pressure integration that obtained from the Eq 3.2.

By utilizing the orthogonality of the harmonic function, one may extract the hydrodynamic coefficients (a_{44} and b_{44}) from Eq. 3.6 above.

$$\int_0^{2\pi} sin(mx)cos(mx)dx = 0 \tag{3.7}$$

$$\int_0^{2\pi} sin(mx)sin(nx)dx = \begin{cases} 0, if n \neq m \\ \\ \pi, otherwise \end{cases} \tag{3.8}$$

If one only consider the dynamic pressures working on the body, this means the hydrostatic term is vanished. Based on the above orthogonality relationship, the hydrodynamic coefficients can be found with the following equations:

$$A_{44} = \frac{\int_0^{nT} -M_4(t)\ddot{\eta}_4(t)dt}{\int_0^{nT} \ddot{\eta}_4(t)\ddot{\eta}_4(t)dt} \tag{3.9}$$

$$B_{44} = \frac{\int_0^{nT} -M_4(t)\dot{\eta}_4(t)dt}{\int_0^{nT} \dot{\eta}_4(t)\dot{\eta}_4(t)dt} \tag{3.10}$$

3.5.2 Geometry and computational mesh

Three configurations of two-dimensional ship mid sections are considered, each configuration has different disk diameter (D_D) with similar thickness (t_D).

Main particulars of every configurations are given in Table 3.1 below.
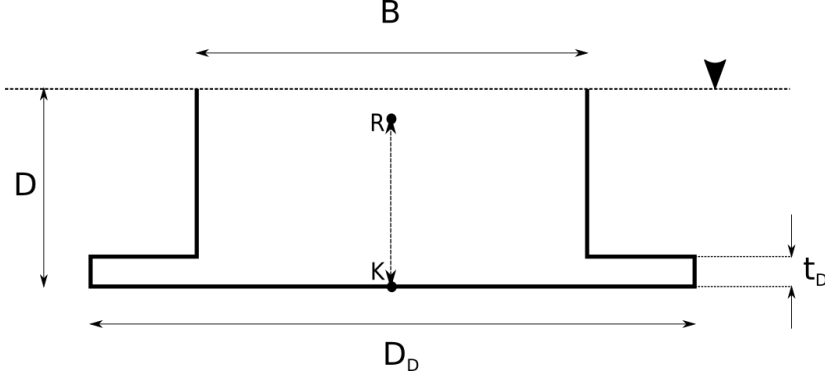
Figure 3.6: Visualization of the two-dimensional ship mid section with the corresponding parameters

Table 3.1: Non-dimensionalized ship mid section particulars

Parameters (Non-dimensionalized)	BB1	BB2	BB3
Breadth (B/B)		1.00	
Draught (D/B)		0.32	
Keel-to-centre of rotation (KR/B)		0.2912	
Disk thickness (t_D/B)		0.056	
Disk diameter (D_D/B)	1.20	1.30	1.40
Section area (A/(BD))	1.035	1.0525	1.07

As discussed in Section 3.2, the space needs to be discretized. Body-fitted unstructured mesh type is adopted for the present study. The meshes are generated by Hexpress from Fine Marine®package by Babak Ommani, senior researcher in SINTEF Ocean. Example of the generated mesh is illustrated in Fig. 3.7 below. The flow separation from the sharp corner is believed more important compare to the viscous stresses that come from boundary layer, therefore the meshes are more refined near the bilge boxes. The computational domain is chosen sufficiently long enough to avoid the wave reflection. Having large cells away from the body may give some numerical damping with respect to radiated waves.

SBR mesh deformation technique (see Section 3.4) is adopted to incorporate instantaneous body boundary condition into numerical calculation. This was shown by Fredriksen (2015), Ommani et al. (2015) and Ommani et al. (2016b) on their studies, the exact body boundary condition is needed to model the relative motion in the separation point. The relative motions between fluid and the body motion dictate the strength of the vortex shedding.

Since the Navier-Stokes equations are almost not possible to solve analytically, one of the methods is to discretize the equations spatially with the so-called control volume/grid/mesh. When the equations are approximated by the discrete equations, the *discretization error* will always exist. Theoritically, numerical method approximation approaches exact solution when the grid spacing goes to zero. Meaning that the solution will converge to a grid-independent solution. A series of mesh convergence study was performed with 4 steps block refinement
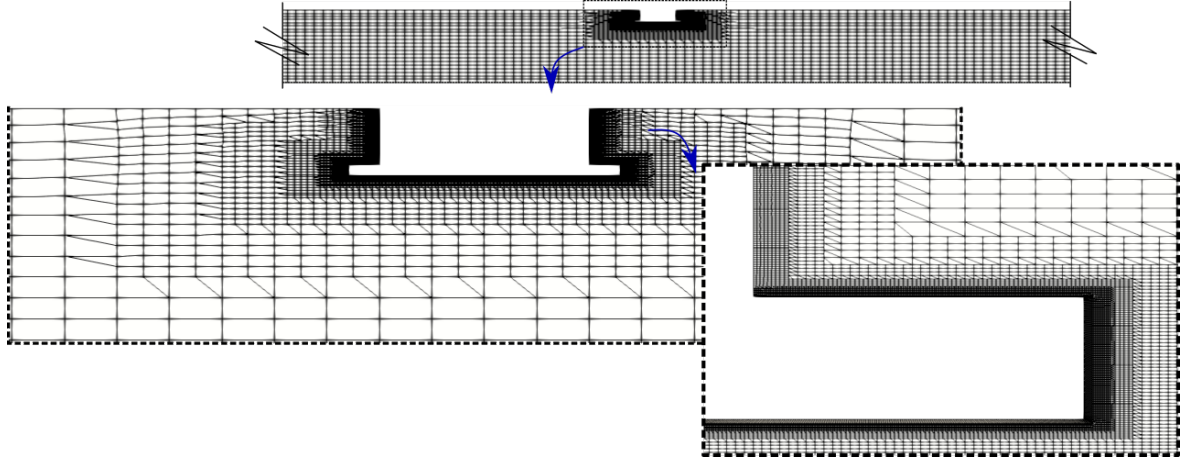
Figure 3.7: Unstructured boundary-fitted mesh generated by Hexpress from Fine Marine®

method. The mesh refinement was done by selecting the refinement block, and with increasing the refinement step, the cells inside refinement block will be divided into a set of smaller cells. Number of the generated cells for the mesh convergence study is summarized in Table 3.2.

Table 3.2: Number of cells generated for different configurations and refinement steps

Refinement level	No. of cells			Points			Faces		
	BB1	BB2	BB3	BB1	BB2	BB3	BB1	BB2	BB3
R4	12666	12984	13350	26850	27538	28318	51422	52720	54208
R5	16 322	17126	17786	34676	36388	37808	66303	69571	72261
R6	23424	25146	26586	49882	53530	56614	95212	102202	108064
R7	37 344	40284	43566	79694	85982	92954	151878	163842	177174

From Fig. 3.8, one may observe that the solutions (in this case, A_{44} and B_{44}) converge towards mesh independent solution. The differences between the solutions come from refinement level R6 to R7 are less than 1 %. Practically speaking, if the refined results are less than 5 % difference from the coarser one, one may safely choose the coarser mesh. Hence, the mesh refinement R6 scheme is chosen for all the configurations throughout the present study.

3.5.3   Time step refinement study

As briefly mentioned in 3.2, the time needs to be discretized by the defined time-step. According to Ommani et al. (2016b), there are three conditions that restrict the time-step.

1. Since explicit Euler method is used in this present study, which are always conditionally stable, the restriction should be imposed to restrict the error grows indefinitely. The so-called Courant–Friedrichs–Lewy(CFL) criterion has been used as a cure for this problem,
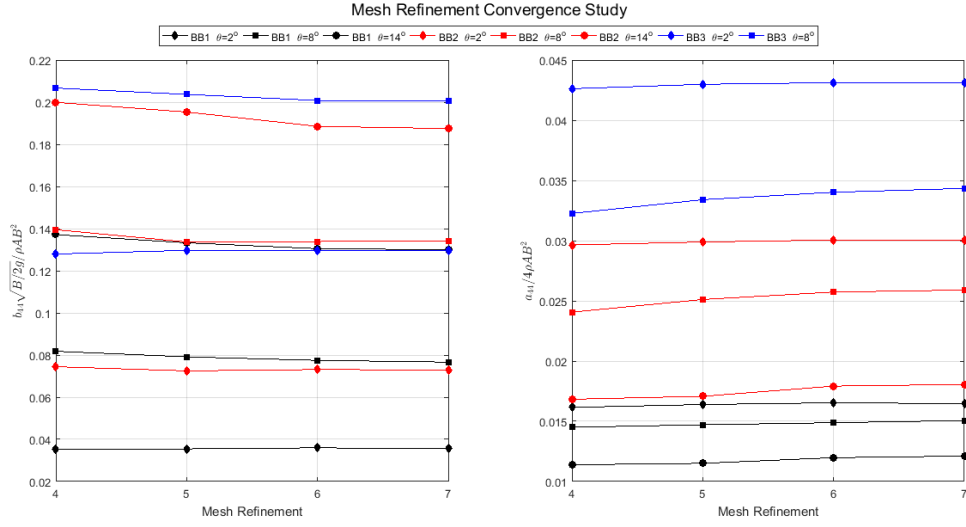
Figure 3.8: Mesh convergence study with different configurations and forcing amplitudes

by limiting the ratio of time-step Δt to the characteristic of convection time $u/\Delta x$ to unity. This is reasonable restriction for information propagation-wise, since the fluid particle cannot move more than one grid length in a single time step.

$$\frac{U\Delta t}{\Delta x_i} < 1 \tag{3.11}$$

where U being the local velocity, and Δx_i is the minimum mesh spacing in computational domain

2. Due to the deforming body boundary condition as well as stability, the time step needs to be fixed and decreased with respect to the roll amplitudes. This is due to the sensitivity of hydrodynamic coefficients extraction to phasing, as shown by Kristiansen et al. (2014)

3. Accuracy of the instantaneous body boundary condition and its velocity is important in terms of the strength of the produced vortex-shedding.

A series of time-step convergence tests were conducted in order to determine the required time-step for each forcing amplitude, this is due to the conditions discussed above. It was chosen 1000 time steps per period for the case with forcing amplitudes below 5°, 2000 for amplitudes between 5° and 10° and 4000 for amplitudes above 10°. The time-step settings are also recommended by Ommani et al. (2015).

3.5.4 Boundary conditions and initial values

The information about the at the domain boundaries are needed in order to obtain the unique solution. Generally, the conditions are either given value (Dirichlet boundary conditions), its gradient in particular direction (Neumann boundary conditions) or a linear combination of those two quantities. While initial values problem are needed for march the solutions of partial differential equations in time. The illustration of the computational domain including
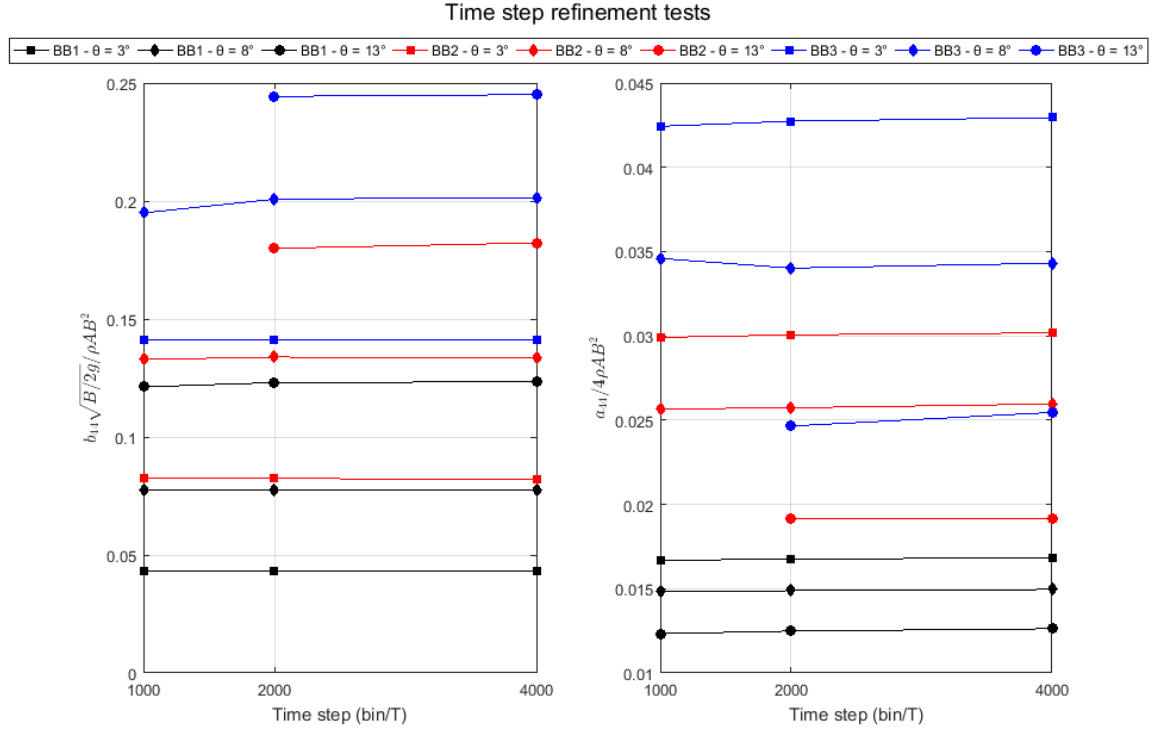
Figure 3.9: Time-step convergence study with different configurations and forcing amplitudes

the boundaries is given in Fig. 3.10 below, while the initial and boundary values that used for present study are summarized in Table 3.3.
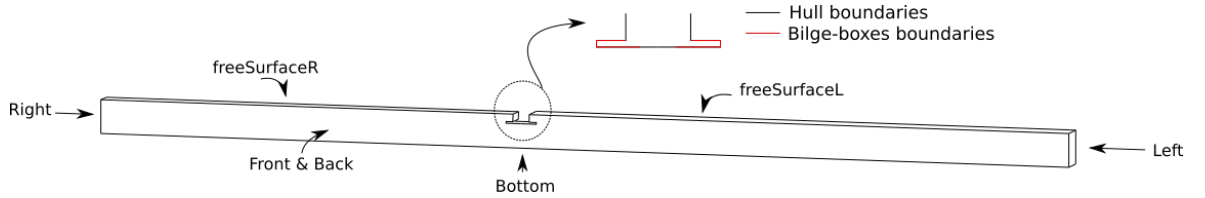
Figure 3.10: Name and the location of the boundary condition used for the numerical simulation

The static pressure has to be calculated in the location of interest. The body should behave as a moving wall, thus the horizontal and vertical fluid velocity is always zero on the instantaneous body surface. In addition, the pressure is calculated according the flux (velocity) in the wall. As one may observe from Fig. 3.10, the bilge boxes patch were made to be equal with the one in experiment (see Chapter 4). Left, right and bottom boundary conditions are modeled as a no-slip wall. The waveSurfacePressure boundary condition computes the wave height and the pressure change due the free surface profile change by integrating the fluid velocity at the free surface over time. The outflow velocity is defined as zeroGradient while the inflow velocity is obtained from the flux with the specified inlet direction. A slip condition is applied tangential to the freeSurfaceR freeSurfaceL patch.

Table 3.3: Boundary types and initial values specified in present study

Boundary name	Boundary conditions (OpenFOAM®)		
	Total pressure, p	Dynamic pressure, p_gh	Velocity, U
Front	*empty*	*empty*	*empty*
Back	*empty*	*empty*	*empty*
Hull	*calculated, uniform 0*	*fixedFluxPressure, uniform 0*	*movingWallVelocity, uniform(0,0,0)*
Bilge boxes	*calculated, uniform 0*	*fixedFluxPressure, uniform 0*	*movingWallVelocity, uniform(0,0,0)*
Left	*calculated, uniform 0*	*zeroGradient*	*fixedValue, uniform(0,0,0)*
Right	*calculated, uniform 0*	*zeroGradient*	*fixedValue, uniform(0,0,0)*
Bottom	*calculated, uniform 0*	*zeroGradient*	*fixedValue, uniform(0,0,0)*
freeSurfaceL	*calculated, uniform 0*	*waveSurfacePressure, uniform 0*	*pressureInletOutletParSlipVelocity, uniform(0,0,0)*
freeSurfaceR	*calculated, uniform 0*	*waveSurfacePressure, uniform 0*	*pressureInletOutletParSlipVelocity, uniform(0,0,0)*

3.5.5 Numerical schemes

As mentioned in Section 3.2, all the terms in Eq. 3.2 need to be discretized with the chosen numerical schemes. The numerical schemes used in the present study is adapted from Ommani et al. (2016b).

Temporal derivative terms are discretized by first order explicit Euler method, while second order backward scheme is preferred to march the free-surface elevation solution forward.

The second order scheme is adopted to discretize the spatial gradient and Laplacian terms, interpolation from cell centres to faces. While the first order Gauss Upwind method is considered to discretize the convective terms. The second order corrected scheme was chosen for this the surface normal gradient terms.

Summary of the chosen numerical schemes are given in Table 3.4.

Table 3.4: Applied numerical schemes

Terms	Terms expression	Chosen schemes
Temporal derivative	$\frac{\partial \mathbf{u}}{\partial t}$	for $\mathbf{u}$, Euler
		for ζ, Backward
Gradient	$\nabla \mathbf{u}$	Gauss linear
Divergence	$\nabla \cdot \mathbf{u}$	Diffusion term, Gauss linear
		Convective term, Gauss upwind
Laplacian	$\nabla^2 \phi$	Gauss linear
Surface normal gradient	$\mathbf{n}_f \cdot (\nabla \mathbf{u})_f$	Corrected
Face interpolation	-	Linear

3.5.6 Wave reflection estimation

The computational domain length was modeled 50 meter long without additional wave parabolic beach, hence the wave reflection are expected to disturb the pressure near the body when

present.

In order to avoid the effects of wave reflection, the time window has to be carefully selected. The body is exactly in the middle of the domain length, hence the travel distance for waves to go back and forth is 45 meters. Waves travel speed are estimated with the group velocity C_g that can be derived from Eq. 2.59.

$$C_g = \frac{d\omega}{dk} \tag{3.12}$$

Fig. 3.11 shows how the time window selection based on.
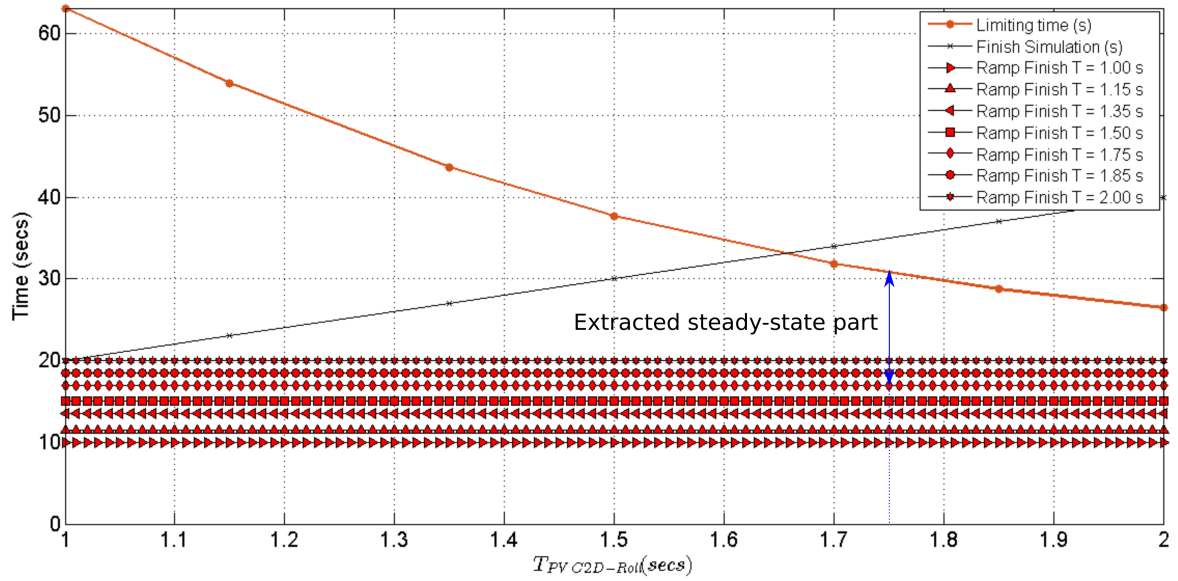
Figure 3.11: Estimation of the time window selection based on the group velocity and travel distance to go back and forth to the model. Case example shown here is for T=1.70 secs

The blue-line in Fig. 3.11 above is the part where the time series already passed the ramp and also before the wave-reflection present. The orange-dotted line is the time limit, when the reflected waves up near the model. The black line is the time when the simulation has finished. Some example of the cases where the wave reflection present is demonstrated by Fig. 3.12

The red part in Fig. 3.12 is the one that will be further processed to extract the hydrodynamic coefficients. Finally, the time window for all the simulated cases can be estimated.

3.5.7   Numerical code comparison with potential-flow solution

As initial tests, the present PVC2D-Roll numerical code results are also compared to known reference case. Box-shaped cylinder with breadth to draft ratio B/D=2.00 is forced to oscillate harmonically and solved by both of potential flow calculation (Skejetic,R. 2012, private communication) and PVC2D-Roll.
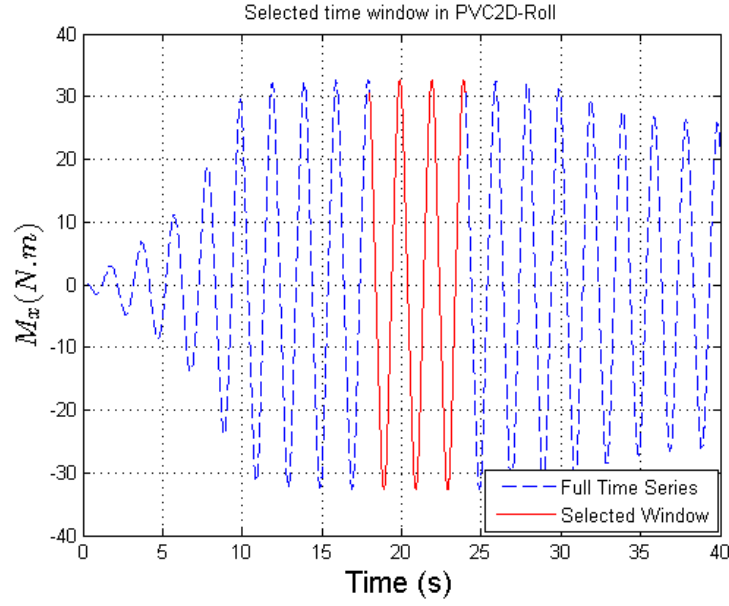
Figure 3.12: Illustration where the selected window does not get any influence from the wave reflection

Based on both of the curves in Fig. 3.13, PVC2D-Roll results are compared well with the potential flow calculation. It is interest to note that when the motion is small, the flow separation contribution is minimum and PVC2D-Roll results should approach potential flow calculation. Since PVC2D-Roll represents correct hydrodynamic behavior in the present reference case, it is expected that all numerical settings are correct and also can be applied for present study.
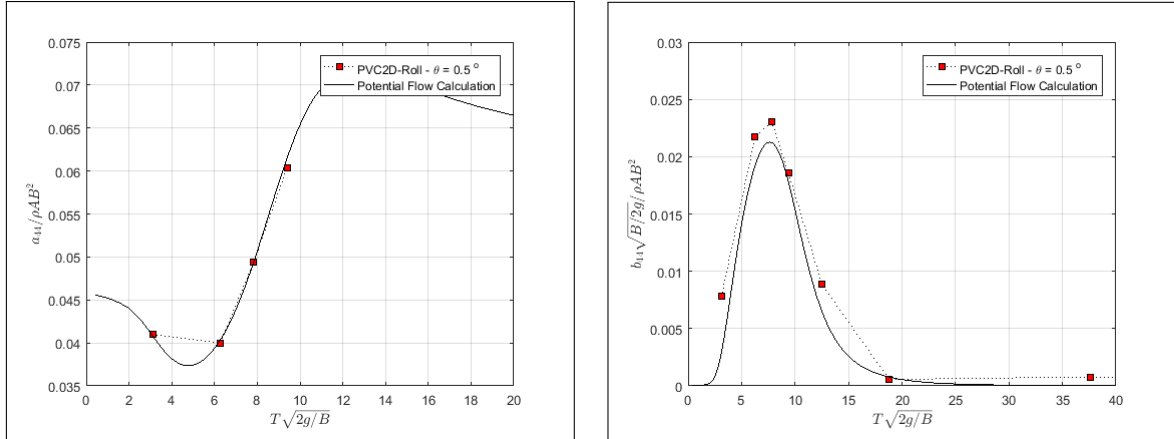
Figure 3.13: Added-mass and damping coefficients of box-shaped cylinder comparison with the potential flow solution

Chapter 4

Experimental Modeling of Forced Roll Oscillation

4.1 General

Two sets of experimental model tests were performed during February and April 2017, with the additional one set of repetition test in May 2017. Forced-oscillation of two dimensional ship mid section with bilge boxes as modeled numerically in Chapter 3 is considered. The dimension of the model without bilge boxes was also desired to have zero wave radiation damping, as shown by Vugts (1968) in Fig. 2.8.
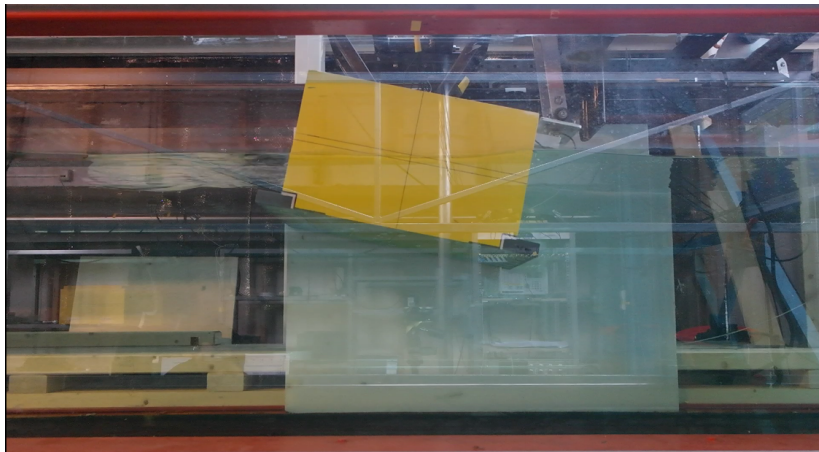
Figure 4.1: Some example of forced roll oscillation test of two-dimensional ship mid section with BB1

The aim is to extract the hydrodynamic coefficients from the radiation problem as discussed in Section 2.1, and compare with the one that obtained numerically from Chapter 3. Linearized hydrodynamic coefficients are desired (see Section 2.6), especially the nonlinearities of the coefficient with respect to roll amplitudes, hence 13 forcing amplitudes (ranging from 2 to 14 degrees) and 7 periods (1.00 s, 1.15 s, 1.35 s, 1.50 s, 1.70 s, 1.85 s and 2.00 s) were chosen.

The differences between both of the sets were the imposed harmonic motion. In February 2017 tests, the author were careless and hence the imposed forced motions were far from pure sinusoidal motion. Attempts has been made to improve the motion, and another set of tests were conducted in April 2017. More detailed discussion will be presented in latter section within this chapter.

The experiments took place in the narrow wave flume tank, Ladertanken, one of the laboratory facilities in Marine Technology Centre, Norwegian University of Science and Technology. The tank is 13.0 m long and 0.6 m wide, with the designated water depth of 1.0 m. Since the tank length is limited, the parabolic beaches are attached at both of the tank ends to break the wave energy and avoid wave reflection. The model is always placed in the middle of the tank and attached to the fixed carriage.

In order to extract hydrodynamic coefficients from the harmonic motion, the motion, wave elevation and force measurements were done by applying vertical accelerometers, wave gauges and strain gauges in specific places around the model respectively.

The schematic view of the April 2017 laboratory set up of forced roll oscillation test is given in Fig. 4.2 below. Some changes of wave gauges position has been done from January 2017 tests, due to the vibration of the wave gauges that were placed very close to the model.
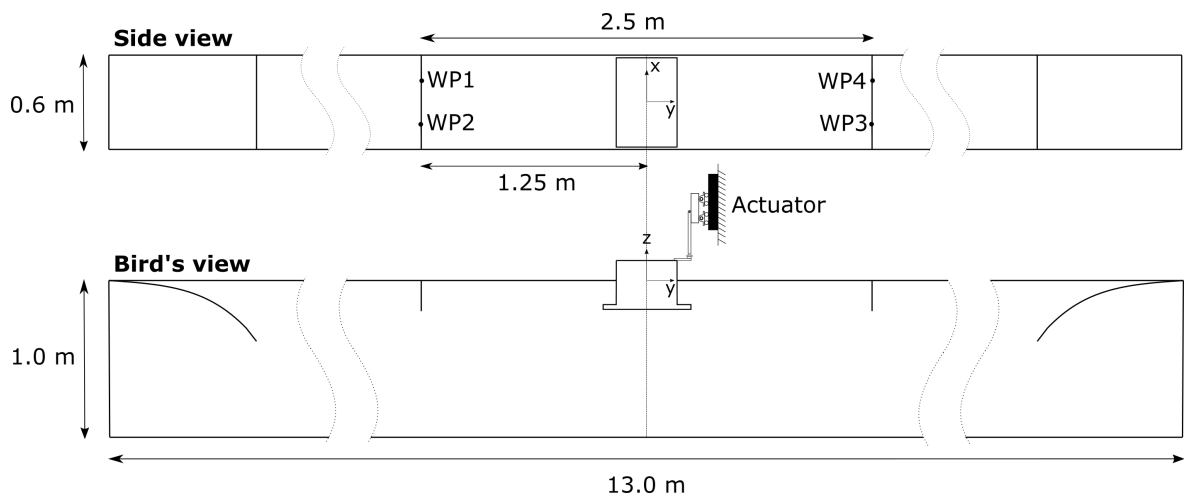
Figure 4.2: Schematic view of the laboratory set up for forced roll oscillation test in April 2017

4.2 The models and instrumentation

The model was constructed by wood plates and divinycell which accurately shaped by manual milling machine based on the 3-D CAD drawings by Trond Innset from NTNU. In addition to the appendages that used in CFD, the model with smooth rounded corner (RC) bilges also tested. The rounded-corner and bilge boxes appendages are made of PVC, some modifications were done in bilge boxes part where more than half of the volumes were replaced by the lighter

material called divinycell. The total weight of the dry model without bilge boxes is 17.874 kg, hence 27.827 kg of ballast weights are needed to ensure the desired draught is obtained. Finally, when the model and appendages are submerged into the water, the neutral buoyant state is achieved.

Figure 4.3: Ballast weights arrangement inside the model to have neutral buoyant state when the model is submerged

The roll moment of inertia I_{44} and restoring coefficient C_{44} are also investigated by the pendulum and inclination tests respectively. The principle of the tests can be found in several text books about stability and solid mechanics. In addition to the geometry parameters which are similar with the one in Table 3.1, another important parameters are summarized in Table 4.1 below.

Table 4.1: Roll moment of inertia and restoring coefficients

Parameters	RC	BB1	BB2	BB3
$I44^{(2D)}(kgm^2/m)$	1.56	1.79	1.93	2.13
$C44^{(2D)}((kgm^2/s^2)/m)$	100.55	99.48	99.52	97.83

Two accelerometers and eight strain gauges are attached around the model. Accelerometers were used to measure the average of vertical accelerations in two fixed position on the model. The force measurement were acquired from four strain gauges measuring force in x-direction and the other four for y- direction force. Thus, two sensors were utilized to measure the force in each direction on each side. Then with averaging the magnitude between the two sensors may increase the accuracy and the quality of the experiment. Fig. 4.4 below describes the placement of the accelerometers and strain gauges within the model.

Another one strain gauge is attached in the attachment point between model and activator arm (see Fig. 4.2). This strain gauge acquires the total force that the actuator gave to the model in order to rotate with a specific rotational angle.

As a summary, the list of sensors that used in the present study including the abbreviations are given in Table 4.2 below.
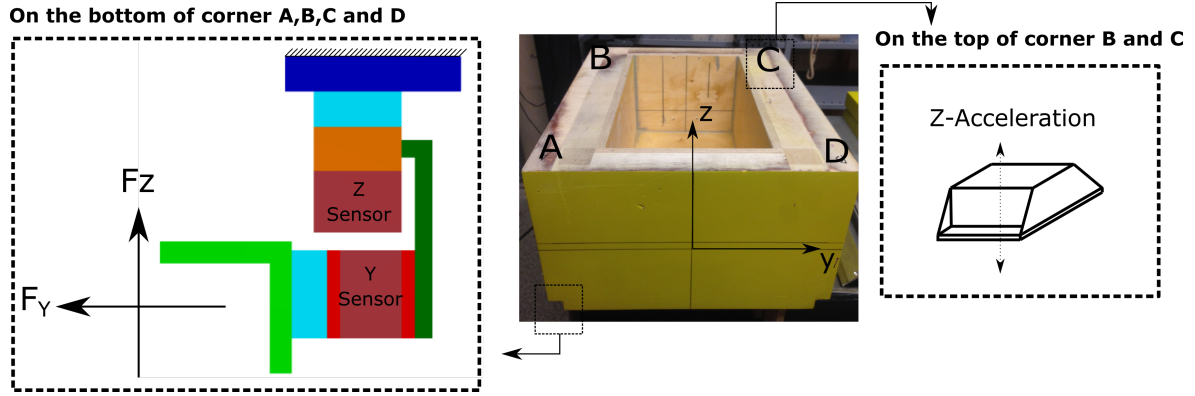
Figure 4.4: Information of the accelerometers and strain gauges attachment. Coordinate system used is the same as given in section 3.5.1

Table 4.2: List of the sensors that used in the present study

Sensor type	Sensor name
Accelerometer	Acc_B and Acc_C
Strain gauges	Fz_exc, Fy_A, Fz_A, Fy_B, Fz_B, Fy_C, Fz_C, Fy_D and Fz_D
Wave gauges	WP1. WP2, WP3 and WP4

Finally, all the motion and force terms in Eq. 2.35 can be obtained from the present experiment setup. In addition, the radiated waves are also obtained from the wave gauges.

4.3 Motion actuator

The roll motion is obtained from the translation-rotation mechanism from one DOF actuator to the model centre of rotation. Rotary bearings are placed on both sides of model width, which attached to the fixed carriage to keep the model in place. In present study, centre of rotation is fixed at the same place as in the numerical model (see Fig. 3.6). In principle, one can derive the mathematical equation to transfer the desired rotation angle from point A to the imposed translation of point C, or vice versa. The schematic view of the actuator mechanism is illustrated in Fig. 4.5 below.

L_{arm} is the distance between actuator arm-body arm attachment point to the zero position of the actuator, Y_{arm} is the distance between body centre of rotation to the actuator arm-body arm attachment point , θ is the angle between horizontal line parallel to the y-axis and $\overline{AB}$ and h is the distance between the centre of rotation to the zero position of actuator.

In order to obtain pure harmonic sinusoidal of amplitude η_4 motion, the translation of point C can be mathematically described as:

$$z'(t) = \overline{AB}\,sin(\theta + \eta_4(t)) + \sqrt{L_{arm}^2 - (y_{arm} - \overline{AB}cos(\theta))^2} - h \qquad (4.1)$$
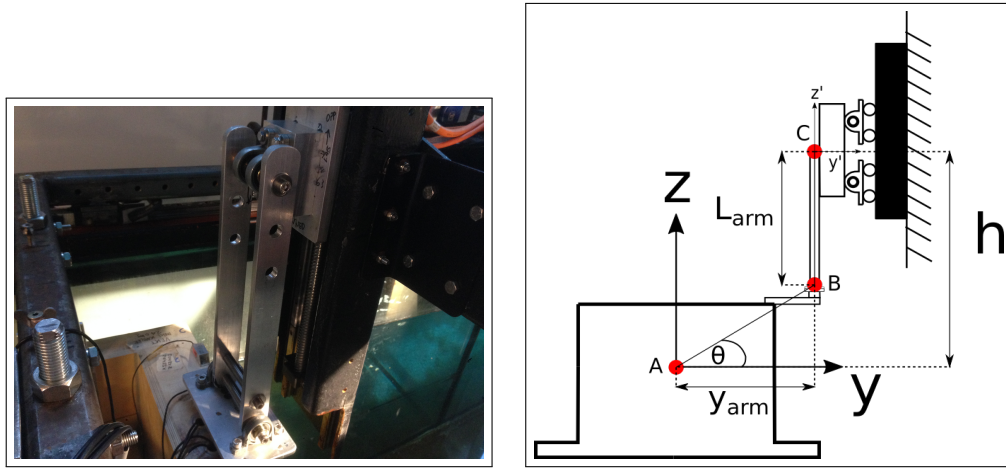
Figure 4.5: Left: physical actuator used for the forced roll oscillation. Right: Schematic view of the body rotation - actuator translation mechanism
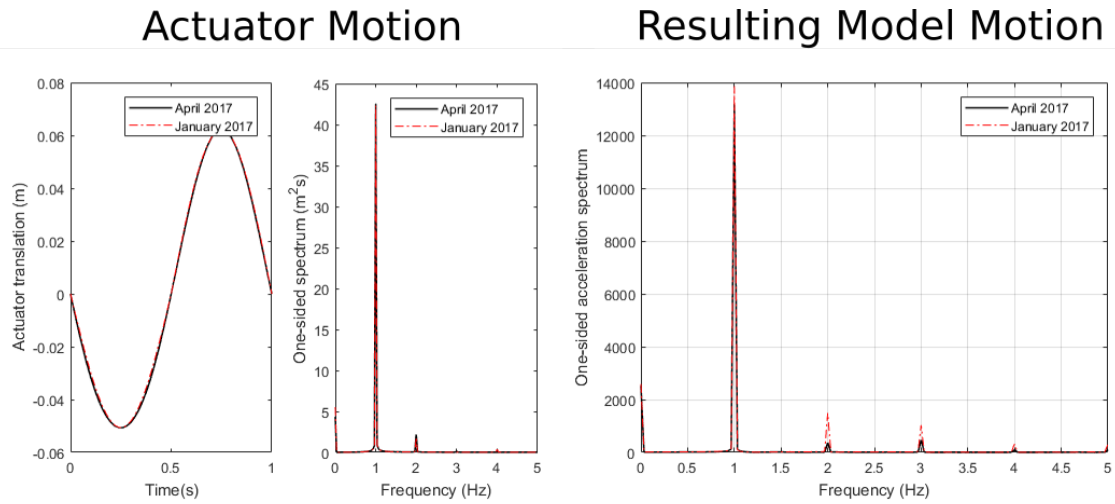
Figure 4.6: One of the comparisons of imposed actuator motion and resulting model motion between January 2017 tests and April 2017 tests

As mentioned before, the January 2017 tests were incorrect due to the author was not aware of Eq. 4.1 above. Hence, the imposed motion of actuator (z') was not calculated with that equation, but with the modified pure sinusoidal motion with some specific maxima and minima to obtain only the correct roll angle. The comparison between the actuator motion and the resulting η_4 from both of January and April 2017 tests is given in Fig. 4.6. The results from January 2017 gives higher additional harmonic, which should be avoided if one desire pure sinusoidal motion. Even though improvement was quite significant for the April 2017 tests, but the additional harmonic still appeared. This will be discussed in latter section of this chapter.

4.4   Analysis procedures

In order to extract hydrodynamic coefficient as already discussed in Chapter 3, several procedures have to be done first and will be discussed within this section.

The sensors mentioned in Section 4.2 before acquire the data in the form of discrete signal, meaning the data are sampled at equal intervals of time. The sampling frequency has to be sufficiently high enough to capture all variations of the recorded data. On the other hand using high sampling frequency increases the data size which would be an issue for the storage and data processing. The consequence of using lower sampling frequency than what it supposes to capture is illustrated by Fig. 4.7. The sampling frequency of the present study was chosen to be 600 Hz based on suggestion from Babak Ommani, which was believed to capture most of the important phenomena in this present experiment.
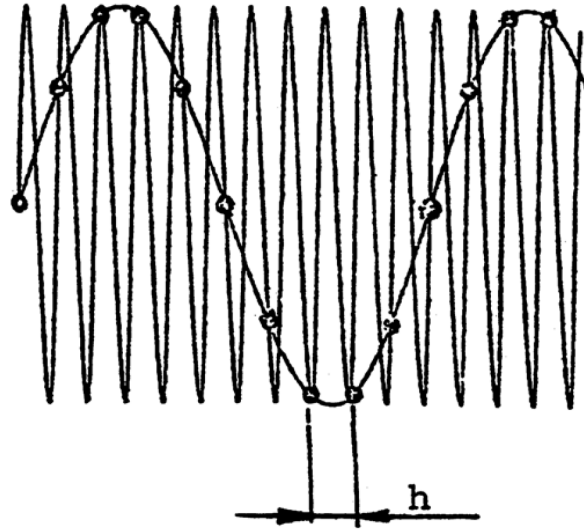
Figure 4.7: Illustration where the sampling frequency is not sufficiently high enough to capture the real observation data variation. In order to capture the correct sinusoidal, the sampling rate h suppose to be twice higher

4.4.1   Calibration of instruments and zero-ing

Before calibrate the sensor, the zero reference value has to be determined first. Most of the sensors are sensitive and could be drifted by some temperature changes or some other particular condition. The procedure of zero-ing is by doing measurement for some duration of time and finding the average of the measured, which will be assigned as the new zero values.

After the new zero values obtained, then the sensors need to be calibrated in order to acquire the correct measurement. Calibration means finding the exact relationship between the output signals and the known physical properties e.g. force, displacement, water elevation, and the other. One key aspect is to ensure the linearity of the sensors, which is the most important rather than dealing with the nonlinearities that makes data acquisition become

more complicated. The procedures of calibration are the same in concept for all the sensors, which can briefly be summarized as below:

1. Several different known/given values of specific parameter were measured, such as force, displacement, etc. The results output would be in voltage

2. Trend analysis of the measured values, which is expected to get linear relationship between the given and measured values

3. Calibration factor [Unit/Volt] was then obtained, then input the number into the data acquisition system for the specific calibrated sensor.

$$y = mx + b \tag{4.2}$$

where m is the calibration factor, and b is being the zero value.

4.4.2   Motion calibrations

The motion calibrations were done manually by using inclinometer everytime the parameters inside the motion's mathematical model Eq. 4.1 need to be changed. The resulting rotation angles from the imposed mathematical model for low, medium and high roll amplitudes were verified, the periods were chosen to be sufficiently high enough due to the update rate limitation of inclinometer. When the desired angles achieved for all the tested cases, it was assumed that the actuator have a capability to perform correctly in the other cases. In reality, this does not hold true, and discrepancies were obtained especially for low forcing period (sufficiently fast motion). This will be discussed in latter chapter.

4.4.3   Forced roll time series

The actuator needs time-series input that derived from Eq. 4.5. The time series input files are automatically generated with the MATLAB script that developed by Prof. Trygve Kristiansen, which allows to generate a series of several forced oscillation with different amplitudes and periods. Due to the memory limitation of the actuator system, the time series are restricted to maximum three hours. Linear ramp-up and ramp-down were applied to the time series for five forcing periods before and after the actuator achieves the steady-state oscillation. Resting time of 120 seconds were applied in between of two time series to make sure the water is calm before the new one started, this was empirically chosen by visual observation.

4.4.4   Filtering

Besides acquiring the data within the frequency of interest, most of the data acquisition sensor that were used during present study also captured noise with high frequency. Furthermore, the drifting that caused by change of water/ room temperature also may appear as the low frequency component of the oscillatory system. Therefore, a digital Band-pass filter that were developed in MARINTEK by Prof. Trygve Kristiansen used to remove the unimportant

frequency in the time series. This is preferrable compare to the real-time filtering, which may cause phase delay. Illustration of the time-series filtering is best described by Fig. 4.9 below.
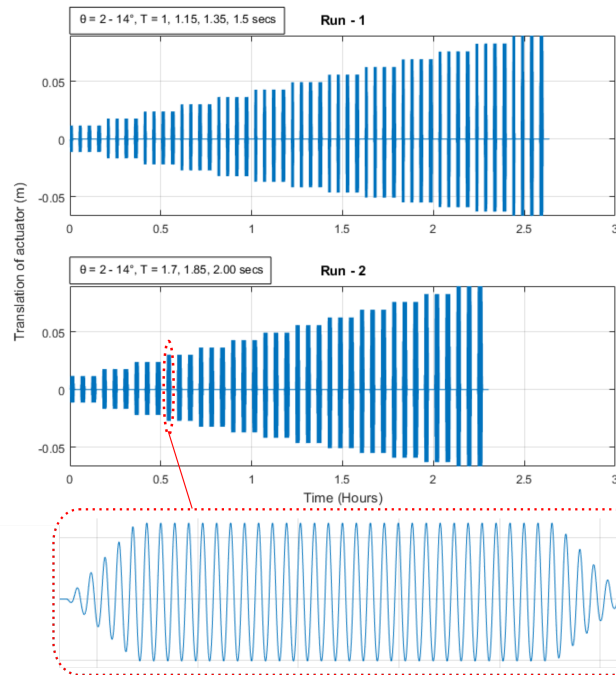
Figure 4.8: Constructed time series for the actuator input. The series need to be divided into two parts due to the actuator system memory limitation. The blue columns shown in the figure represent time series for different forcing amplitudes and periods.
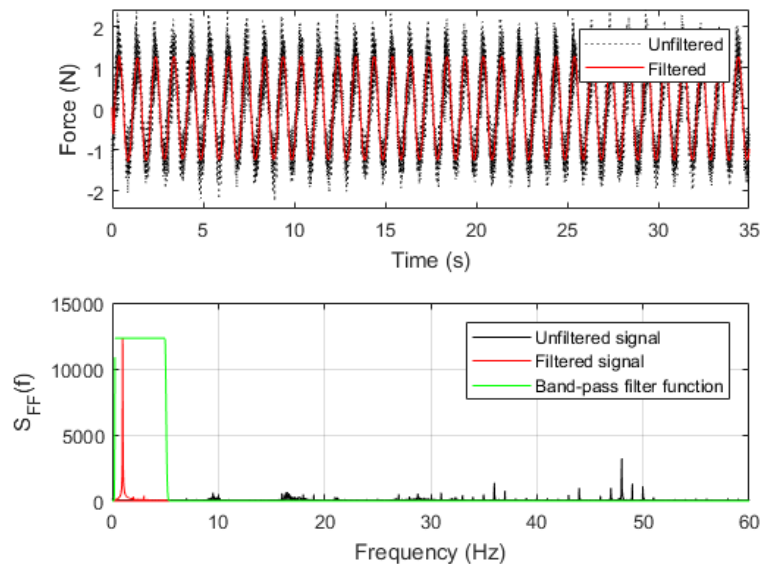
Figure 4.9: Illustration of filtering process in experimental data. Top figure demonstrates the unfiltered with the corresponding filtered time-series. The figure at the bottom illustrate the frequency domain analysis, the range of cut-off frequency has to be selected within the range of frequency of interest

It also can be observed from Fig. 4.9 that the noises are located sufficiently far from the frequency of interest, which apparent to appear for frequency $f \geq 10$ Hz. Those noises are mainly come from the rig vibration, electronics and power supplies. Based on the dedicated investigation, it is believed by taking band-pass filter from 0.3 to 5 Hz for all the acquired data in the present study, it will capture only the frequencies that come from the model oscillation and the corresponding fluid reaction.

4.4.5   Rigid-body oscillation

As mentioned before, two vertical accelerometers were used to measure the acceleration at two sides of body (see Fig. 3.5.1). Using the first order motion approximation from Eq. 2.12, the angular acceleration $\ddot{\eta}_4$ is possible to be obtained only by utilizing one accelerometer. In order to increase the accuracy, the angular acceleration was determined by taking the average between angular accelerations from both of the accelerometer (see Fig. 4.10). This is mainly because the locations of the red dots in Fig. 4.10 are not exactly known, which introduce uncertainty in parameter l_{acc}.
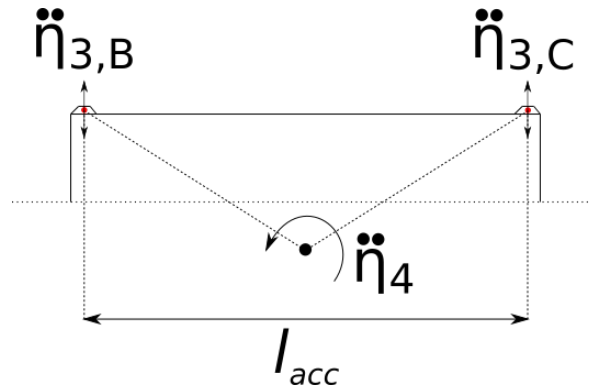
Figure 4.10: Determination of angular acceleration from two vertical accelerometers

The average of angular acceleration from both accelerometers can be mathematically described as:

$$\ddot{\eta}_4 = \frac{\ddot{\eta}_{3,b} - \ddot{\eta}_{3,c}}{l_{acc}} \tag{4.3}$$

If the harmonic motion is considered, the corresponding angular velocity $\dot{\eta}_4$ and rotation η_4 can be obtained by integrating once and twice respectively.

4.4.6   Hydrodynamic coefficients extraction

Similar with Eq. 3.6, but since in the model test the excitation force sensor measure the total applied force to rotate the model, the equation now become:

$$(I_{44} + A_{44})\ddot{\eta}_4 + B_{44}\dot{\eta}_4 + C_{44}\eta_4 = M_4 \tag{4.4}$$

with I_{44} represents the inertial force of the body due to the change of velocity.

Since Eq. 3.7 and 3.8 can also be used for the equation above, the hydrodynamic coefficients from experiment can be obtained by:

$$A_{44} = \frac{\int_0^{nT}(M_4(t) - I_{44}\ddot{\eta}_4 - C_{44}\eta_4)\ddot{\eta}_4(t)dt}{\int_0^{nT}\ddot{\eta}_4(t)\ddot{\eta}_4(t)dt} \tag{4.5}$$

$$B_{44} = \frac{\int_0^{nT}M_4(t)\dot{\eta}_4(t)dt}{\int_0^{nT}\dot{\eta}_4(t)\dot{\eta}_4(t)dt} \tag{4.6}$$

The sensitivity of the chosen time window for hydrodynamic extraction was investigated. This is mainly due to the uncertainty that might be introduced by the acquired time series from the experiment, which for some cases appeared to be not steady enough. This most likely caused by the limitation of the actuator for being not fast enough (see Section 4.5). The illustration of the selected time window is given by the Fig. 4.11 below.
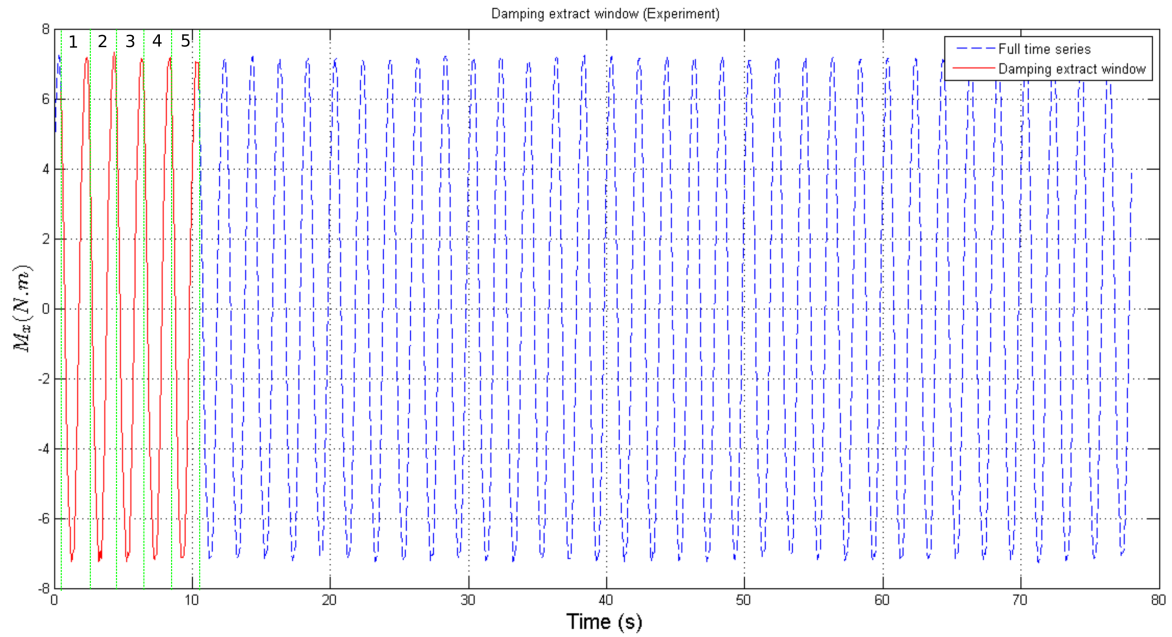
Figure 4.11: Selection of time window from the whole time series for hydrodynamic coefficients extraction. The red line, which represents five oscillating periods, will be used in the further calculation.

The time window sensitivity study cases were done for 1, 5, 10 and 20 oscillating periods. With each time window case, the damping and added-mas coefficients are extracted and compared with the other window cases. The study only limited for the forced roll cases with forcing periods T = 1.0 and 2.0 secs, which are considered as the cases where the fastest and slowest actuator motion produced, and assume that the results are valid for all the cases. In addition, since the parabolic beaches capacity in dissipating wave energy was not quantified (see 4.5),

case where T = 2.0 secs gives insight of how sensitive the time window selection with respect to the waves reflection.

Based on Fig. 4.12 and Fig. 4.13, the extracted coefficients suggest minor dependency of the selected time window length. The differences are only within the range of 1-5 %, which sufficiently small enough. In conclusion, the damping extraction technique in Eq. 4.5 and 4.6 are robust enough to extract the hydrodynamic coefficients, since they based on the mean work done by the roll motion in some period of time.
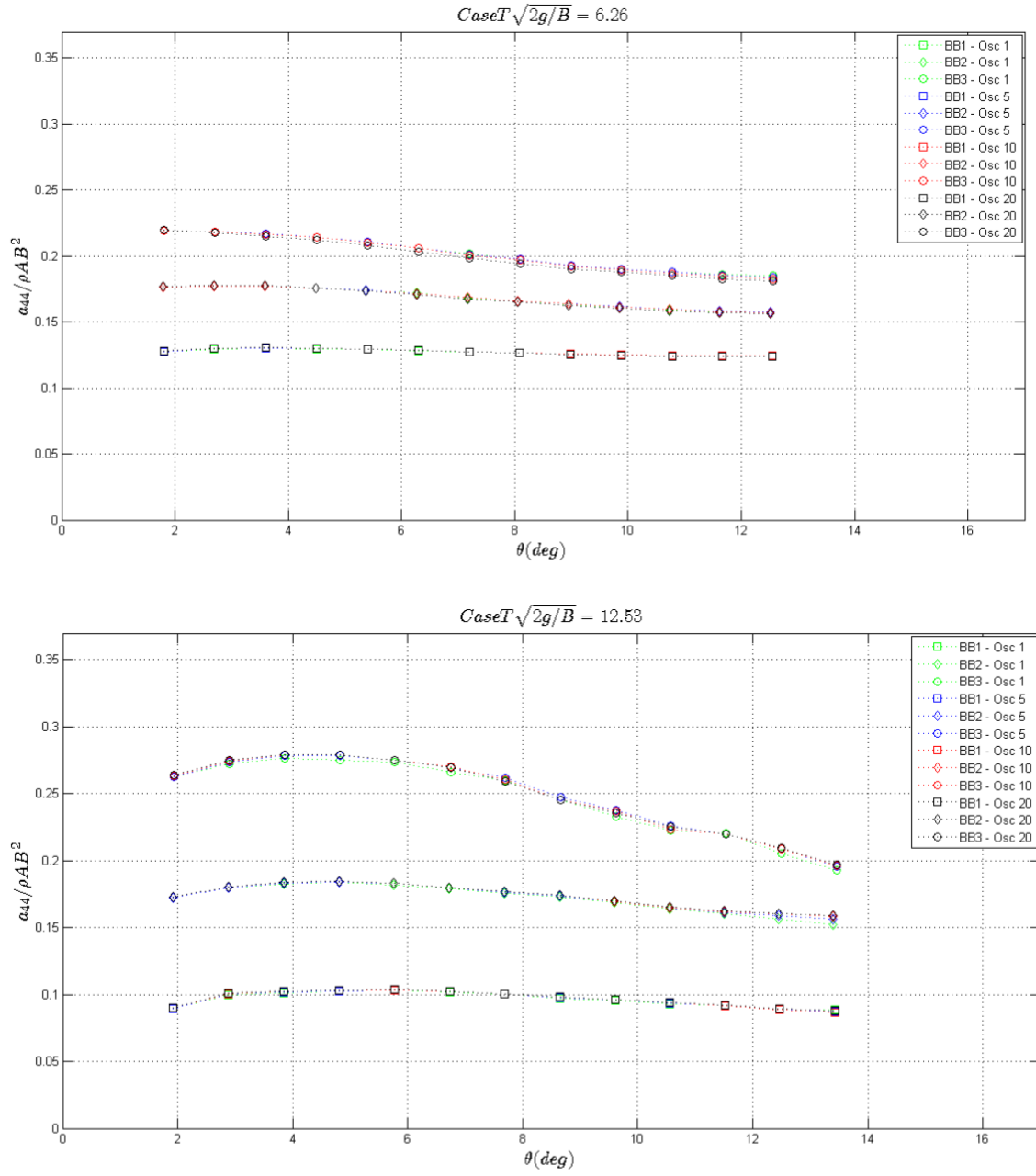
Figure 4.12: Results of added-mass coefficients based on several time window selections
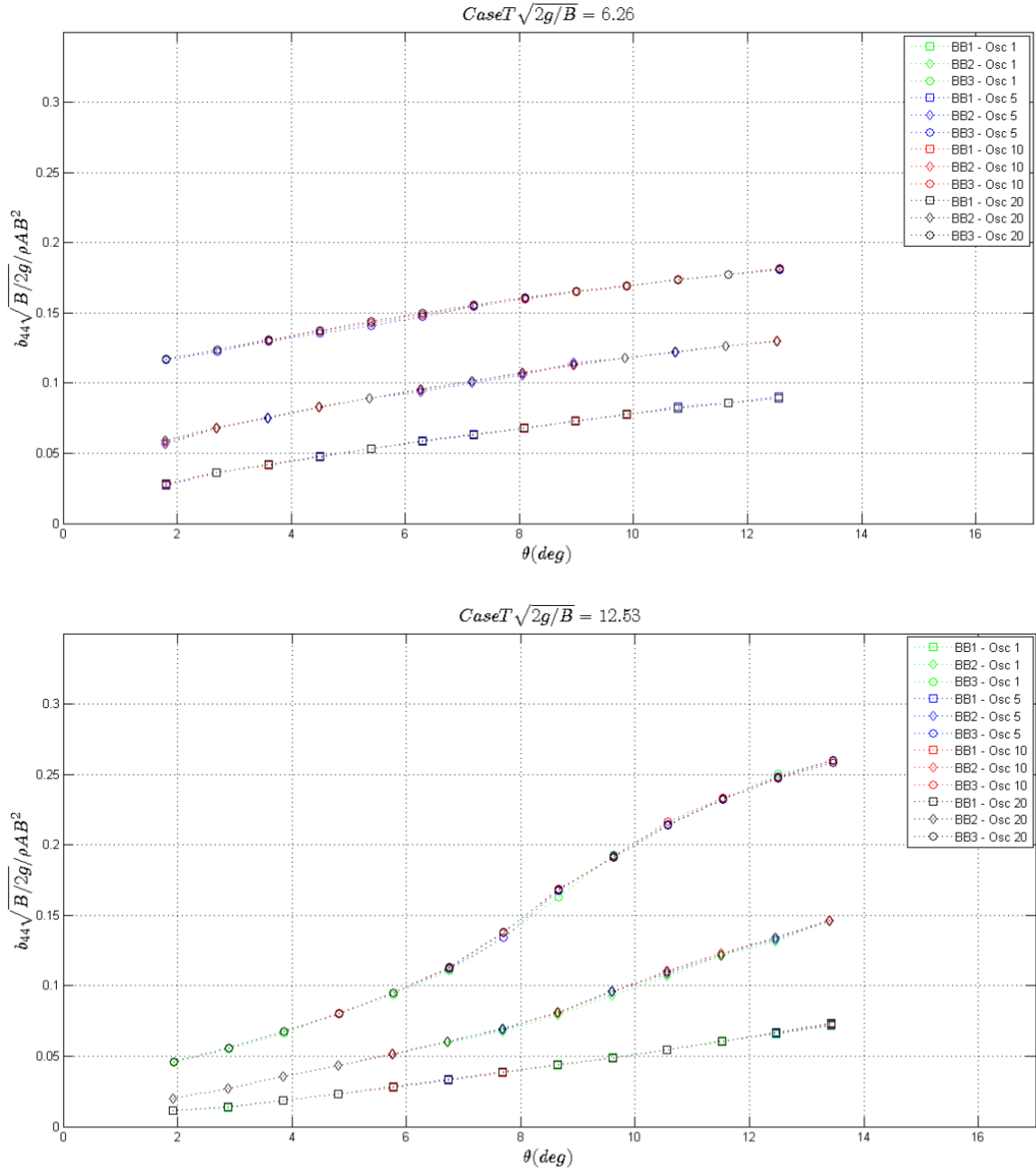
Figure 4.13: Results of damping coefficients based on several time window selections

4.5 Error sources discussion

There are two types of errors that need to be carefully considered when conducting experiment: *precision* and *bias* errors. Precision errors can be quantified by the repetition tests, while bias errors are not revealed by doing such tests.

4.5.1 Precision errors

Due to the time constraints and the error analysis is not a fundamental part of the present study, the repetition tests were done once for one test condition and assume that the precision error found is applicable for the other condition. Some reconstruction of the tests were done by disassemble and re-assemble the setup to introduce the human error that might appear during the process.

Fig. 4.14 below shows the comparison of the damping coefficient results from both of the April 2017 tests and May 2017 repetition tests with the corresponding standard deviation. The BB3 bilge boxes was chosen as the repetition tests case, repetition tests were done for all forcing amplitudes and periods that also used in April 2017 tests.
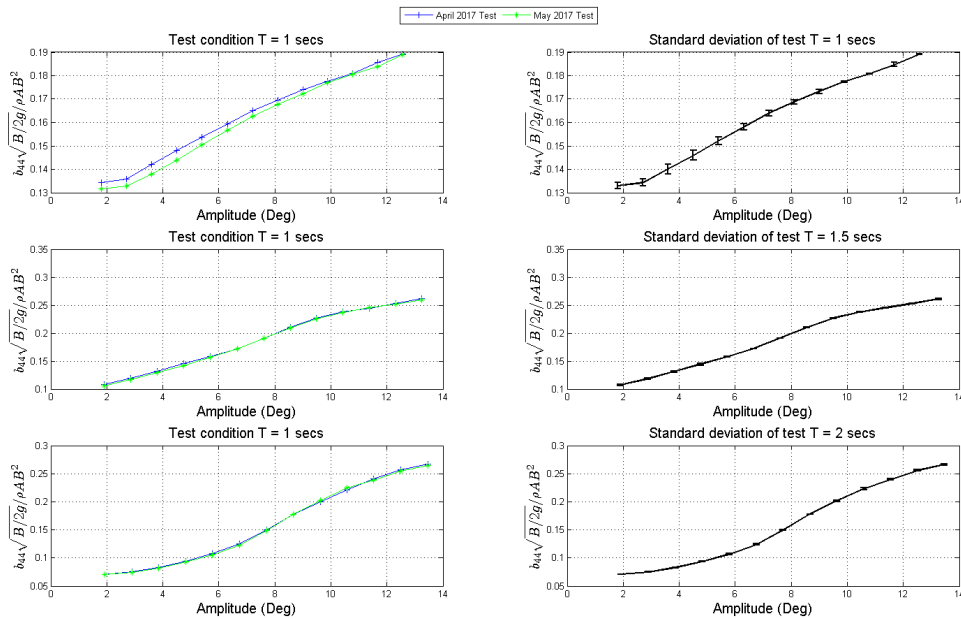
Figure 4.14: Some of the comparison results of the damping coefficients based on April 2017 and May 2017 tests including the corresponding standard deviation

Student's t distribution with N-1 degrees of freedom and 95% confidence level is used to quantify the precision of the tests. Summary of the uncertainty calculation for all the cases is given in the Table 4.3 below. It shows that the maximum uncertainties are within the range of 10-18%.

It is believed that the uncertainty of the damping coefficients is due to the error propagation

Table 4.3: Table presents the maximum and minimum value of uncertainty that found based on the April 2017 and May 2017 tests.

Test condition	Minimum Uncertainty (%)	Maximum Uncertainty (%)
BB3 - T=1.00 secs	0.23	17.92
BB3 - T=1.15 secs	2.11	12.22
BB3 - T=1.35 secs	0.75	14.98
BB3 - T=1.50 secs	0.0059	14.58
BB3 - T=1.70 secs	1.19	13.87
BB3 - T=1.85 secs	0.12	10.78
BB3 - T=2.00 secs	0.48	14.76

from the components that arrange the equation. Hence, a look through time series of some cases has been done. Case BB3 with T = 1.00 secs was chosen as the sample, which shows the largest uncertainty among all the tests. The roll angle, angular velocity, angular acceleration and moment time series are given in Fig. 4.15 below. At a glance, the time series comparison shows a good agreement which indicates that the test quality is sufficiently high. Thorough investigation has not been done to identify the problem, but as stated in Kristiansen et al. (2014), the damping coefficient extraction is sensitive to phasing problem. Dedicated study of uncertainty analysis of damping extraction from model test results is needed in the future.
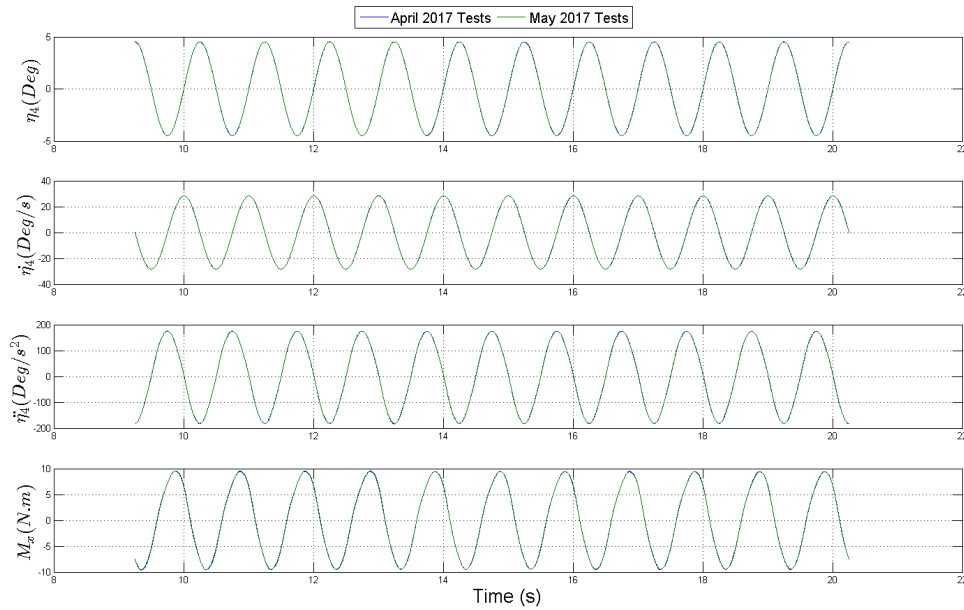

Figure 4.15: Time series comparison between April 2017 and May 2017 for case BB3 with T = 1.00 secs

The easiest way to reduce the uncertainty is to do several repetition tests. Since only one set of repetition tests has been done, the calculated standard deviation and uncertainty has considered to be not enough. The standard deviation will be expected to increase but become

less uncertain with the increment of number of samples. This may improve the random error quantification of the model tests, and become more reliable to be applied for the design consideration.

4.5.2 Bias errors

Several bias errors will be discussed in this Sub Section. Identifying the limit of the laboratory set up and equipment based on the obtained data, discussion with the experience laboratory user, and also visual observation during the model test has been attempted in order to get the quantification of errors.

Actuator acceleration was found to be 1 m/s^2, which will be achieved by the actuator for forcing period longer than 2 seconds. Unfortunately, the forcing periods in present study were less than 2 seconds, meaning that they exceed the actuator capacity. The apparent consequence was the desired rotation angles were not achieved, this clearly can be seen from the obtained data. It could also be connected to the higher harmonics that appear in the motion, since the motion characteristic may alter from the one that imposed.

Agreement between the physical-mathematical model was investigated to be important in the body rotation - actuator translation mechanism, since it involves the geometry parameter inside the equation. This was found by help from Babak Ommani, who investigated this problem with author after observed some significant energy in higher harmonics (second, third, fourth, etc.) from January 2017 test results. The conclusion was if some of the geometry inputs in Eq. 4.1 is slightly different with the one in the physical system, the resulting angular acceleration will contain higher harmonics. Efforts has been made to reduce the higher harmonics by improving the geometry measurement accuracy, new rig attachment design for the model to be accurately positioned every time changing the appendages (designed by Tobias Rasen Borgenhov, NTNU), which was found to be effective but still could not completely remove the higher harmonics.

The parabolic beaches that are installed in present study was found to be effective only for the waves with period more than 1.5 secs (Kristiansen (2009)). The performance of parabolic beaches were not investigated in the present study, but based on the visual observation and inspection on some of the results, the waves were not break properly for shallow water waves. This may change the fluid behavior and affect the results.

Mechanical friction damping was introduced by the rotary bearings that used during present study. This gives additional damping to the system, which is apparent to be nonlinear based on the results analysis. No quantification has been made to tackle the problem.

Chapter 5

Results and Discussions

5.1 General

This chapter will present the results and the discussions of the forced roll oscillation results that has been done with the model tests from Chapter 4 and numerical model that was discussed in Chapter 3.

The results will be presented in the non-dimensionalized form in the similar way as the work by Vugts (1968), which will be stated in every presented graphs.

In general, only the interesting results will be discussed in this chapter to make the report become more concise, while the rest will be included in the Appendix. Comparison between the model tests and numerical model will be given whenever possible. Some of the works that could not be done during the present study will be discussed briefly and recommended for the further works later on the next chapter.

5.2 Time domain responses

Some results of time series will be given and discussed within this chapter. Ramp-function Eq. 3.5 is used in both of model tests and PVC2D-Roll, and only the steady-state part will be used and presented here. The wave reflection problem in PVC2D-Roll is avoided as discussed in Section 3.5.6. The sensitivity of time window to the hydrodynamic coefficient extraction on model tests also already investigated in Section 4.4.6. Time series from both model tests and PVC2D-Roll are shifted to t=0 secs for the comparison purpose.

5.2.1 Motion

The measured motion of forced roll oscillations are compared with the PVC2D-Roll simulation results. Comparison of the roll angle θ between the model tests and PVC2D-Roll shows good agreement, especially when one observes the peaks position and slope of the sinusoidal motion. The discrepancies of the roll magnitude are occured due to the actuator for being not too

precise, as discussed in Section 4.5.2, hence the desired amplitude would not be achieved if the imposed actuator motion exceeds the speed limit. The motion with the corresponding angular velocity $\dot{\theta}$ and acceleration $\ddot{\theta}$ are presented in Fig. 5.1 below. In addition, the importance of geometry parameter agreement between the physical and imposed mathematical model has already discussed, the additional harmonics contribution appeared in the experiment become more visible in $\dot{\theta}$ and $\ddot{\theta}$ terms. In conclusion, even though the model test motions resemble the one in PVC2D-Roll, the model moves with different velocity and acceleration.
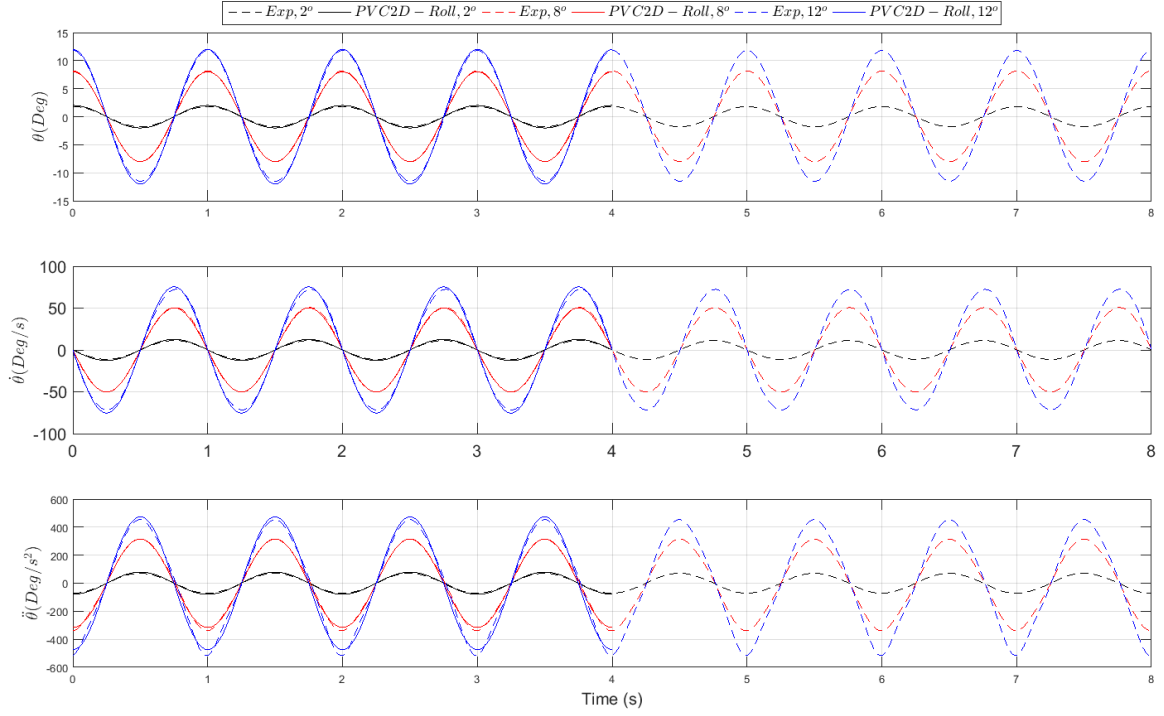

Figure 5.1: Comparison of motion time series for several forcing amplitudes with $T\sqrt{2g/B} = 6.26$

5.2.2 Forces

By subtracting the I_{44} and C_{44} terms from Eq. 4.4, the hydrodynamic roll moment (M_4 in Eq. 4.4) from model tests can be compared with PVC2D-Roll results. The BB2 case time series comparison, for instance, for four roll amplitudes and three periods are illustrated in Fig. 5.2, 5.3 and 5.4. Results from both model tests and PVC2D-Roll agree for some extent. As expected, with higher frequency and/or amplitude of motion, gives higher roll moment. Both methods show constant shift and skew of the moment time series with increasing amplitude, this indicates the viscous effects and flow separation become more prominent for increasing amplitude.

In general, discrepancies are clearly visible from the time series. Firstly, the roll amplitude between model tests and PVC2D-Roll are not similar, this due to the actuator limitation in model tests (see Section 4.5.2). Secondly, another plausible explanation of differences are

due to the different angular velocity and acceleration between model tests and PVC2D-Roll (see Section 5.2.1), this may clearly cause different moment time series since fluid reactive forces that proportional to body velocity and acceleration are not being pure harmonic. In PVC2D-Roll, however, the body motion is assured to be pure harmonic.
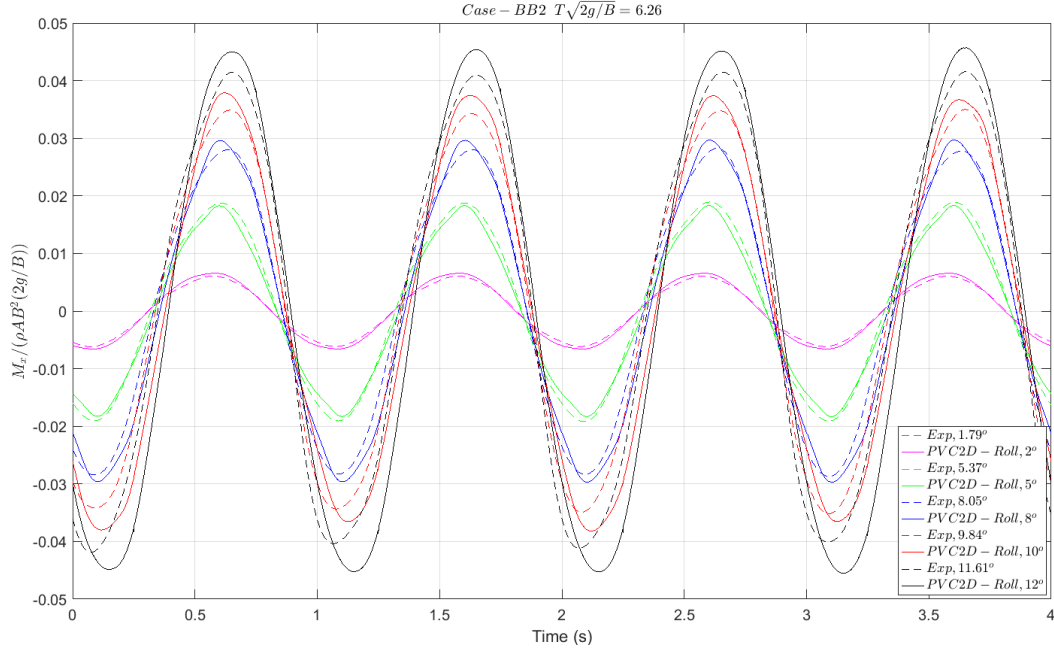

Figure 5.2: Comparison of hydrodynamic moment for case BB2 with $T\sqrt{2g/B} = 6.26$ with several forcing amplitudes
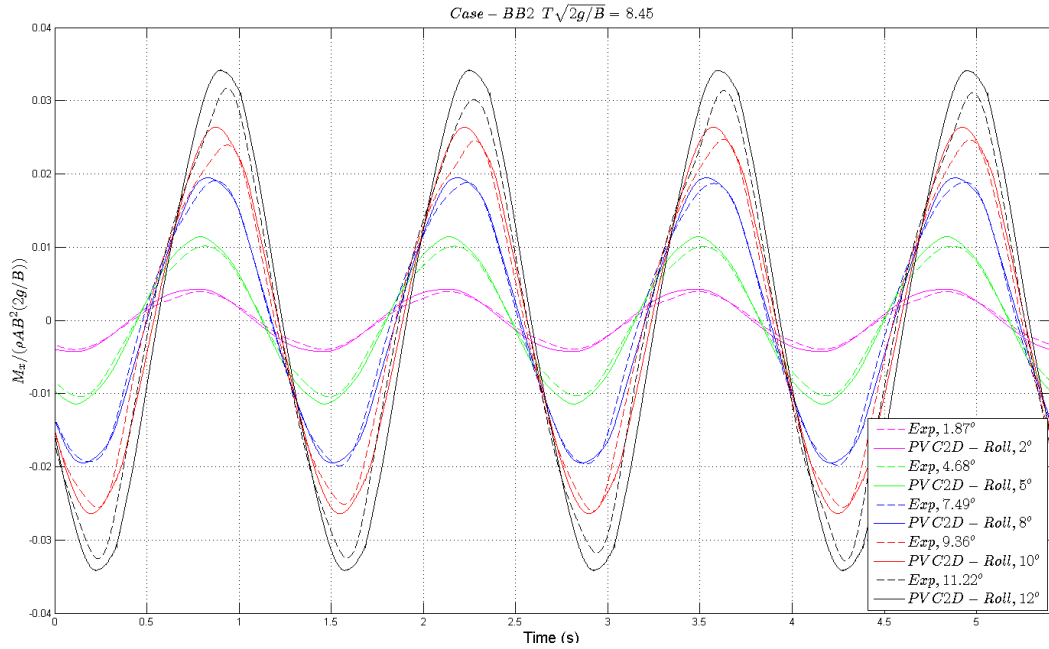

Figure 5.3: Comparison of hydrodynamic moment for case BB2 with $T\sqrt{2g/B} = 8.45$ with several forcing amplitudes
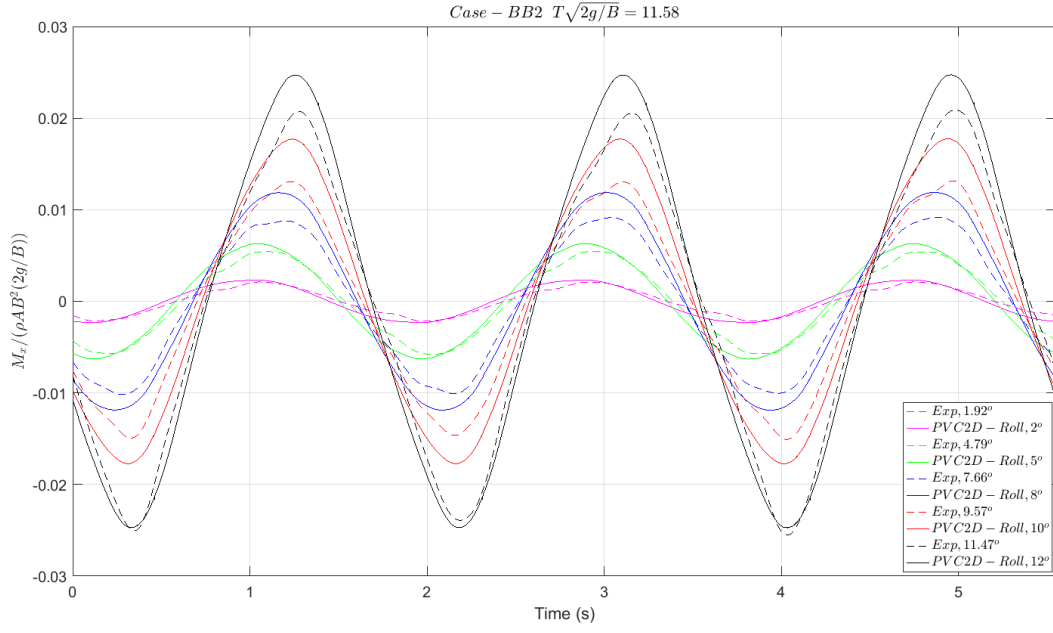
Figure 5.4: Comparison of hydrodynamic moment for case BB2 with $T\sqrt{2g/B} = 11.58$ with several forcing amplitudes

Normal forces on the bilge-boxes are also obtained in present study. In PVC2D-Roll, the hydrodynamic forces are obtained from the integration of dynamic pressure, and translate the obtained force into the body-fixed coordinate normal to bilge-boxes. For model tests, the dry tests in air were performed to obtain the inertia of the bilge-boxes including the connector constructions. The hydrodynamic forces can be obtained by subtracting the inertia loading by the measured forces in water tests. The force on each side (port and starboard) is calculated by adding the measured forces from the sensors located on the respective side. Based on the obtained data observation, the calibration factor of strain gauges D (see Fig. 4.4) has drifted, and consequently gives lower force reading in port side. It is believed that for the pure harmonic motion, the bilge-boxes forces time series on port and starboard sides should be similar in magnitude but opposite in sign. This become evident in Fig. 5.5, for instance, where strain gauges A, B and C gives similar range of force reading. Hence, bilge-boxes force on the starboard side is considered sufficient for the further discussion.

The obtained bilge-boxes BB2 forces on starboard side for several forcing amplitudes and periods are presented in Fig. 5.6, 5.7 and 5.8. The flow separation becomes more apparent in the time series, this indicated by the time series skew become more visible within this case. Both methods give quite well comparison in general, even though some differences are already expected based on the previous discussion.
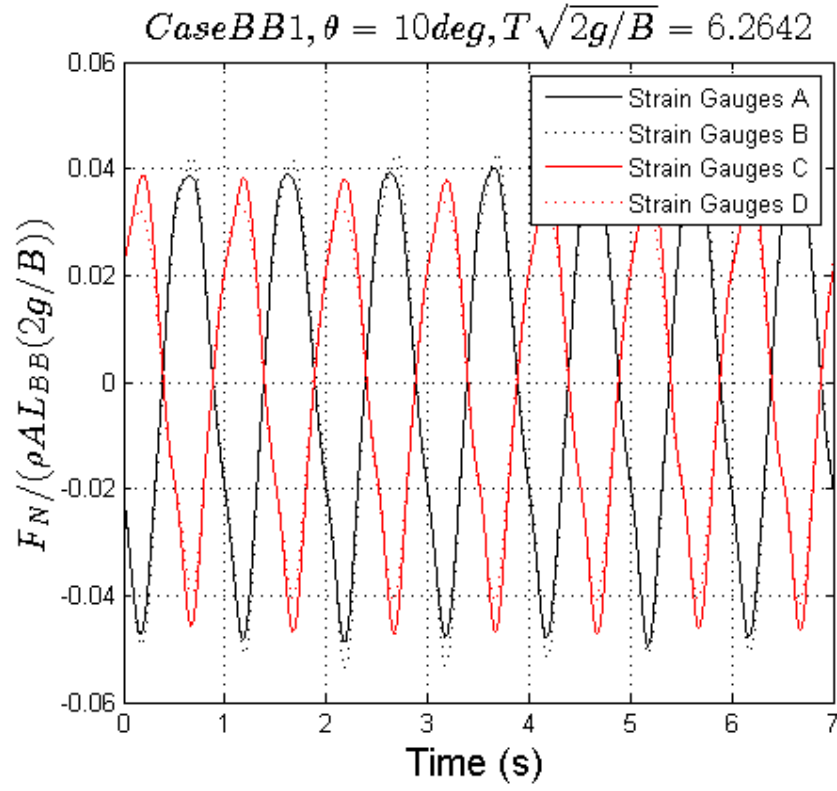
Figure 5.5: Comparison of hydrodynamic forces obtained from all the strain gauges in model tests. Sensor D gives lower value of force due to the calibration factor drifting
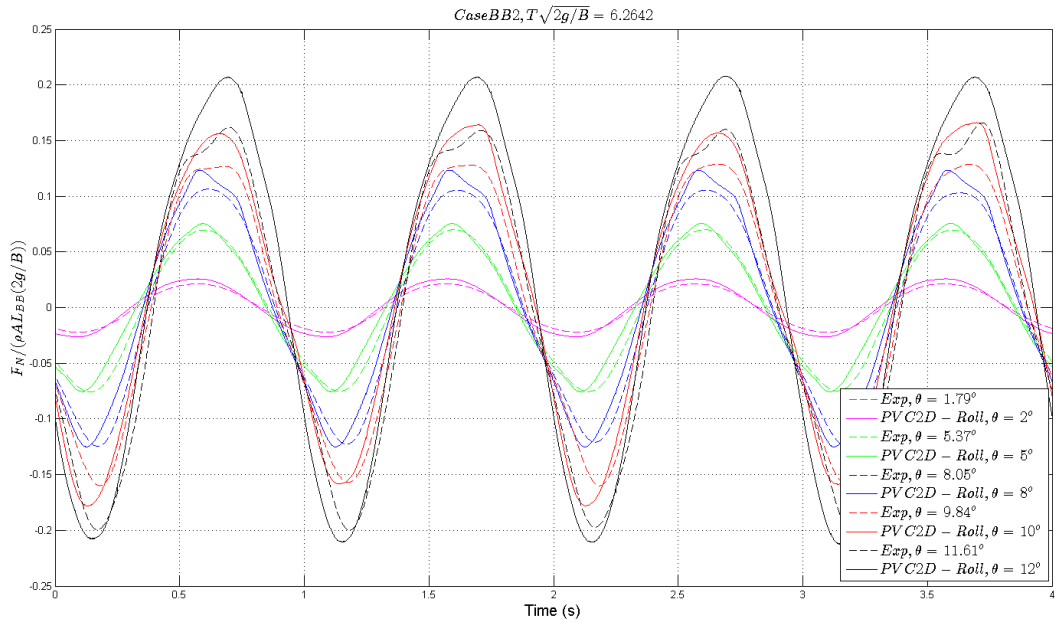

Figure 5.6: Comparison of the bilge-boxes normal force on the starboard side for case BB2 with $T\sqrt{2g/B} = 6.26$ with several forcing amplitudes
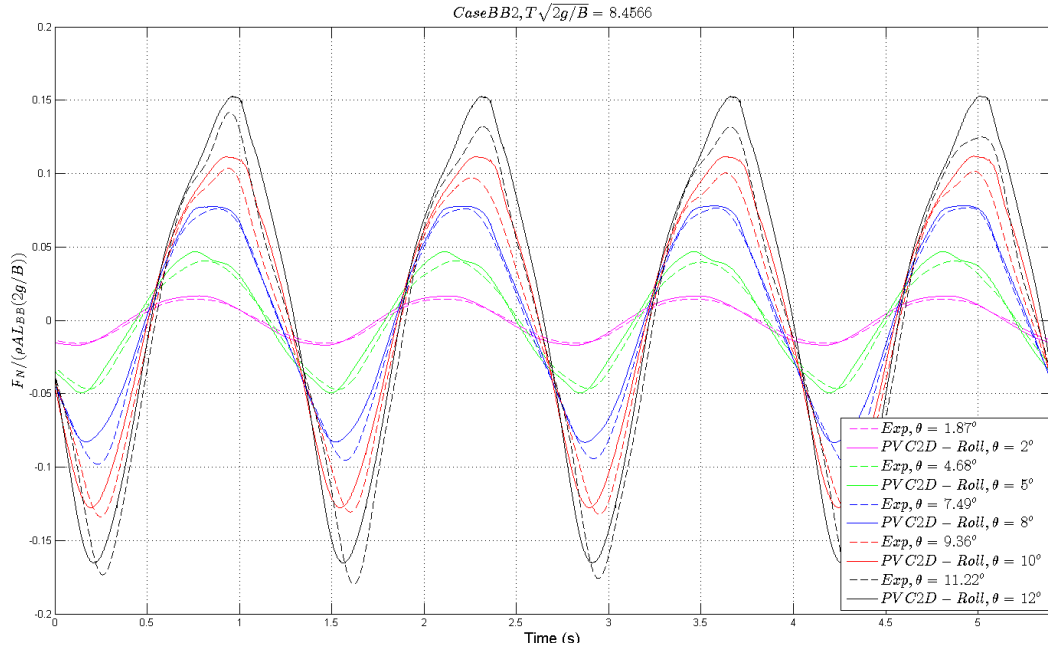
Figure 5.7: Comparison of the bilge-boxes normal force on the starboard side for case BB2 with $T\sqrt{2g/B} = 8.45$ with several forcing amplitudes
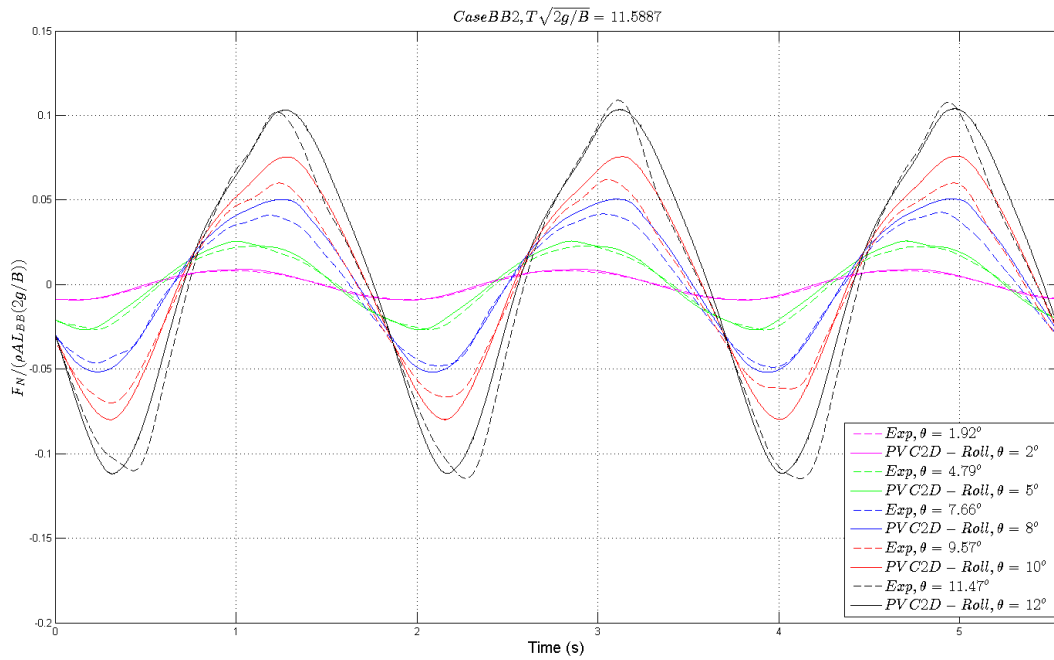
Figure 5.8: Comparison of the bilge-boxes normal force on the starboard side for case BB2 with $T\sqrt{2g/B} = 11.58$ with several forcing amplitudes

5.2.3 Wave elevation

Wave elevation is another quantity that acquired during model tests and numerical simulation, which can be utilized to find the damping due to the waves radiation (see Section 2.7.3). In the present study, PVC2D-Roll results give some unphysical discontinuity in the dynamic

pressure field away from the body, this consequently affects the obtained wave elevations. The problem is obviously comes from the numeric, and was not investigated any further. One of the results can be seen in Fig. 5.9 below. The discontinuity is apparent, but the predicted values are somewhat comparable, especially for the small amplitude waves.
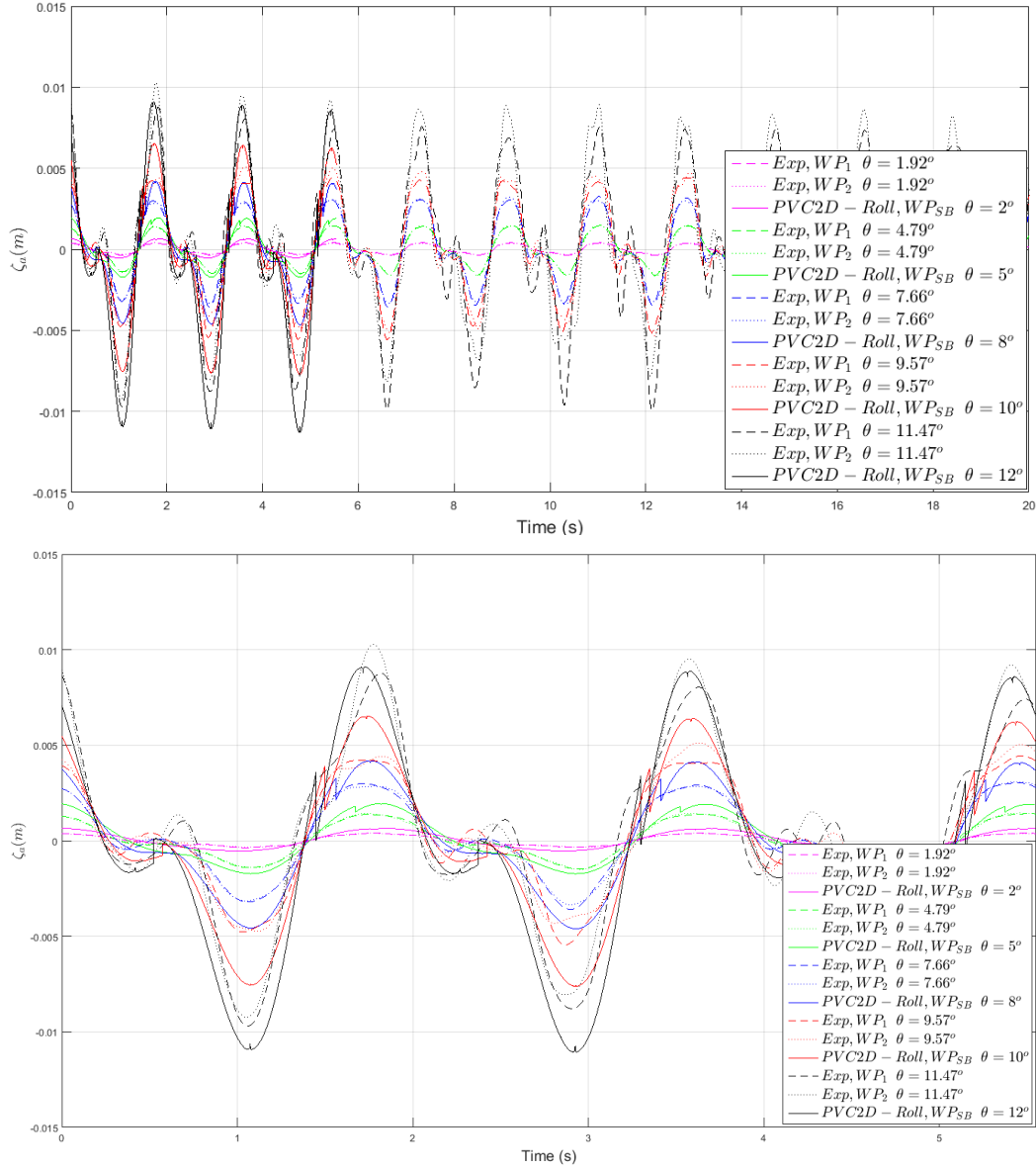

Figure 5.9: Comparison of the wave gauges on the starboard side for case BB2 with $T\sqrt{2g/B} = 11.58$ with several forcing amplitudes

5.3 Unwanted damping component removal

The method to remove unwanted damping (see Section 4.5.2) that existed on the system will be explained in this section. Thorough investigation about this mechanical friction feature has not been done, but by utilizing another known quantities it is not impossible to approximately

remove this unwanted component.

The damping components of the model without bilge-boxes can be estimated to comprise of wave radiation B_W, skin-friction B_F and unwanted B_{UW} damping from bearing and mechanical friction. The interaction among of them are assumed to be neglected. This kind of component analysis has also been practiced by Ikeda et al. (1976, 1977b,a, 1978) in his extensive studies on damping of bilge keels. Extracted damping coefficients from model tests and PVC2D-Roll for model with rounded corner is presented in Fig. 5.10 below.
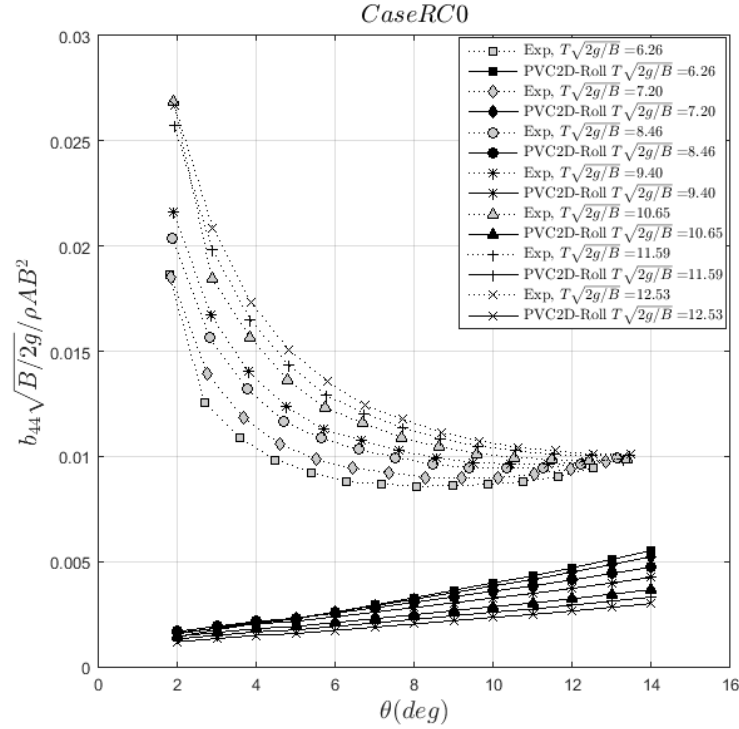

Figure 5.10: Variation of roll damping with amplitude and period of oscillations for the case of body with rounded corner

As one may observe from figure above, model test results demonstrate damping coefficients differently compared to the PVC2D-Roll. PVC2D-Roll results, at least, show more correct damping behavior. When body rolls with increasing amplitude, the B_F part will become more pronounce, and resulting in higher damping. Moreover, the body motion frequency also dictates the vortex that shed from the body, the faster it moves, the higher damping felt by the body. Viscous effects become not important if the body does not shed any vortex, meaning that the damping when $\theta = 0$ in figure above should represent only wave radiation damping. According to experiment results by Vugts (1968), beam-to-draught ratio of the body that used in present study should gives approximately zero wave radiation damping. PVC2D-Roll once again predict the behavior correctly, while the model tests results suggest increasing damping. The damping also become more prominent when the body oscillates slower. It is now obvious that the unwanted friction damping presents on the model tests. It

is also interest to note another aspect that the model tests results show higher damping, this is believed due to the scale effects that come from the surface roughness in the real problem, while smooth surface is assumed in PVC2D-Roll.

Four assumptions will be made to treat the model tests results. Firstly, body moves with similar motion for every amplitudes and periods. Secondly, the skin friction damping is small relative to damping that introduced by bilge-boxes, this holds true for most of the cases. Thirdly, the wave radiation damping from bare-hull body is very small. Lastly, the unwanted damping gives the same contribution for specific roll amplitude and period, no matter which bilge-boxes are attached. Finally, if the body with bilge-boxes has the same damping components but with additional bilge-boxes pressure damping B_{BB}, the unwanted damping can be removed by subtracting the obtained coefficients with the damping from the body with rounded corner ($RC0$) results. The damping information from B_F and B_W from $RC0$ corner definitely will disappear, but those quantities are almost negligible compare to B_{BB}. To be fair, the PVC2D-Roll results for cases with bilge-boxes also will be subtracted by the simulated $RC0$ cases. All results presented later will be based on this correction.
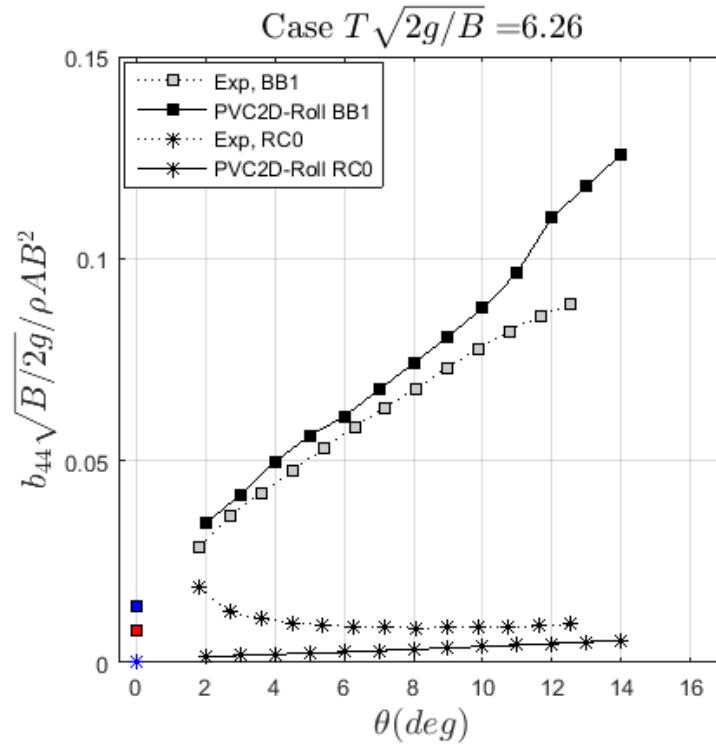

Figure 5.11: Resulting damping coefficients after the correction. Red and blue symbols represent estimated wave radiation damping based on Section 2.7.3. The wave radiation and skin-friction damping coefficients of $RC0$ are negligible compare to the damping of BB1. Results of rounded corner $RC0$ are not corrected and represent the original values obtained from both tests.

5.4 Hydrodynamic coefficients

5.4.1 Damping coefficients

The damping coefficients B_{44} term variation for different parameters are investigated. The goal is to define the damping dependency on the investigated parameter: amplitude, period and bilge-box length. Results are extracted based on the time series discussed on Section 5.2.1. Damping coefficients presented include wave radiation damping, and can be approximated by energy relations as discussed in Section 2.7.3 will be presented within the graphs. All the presented values are in the non-dimensionalized form. For more results, see Appendix B and D.

Effect of roll amplitude and period

The roll damping dependency on amplitude and period is demonstrated by Fig. 5.12 below, BB1 case is taken as an example for discussion. Both of model tests and PVC2D-Roll damping curves suggest approaching wave radiation damping when roll amplitude goes to zero. In general, the bilge-boxes influence the body capability in generating waves and decreasing with larger period oscillations. The discrepancies between estimated wave radiation damping from model tests and PVC2D-Roll are obvious for $T\sqrt{2g/B}$ =6.26 and 7.20, this is due to PVC2D-Roll predicts higher generated waves than the one that obtained in model tests (see Fig. 5.9 for instance).

The curves above show quadratic behavior, which increasing with amplitude. This is mainly due to the flow separation from the bilge-boxes. Based on the model tests results, slope changes on the damping curve of the lowest period can be found in the high amplitude range. This was also identified in Ommani et al. (2016a) in their study of two-dimensional FPSO cross-section with sponsons. They believe that the free surface starts to contribute in flow separation. This could be true for the present study, the bilge-boxes start to pull the free-surface down for sufficiently high amplitude and frequency motion. This evidenced on the video documentation from February 2017 test with the same period and amplitude case. On the other hand, the PVC2D-Roll results suggest higher damping value in high amplitude range. It was suspected that PVC2D-Roll simulated free-surface differently and could change the local velocity at the bilge-boxes tip, i.e. radiated waves system from the body, bilge-boxes and their interaction.

The bilge-boxes forces measurement in Fig. 5.14 can also support the statement above, which represented by the mean bending moment at the bilge-boxes root curves. The mean bending moment was calculated by averaging crest and trough of moment time series. The figure suggests that by increasing the amplitude and period increases the bending moment quadratically, and this mainly due to the viscous effects. Clearly, PVC2D-Roll gives higher force measurement for sufficiently high roll amplitude, while predicts similar trend and magnitude with model tests on the other range. One candidate is that the linear free-surface assumption
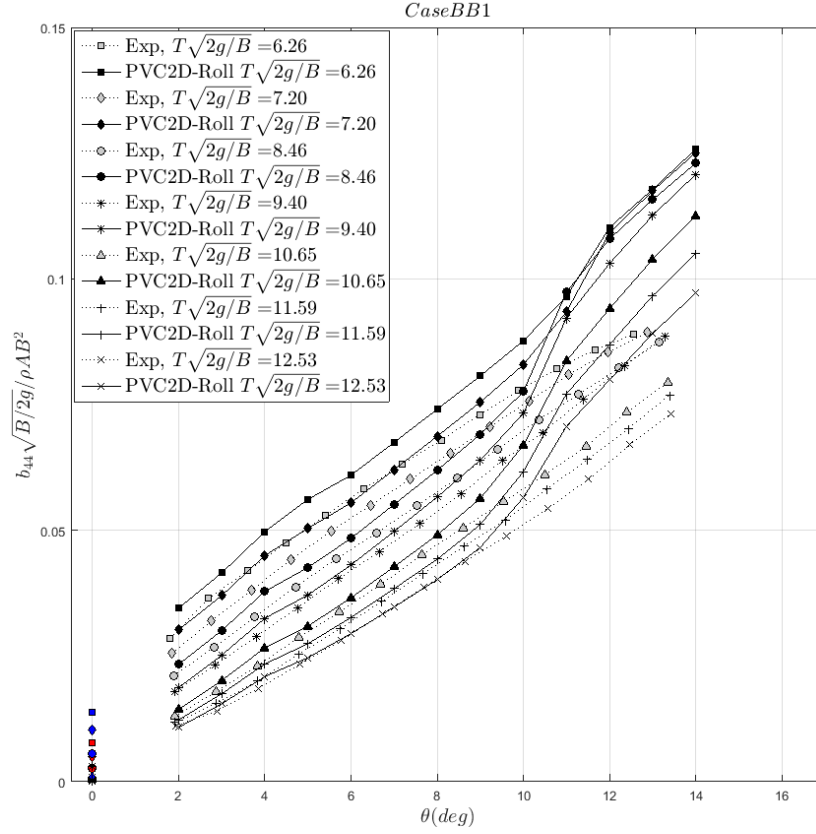
Figure 5.12: Roll damping curve for BB1 case with respect to varying roll amplitude. Red and blue symbols on zero roll amplitude represent wave radiation damping.

in PVC2D-Roll is not sufficient to model local velocity that comes from local body motion, and suspected that the disturbed free-surface has contribution in changing the local velocity. This need to be validated with a dedicated study of local velocity and free-surface effects observation to get more detailed insight.

The damping dependency on period is presented in Fig. 5.15. The roll damping shows larger magnitude for higher amplitude, while the decreasing trend for increasing period is expected. This related to the strength of flow separation due to the local body motion. PVC2D-Roll gives good trend prediction and comparable to the model tests results, the discrepancies of the high roll amplitude between both methods also already discussed.
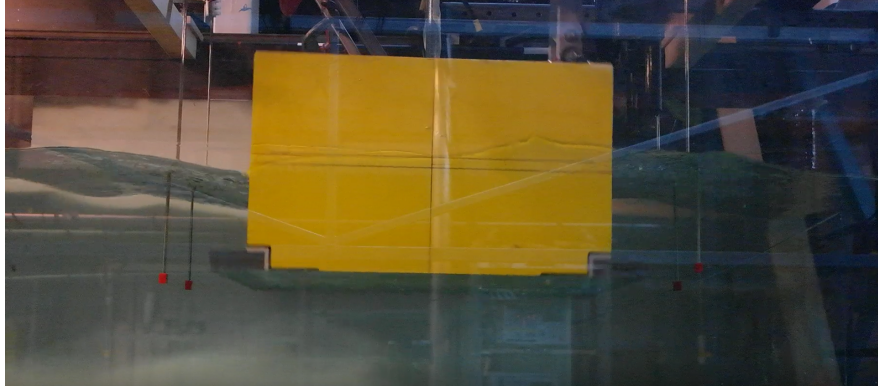
Figure 5.13: Video documention from February 2017 test. The BB1 case with $\theta = 13^o$ and $T\sqrt{2g/B} = 6.26$ shows that the free-surface is pulled down by the bilge-boxes.
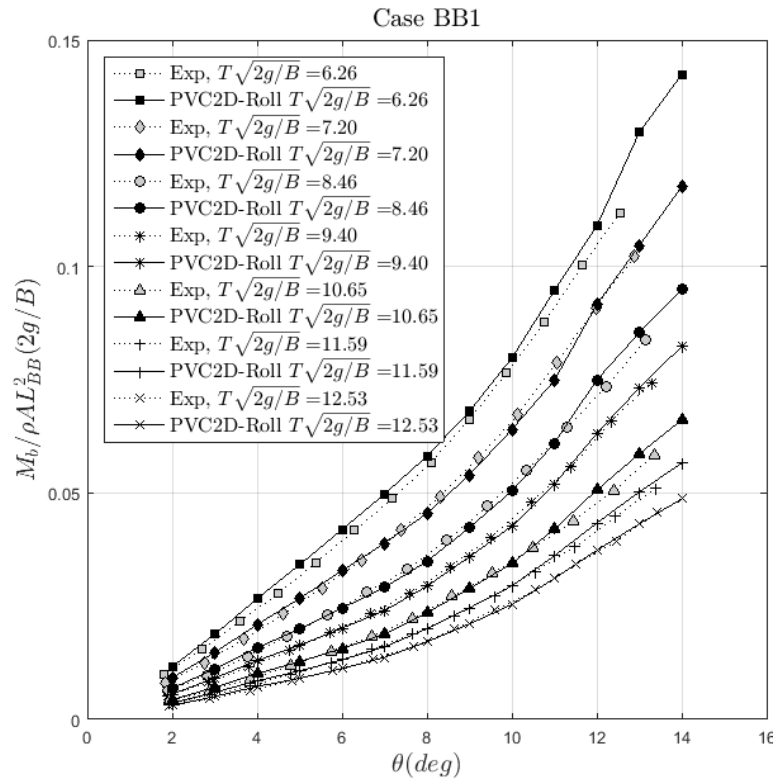

Figure 5.14: Variation of bilge-boxes bending moment with respect to roll amplitude and period.
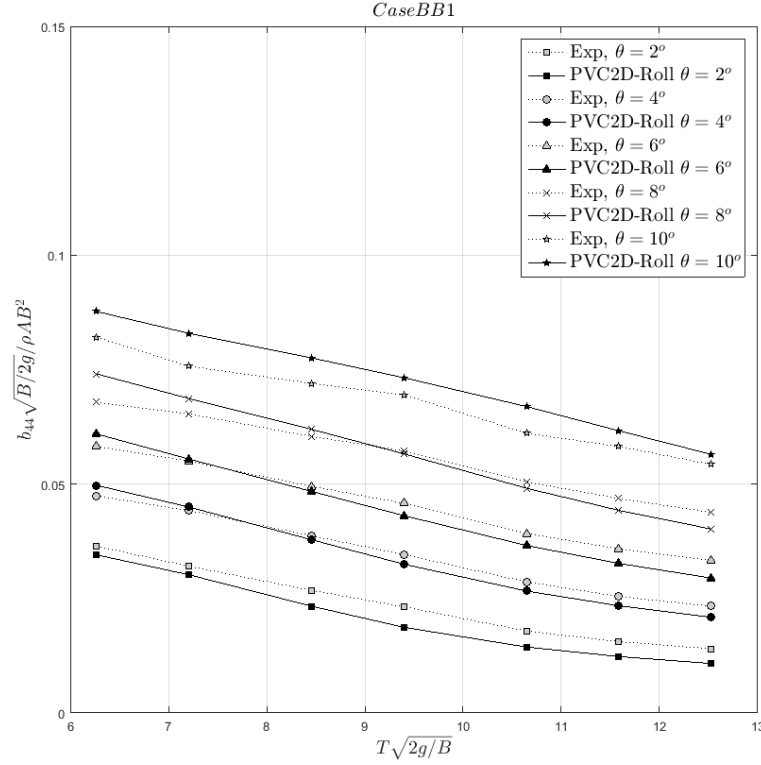
Figure 5.15: Roll damping curve for BB1 case with respect to varying roll period.

Effect of bilge-boxes length

Length of the bilge-boxes also becomes one of the interests in the present study. In the case of longer bilge keels, the bigger roll damping is obtained. Whereas, it is still questionable for bilge-boxes. Three bilge-boxes length are considered in present study, BB1, BB2 and BB3. The characteristic dimensions are the one that already explained in Table 3.1. Fig. 5.16 shows how roll damping varies with the bilge-boxes length for different roll amplitudes and periods of oscillations.

By introducing longer bilge-boxes, the wave radiation damping becomes bigger. It is also expected to decrease with longer period of oscillations. The discrepancies between the wave radiation damping between both methods need to be investigated more, especially for the largest bilge-boxes results, i.e. by using potential-flow solver like WAMIT. The wave gauges position are also considered too close with the model, hence the evanescent mode is expected has not decayed yet and disturb the measurement (see Section 2.7.2). Fig. 5.16 demonstrates that the capability of body in generating waves also influence the damping curves slope, while the increment of damping with respect to roll amplitudes is expected. The slope increment indicates the dominance of quadratic damping, compare to linear wave radiation damping.

One interesting discovery of introducing longer bilge-boxes is the damping dependency on period become strongly amplitude and period dependant, while that is not necessarily the case for BB1 as shown in Fig. 5.15.
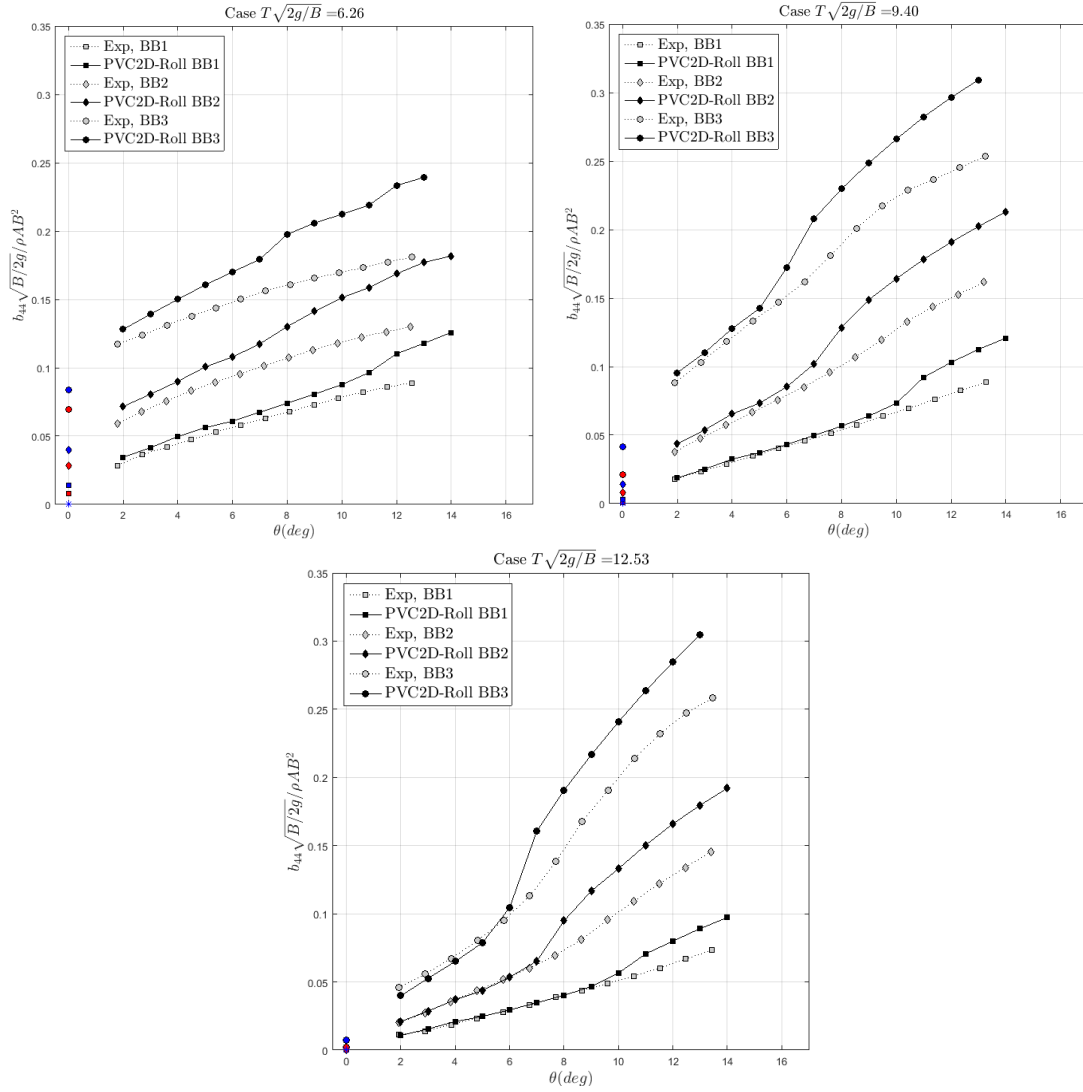
Figure 5.16: Variation of roll damping with bilge-boxes length, roll amplitude and period of oscillations.

Figures above suggest that for sufficiently low amplitude, both for BB2 and BB3 cases, the damping decreases with increasing period of oscillations. This is quite similar with the one that found in case BB1. Slope of decrement starts from smaller period for case BB2, and becomes flat again for $T\sqrt{2g/B} > 10.65$. On the other hand, BB3 shows the opposite way, where the plateau is located at the range of $6.26 < T\sqrt{2g/B} < 9.40$. While different trend is clearly seen for higher roll amplitudes, BB3 damping coefficients indicate increasing trend at the lower period, and start to decrease at $T\sqrt{2g/B} = 11.59$ based on model tests results. BB2 cases with high amplitude suggest somewhat constant results, means that the damping coefficients independent of period of oscillations.

This was investigated from the bilge-boxes force measurement, by assuming bilge-boxes "feel" heave movement locally as shown in Fig. 5.18. KC definition is adopted from free plate definition of Keulegan and Carpenter (1958), in this case KC=$\eta_{3,local}\pi/L_{BB}$. From BB2
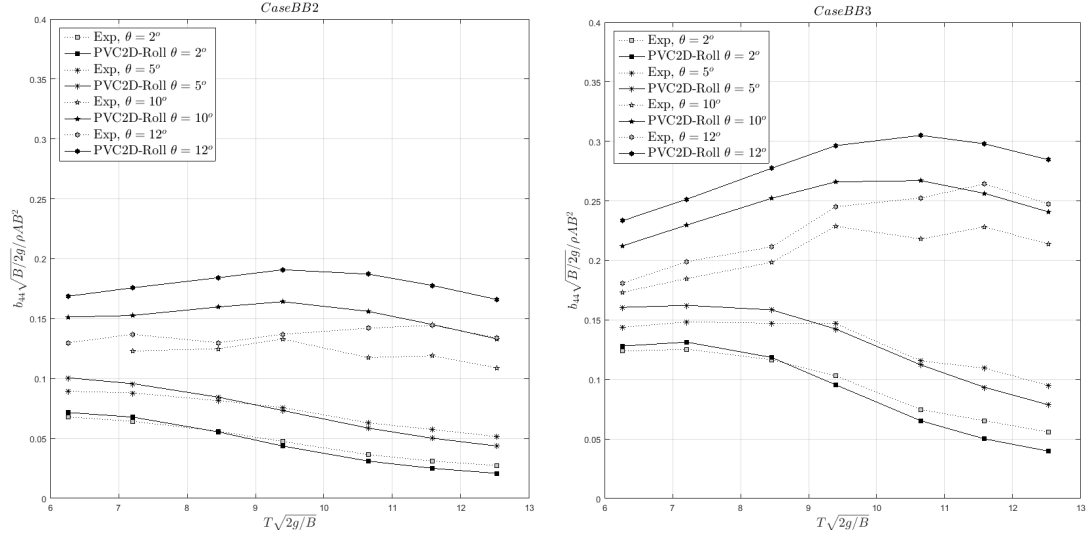
Figure 5.17: Variation of roll damping in BB2 and BB3 case with respect to periods of oscillation for several roll amplitudes

graph on the left, even though for every $T\sqrt{2g/B}$ indicates different slope and crisscrossed each other around KC≈2.1, but they are somewhat in the same range of magnitude. Slope differences are mainly attributed to the quadratic damping due to the flow separation. For BB3 case, the crossing is started earlier in KC≈0.7 which corresponds to roll amplitude approximately 4.5^o. The crossings can explain all the plateaus in Fig. 5.17.

If one has closer look, the slopes change when the body motion is higher relative to the bilge-boxes dimension, means higher KC-number. This also can be seen in Fig. 5.16. One of the candidates to explain about this is due to the free-surface effects on bilge-boxes as mentioned before in Section 5.4.1. This is reasonable since with longer bilge-boxes, the lower roll amplitude it needs to reach the free-surface relative to the shorter one. It is not a coincidence that the slope changes in the lower amplitude in BB3 than BB2. From both Figures, the longer period of oscillations resulting in higher damping in higher KC / amplitude range. This suggests the generated wave system from body and bilge-boxes gives higher relative velocity at the bilge-boxes tip for longer period. Dedicated study about the free-surface effects need to be conducted to confirm this point.

Recall Fig. 5.16 and 5.17, PVC2D-Roll results tend to over predict the model tests results in some cases. Discussion about the discrepancies in BB1 cases has been discussed in Section 5.4.1, hence the BB2 and BB3 cases will be emphasized now. For lower period of oscillations in both BB2 and BB3 cases, PVC2D-Roll predicts very well in low amplitude range and starts to get bigger in higher amplitudes. The damping over prediction by PVC2D-Roll starts on where the free-surface is suspected to contribute based on the previous discussion. One plausible explanation regarding this problem is due to the importance of nonlinear free-surface condition modeling, which is not modeled in PVC2D-Roll. This also has been discussed in Section 5.4.1, but its importance become more pronounce for the longer bilge-boxes. Fig. 5.19
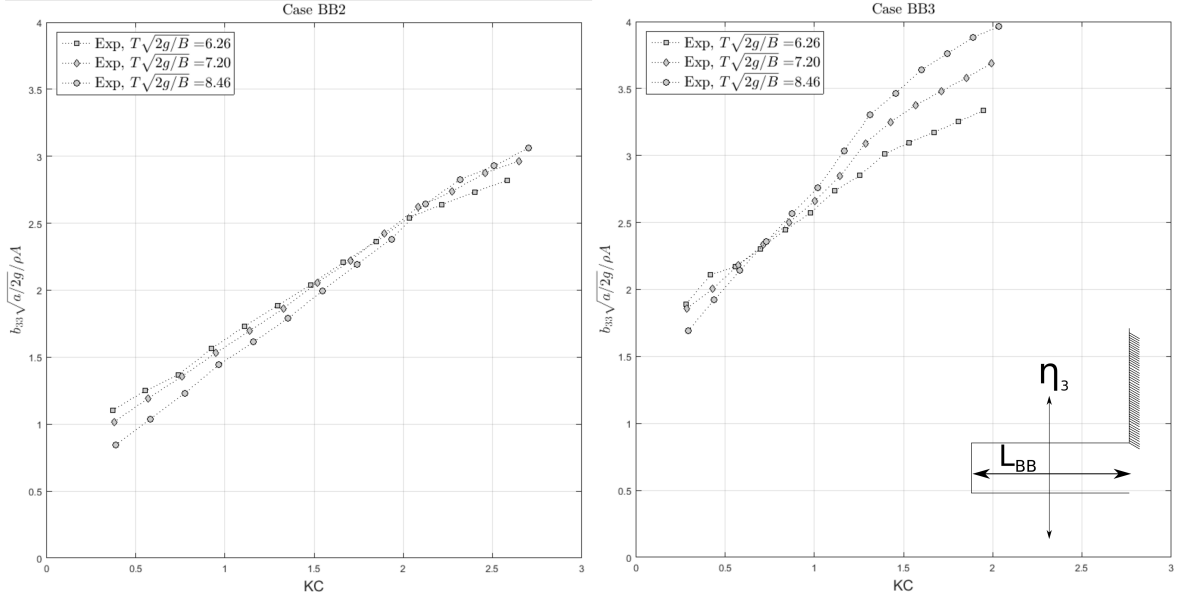
Figure 5.18: Local damping coefficients of bilge-boxes with respect to KC-number and period of oscillations

below shows the nonlinear free-surface condition that generated by the body in one of the model tests. The case shown is for BB3 with $\theta = 10^o$ and $T\sqrt{2g/B} = 6.26$, where from Fig. 5.16 clearly shows PVC2D-Roll over prediction.

From Fig. 5.19 above, there are three physical mechanisms that roughly captured by standard mirrorless camera. No high-speed camera used in this present study, and it is suggested for future study. Firstly, the free-surface is pulled down when the bilge-box goes down. It is similar to what is found in Section 5.13. Secondly, it is suspected that vortex that shed from bilge-boxes are convected away and reach the free-surface as demonstrated in point 4 and 5. Point 6 was taken before the bilge-box starts to go up, the rotating vortex on the free-surface break when interacting with free-surface. Finally, the mixed-water due to the breaking vortex is radiated away as the bilge-box goes up. However, this needs to be confirmed with more detailed study, e.g. Particle Image Velocimetry (PIV) test. Study using Volume of Fluid (VOF) to simulate nonlinear free-surface is also recommended to investigate in the future to validate the hypothesis. But in conclusion, the assumption of linearized free-surface does not model this kind of physics. As discussed in Ommani et al. (2016b), the viscous stresses terms are not modeled in PVC2D-Roll, and may become important when the strong vortex enters the free-surface.

Lastly, the variation of bilge-boxes mean bending moments at bilge-box root are presented for BB2 and BB3 in Fig. 5.20. PVC2D-Roll predicts higher than what measured in model tests for both BB2 and BB3, while gives a good comparison for BB1 case (Fig. 5.14). It is interest to note that by introducing longer bilge-box, if one compare Fig. 5.20 with Fig. 5.14, does not mean that the bending moment would increase. Bending moment is one of the important aspects to consider, i.e. fatigue life.
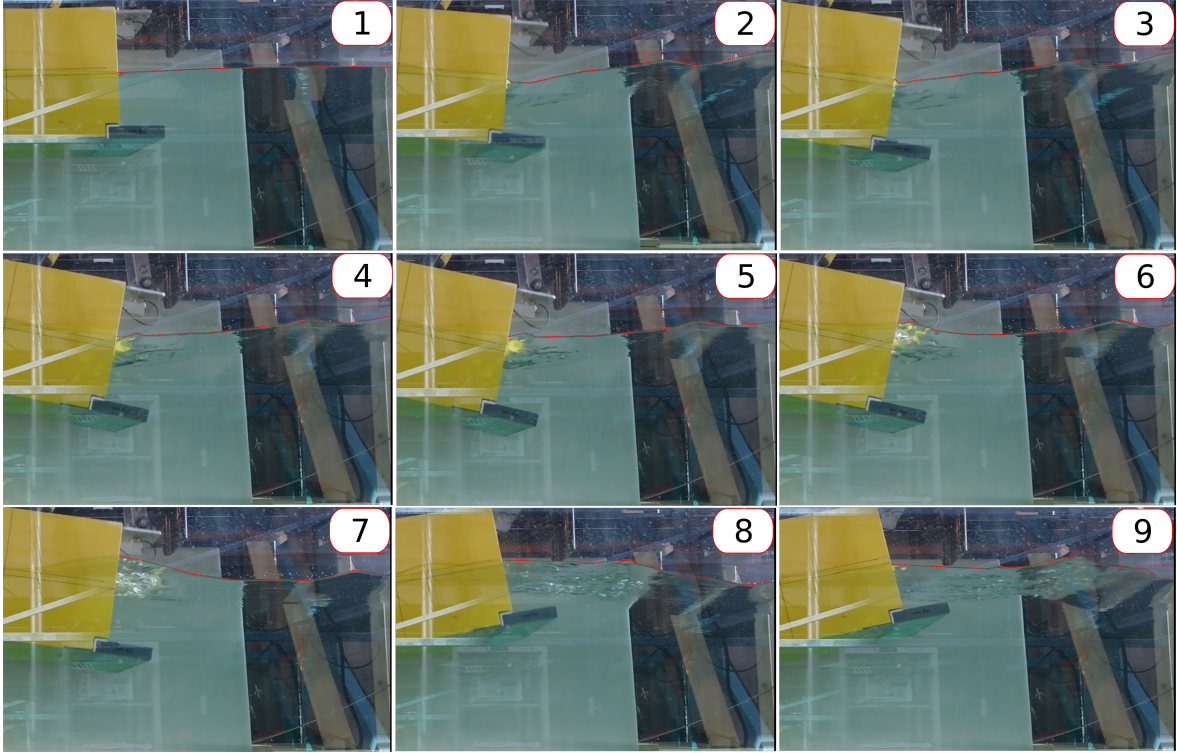
Figure 5.19: Free-surface nonlinearities that found from one of the model tests video documentation. Number shows the the sequence of the motion with bilge-boxes effect to the free-surface

5.4.2 Added-mass coefficients

In addition to the roll damping coefficients, the added-mass has also become one of the important parameters to investigate and will be discussed within this chapter. For sufficiently small bilge box and moderate sea states, the viscous effects on the added-mass can be neglected. Mass of the ship is considered way larger than the added-mass that comes from flow separation at the bilge box tip. This is not necessarily the case in survival seastates and large bilge box, as shown by Shao et al. (2016), where the viscous effects has increased the heave added mass and thus heave natural period.

Since the added-mass extraction in model tests intrinsically difficult due to the uncertainty of I_{44} and C_{44} parameters, where all terms are vanished in damping coefficients extraction, the presented results here are not too trustworthy. The obtained results from model tests demonstrate shifted down results for every increasing period. Investigations has been attempted to find the problem: replication of water test cases in air, sensitivity check of I_{44} and C_{44}, wave reflection in the flume tank and many others, but author did not find the solution due to the time constraint. So is the case for PVC2D-Roll results, as something could not modeled as in reality like the one that found in the previous discussion (see Section 5.4.1). General trend will be discussed based on the findings from both methods. See C and D for more results.

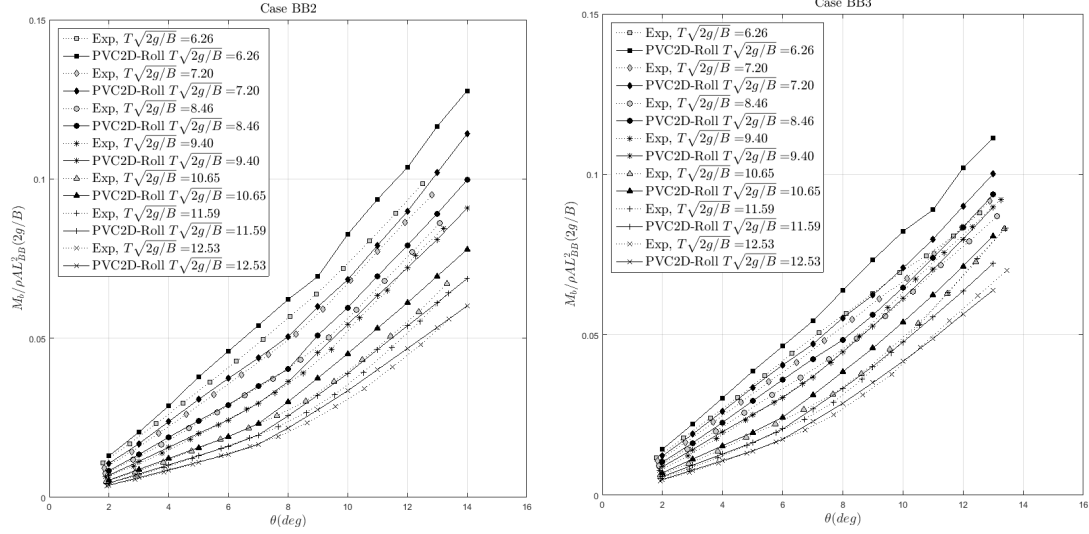Fig. 5.21 represents the added-mass coefficients of the body for all the bilge-boxes length and

Figure 5.20: Variation of mean bending moment at the bilge-box root for BB2 and BB3 case with respect to periods of oscillation for several roll amplitudes

different amplitudes and periods of oscillations. For BB1 case, the added-mass coefficients tend to be constant and independent of amplitude of oscillations. By introducing longer bilge-boxes, the added-mass coefficients decrease with increasing amplitude and the decreasing slope become more pronounce for longer bilge-boxes.

Example of added-mass coefficients dependency on the period is given in Fig. 5.22. Potential flow calculation of two-dimensional conventional ship with beam to draught ratio 2 and 4 are also given just for comparison. The added-mass increases with the presence of bilge-boxes, this clearly shows viscous effects. Larger added-mass relative to the potential flow results is achieved by introducing larger bilge-boxes. For BB1 case, the added-mass shows constant behavior with respect to period increases. This suggests the free-surface has less significant effect for the added-mass of the body with this bilge-boxes length. On the other hand, BB2 and BB3 added-mass shows increment in higher period and indicates the free-surface effects become more pronounce. The added-mass also becomes more dependant on amplitude for BB2 and BB3.

Local added-mass from the bilge-box can be extracted by using the bilge-box force measurement. The bilge-box is assumed to oscillate in heave locally. The results presented in here are non-dimensionalized by the added-mass of the heaving flat plate with similar length as bilge-box in infinite fluid ($a_{44} = \rho\pi(L_{BB}/2)^2$). The results are shown in Fig. below. In general, the added-mass coefficients for all bilge-boxes are bigger than the flat plate in infinite fluid case. This mainly due to the so-called wall effect that introduced by the presence of the body. The hull obstructs more fluid, so the bilge-box accelerates more water thus higher added-mass. The wall effect becomes less pronounce in longer bilge-box, which relatively speaking, the presence of the hull is less perceived by the bilge-box. The added-mass of the bilge-boxes decrease drastically in some KC-number and period of oscillations as shown in
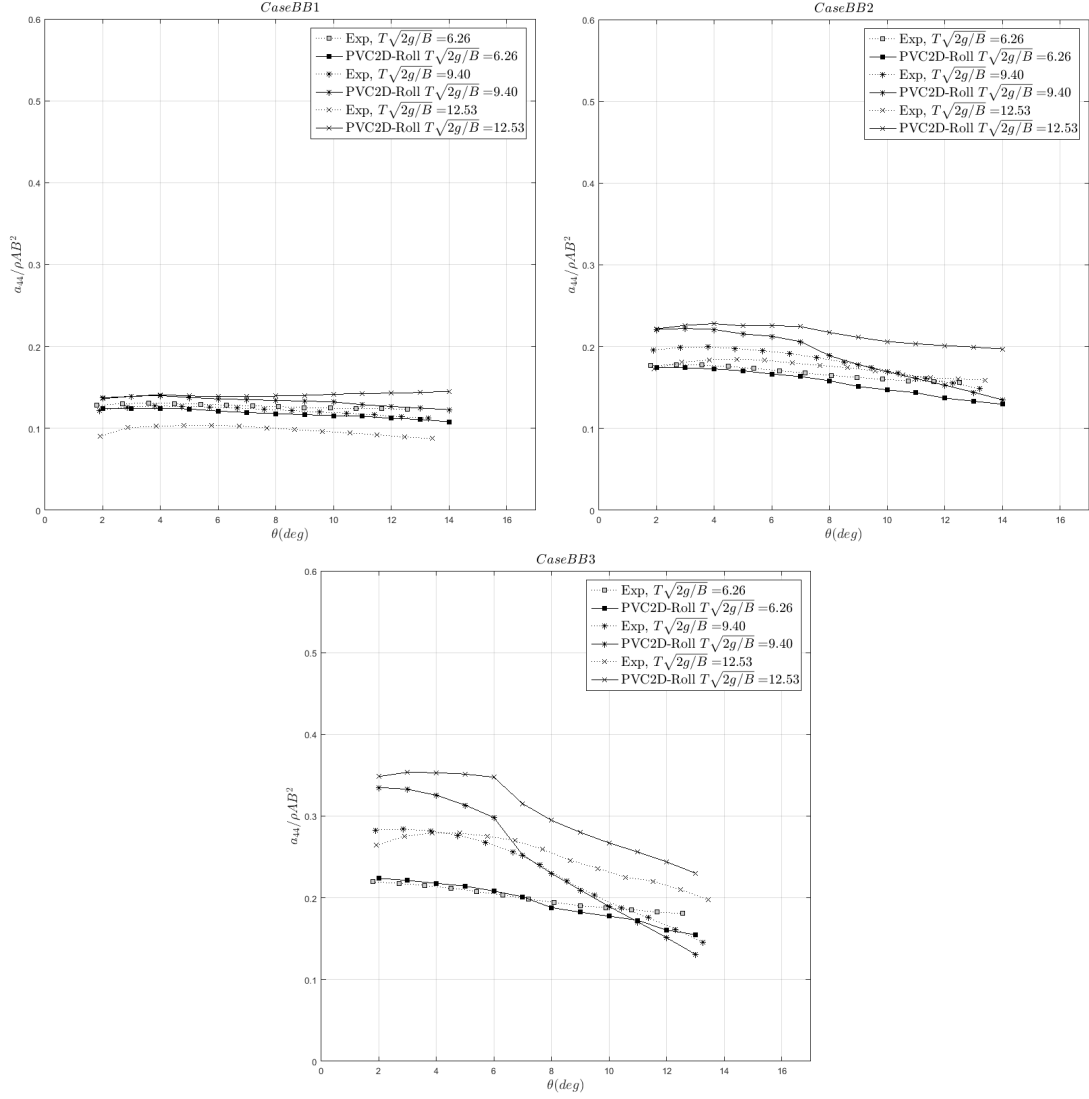
Figure 5.21: Roll added-mass coefficients variation with respect to several amplitudes, period of oscillations and bilge-box length

Fig. 5.23, especially for BB2 and become more pronounce in BB3. On the contrary, the BB1 shows the increment of added-mass. This may also explain the added-mass changes found in Fig. 5.21.

Some unphysical jump is found in PVC2D-Roll results, as one may observe from Fig. 5.23. One of the candidates is that the numerics are not converged. More refined mesh is suggested for the further study. Dedicated time step convergence test also considered to be important, since the deforming mesh technique requires small Courant number in order to achieve stable solution. Mesh refinement has been attempted once, from R6 to R7 (see Table 3.2). Results improvement was achieved, but still with the unphysical jump. Another improvement has not accomplished due to time constraint.

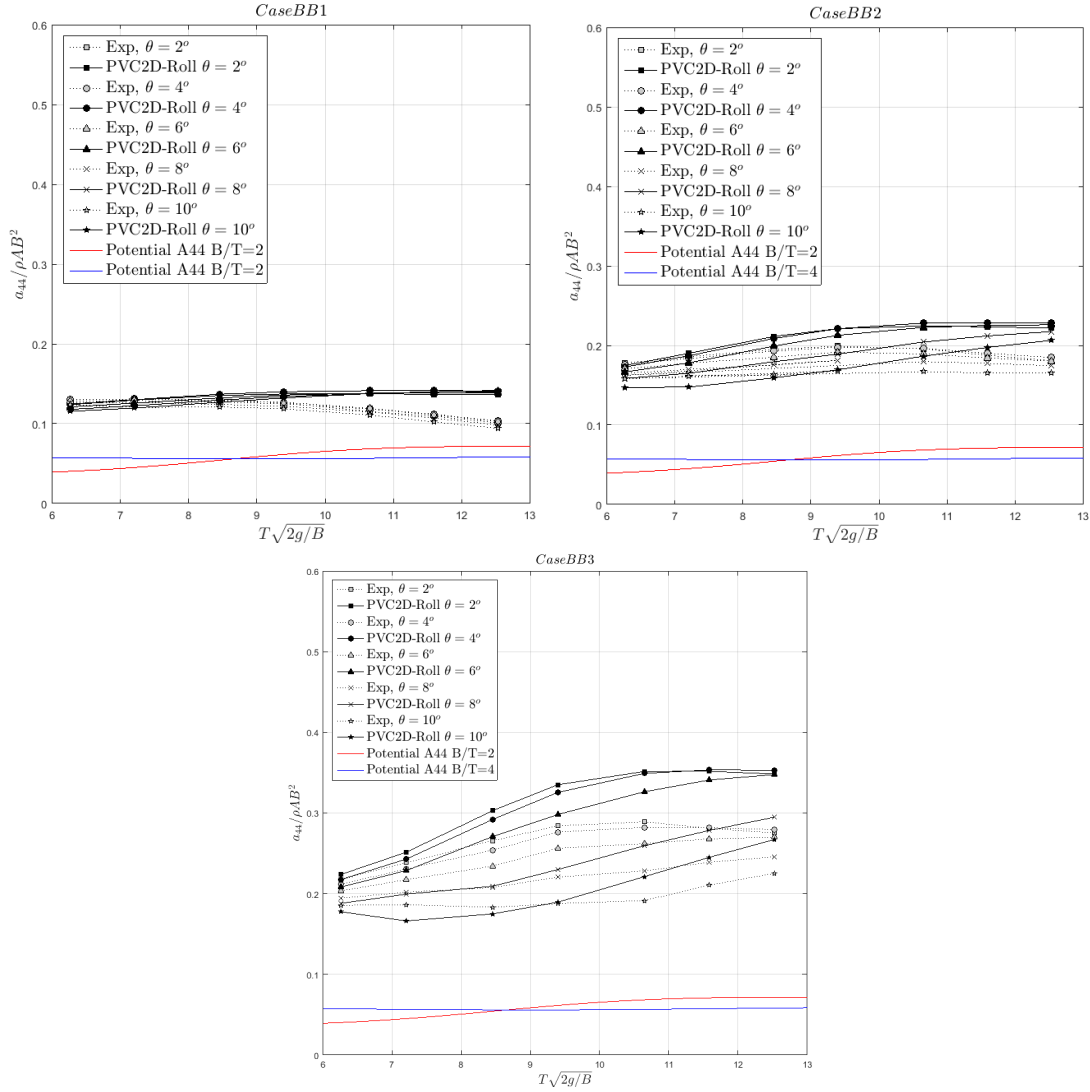In conclusion, this section shows the importance of considering the viscous added-mass pa-

Figure 5.22: Added-mass coefficients dependency on the period of oscillations

rameter in ship with bilge-boxes. The magnitude changes with different amplitudes, period of oscillations and length of the bilge-boxes. Considering only the linear added-mass coefficient during the phase design, can lead to wrong prediction of structural natural period which is a very important parameter.
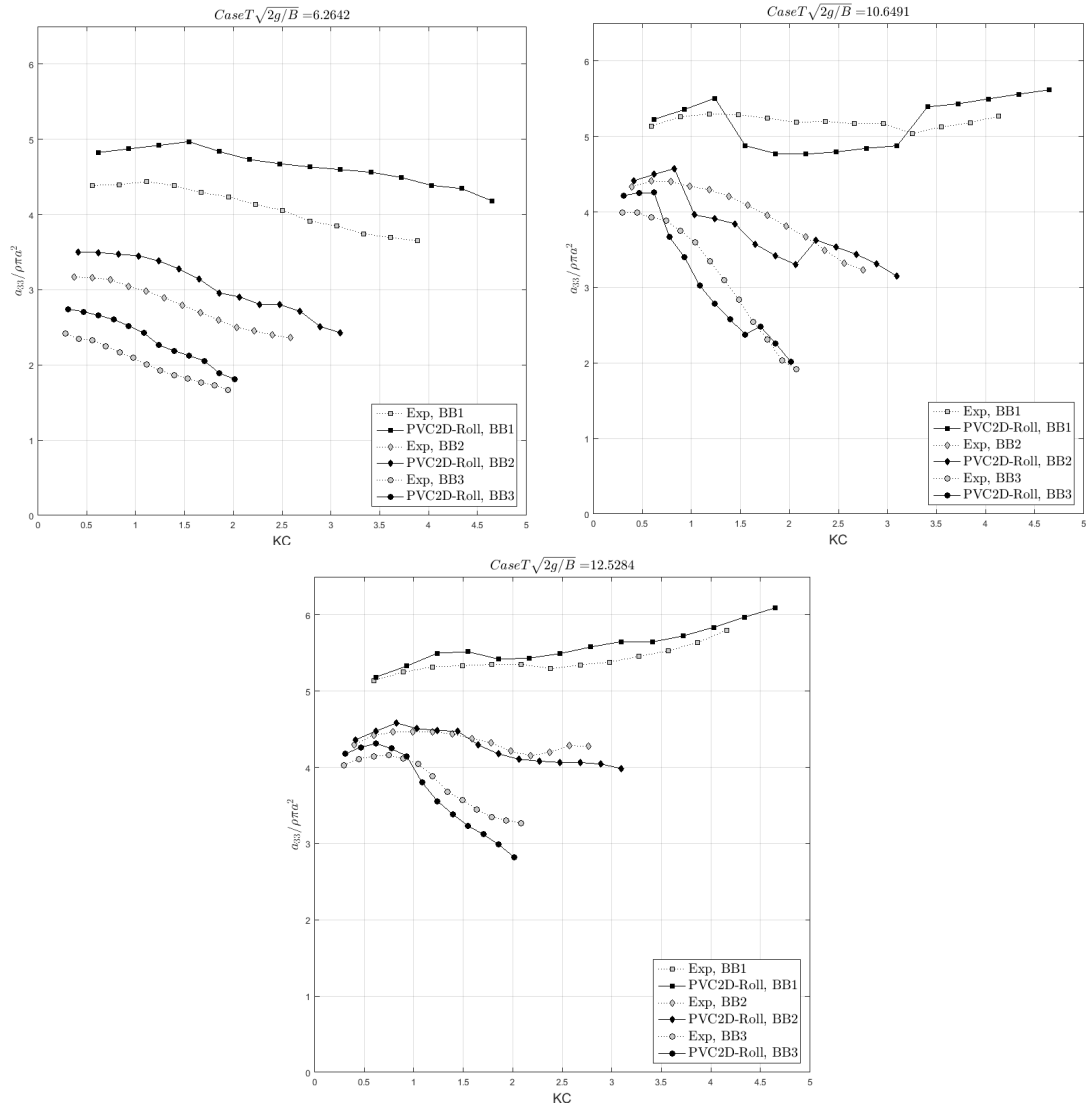
Figure 5.23: Heave added-mass coefficients for several bilge-box length

Chapter 6

Conclusions and Further Work

6.1 Conclusions

The prediction of viscous roll damping is difficult due to the flow separation from the bilge keels and/or hull, which has dependency on several aspects: hull geometry, bilge radius, free surface effect, bilge keels length and/or position, etc. In addition, the added-mass from the flow separation around the bilge-boxes can become significant relative to structural total weight and thus alter the resonance frequency. Dedicated parameter study needs to be performed in order to solve the roll motion problem as a whole.

The main objective of present study is to investigate the viscous roll damping and added-mass in the harmonically rotating two-dimensional ship section with different length of bilge boxes both numerically and experimentally. The section was forced to rotate around fixed point with one draft condition, 13 amplitudes, 7 periods of oscillations and 3 bilge-boxes length. Forced-roll tests were performed with the representation of two-dimensional cross section in narrow flume tank Ladertanken, Norwegian University of Science and Technology.

PVC2D-Roll solver based on Finite Volume Method is adopted for solving laminar incompressible flow. The linearized free-surface condition is assumed, hence the nonlinear terms are neglected. This reduce the needs of fine mesh in the vicinity of free-surface, hence the mesh only required to be fine only around the bilge-boxes. Total cells used in the present study are around $N \approx 2 \times 10^4$. Body-boundary condition is required to be exact, which believed to dictate the strength of separated flow.

The obtained damping coefficients from both methods are relatively in a good agreement. For the short bilge-boxes (BB1), PVC2D-Roll captures the quadratic damping with respect to increasing amplitude very well and starts to over predict the results for higher amplitudes. Slope changes were observed in the damping coefficients with respect to amplitude curves for longer bilge-boxes (BB2 and BB3) and believed due to the free surface contribution in flow separation at the bilge-boxes tip. The observation in bilge-boxes forces measurement was attempted, the results suggest that free-surface effect causes damping coefficients strongly

dependent on the amplitude and period. The discrepancies shown by PVC2D-Roll results are believed due to the nonlinear free surface condition, some strong vortex were documented reach the free surface in one of the model tests cases.

In general, added-mass in roll increases with the presence of bilge-boxes, as evidenced by comparison with the potential calculation for conventional ship hull with beam to draft ratio equal to 2 and 4. Added-mass coefficients for the short bilge-boxes tend to show independency from oscillation amplitude and period. On the other hand, longer bilge-boxes results exhibit reduced added-mass coefficients with respect to amplitude, while increases with increasing period. This is believed mainly due to the viscous flow separation and free surface effect. Bilge-boxes added-mass coefficients also compared with the theorical added-mass of flat plate in infinite fluid, and the results suggest that wall effect from the body thus higher added-mass. Added-mass coefficients are more significant in shorter bilge-boxes as the wall effect is more prominent. The added-mass extraction in model tests is intrinsically difficult due to the uncertainties that might introduced by I_{44} and C_{44} terms, wave reflection, etc. Careful investigation to verify the extracted added-mass quality has not achieved due to the time limit.

6.2 Further work

In the end of present study, there are several details that in author's opinion would have been beneficial to continue in the future investigation of the two-dimensional ship section with bilge-boxes.

Forced-roll oscillations of fully submerged body from present study would be beneficial to understand the flow separation mechanism without any disturbances from free surface. Tao and Thiagarajan (2003) investigated the heave case for damping plate with thickness in small KC number, and they pointed out three different vortex shedding regimes. Based on author's knowledge, no one has done for the roll motion. The knowledge of vortex shedding definitely will add more insight to what have been investigated in the present study. This can be done numerically and/or experimentally.

The freely-floating experiment of identical model in regular and/or irregular waves is another candidate. In the present study, the calm water was assumed. The damping and added-mass contribution from wave particle speed at the bilge keel tip need to be investigated by comparing with present investigation.

The dedicated study on mesh and time step convergence tests in PVC2D-Roll is important and need to be done in the future. Due to the limited time, PVC2D-Roll has been simulated without thorough dedicated investigation and sensitivity check. Consequently, some unphsical jump appeared in the results, i.e. wave probes, the bilge-boxes forces, etc.

Another possibility is to use another numerical solver to compare with present numerical

calculation. Nonlinear free surface is also believed to be important for the present study, hence CFD simulation using surface capturing method such as VOF would be interesting.

Appendix A

Information of the Attached Electronic Appendix

A.1 Experiment MATLAB scripts

Table A.1: Description of the MATLAB scripts used for the experiment data

Matlab function / script	Description
acc2pos.m	script for calculation of displacement when accelerations are known time series.
acc2vel.m	script for calculation of velocity when accelerations are known time series.
bpass.m	function that will band pass filter time series in matrix x
catman_read_5r8	function to read the acquired data from amplifier systems MGCplus
FindAngVel.m	function to find rotational angle based on two vertical accelerometer
mukCut.m	function to cut time series into the specific time span
mukFFT.m	function to do FFT to the signal and visualize the results
mukZuC.m	function to identify the signal based on zero up crossing method
ststate.m	function to find the steady state part in the measured signal
write2mcl.m	read the binary format
PostProcessing.m	main script of postprocessing data in the forced-roll experiment

A.2 CFD MATLAB scripts

Table A.2: Description of the MATLAB scripts used for the CFD data

Matlab function / script	Description
generateRun.m	function to generate PVC2D-Roll case folder for some specific parameter
runscript.m	execute generateRun.m
forceimport.m	function to import the bilge boxes force output from PVC2D-Roll
rollmomimport.m	function to import the roll moment output from PVC2D-Roll
importfile2.m	function to import the the right wave probe output from PVC2D-Roll
importfile3.m	function to import the the left wave probe output from PVC2D-Roll
importfile3.m	function to do FFT to the signal and visualize the results
CFDDatabase.m	main function to generate structure file for PVC2D-Roll results database

A.3 Post-processing MATLAB scripts

Table A.3: Description of the MATLAB scripts used for the post-processing data

Matlab function / script	Description
BBFCurve.m	function to plot the bilge-boxes force damping/added-mass graphs
BBForC.m	function to plot the bilge-boxes forces time series
bbforce.m	function to calculate the hydrodynamic coefficients of bilge-boxes
ExtSS.m	function to create steady state data structure file
HydCoeff.m	function to calculate the hydrodynamic coefficients of model
HydCurve.m	function to plot the model damping/added-mass graphs
MainPostproc.m	main script that shows all the relevant function for the post-processing
MotForC.m	function to plot motion and force time series
StudentT.m	function to calculate the uncertainty analysis from experiment

Appendix B

Damping Coefficients Results
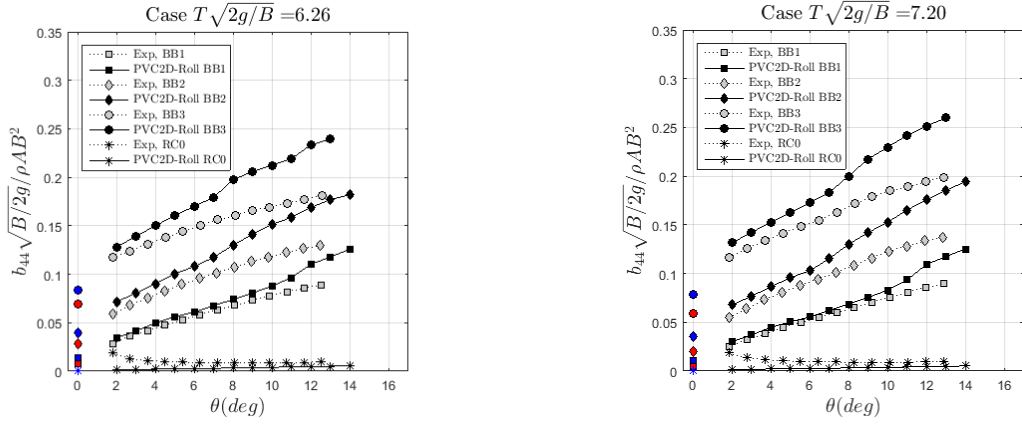
Figure B.1: Damping coefficients results for the varying bilge-boxes length case $T\sqrt{2g/B}$=6.26 and 7.20
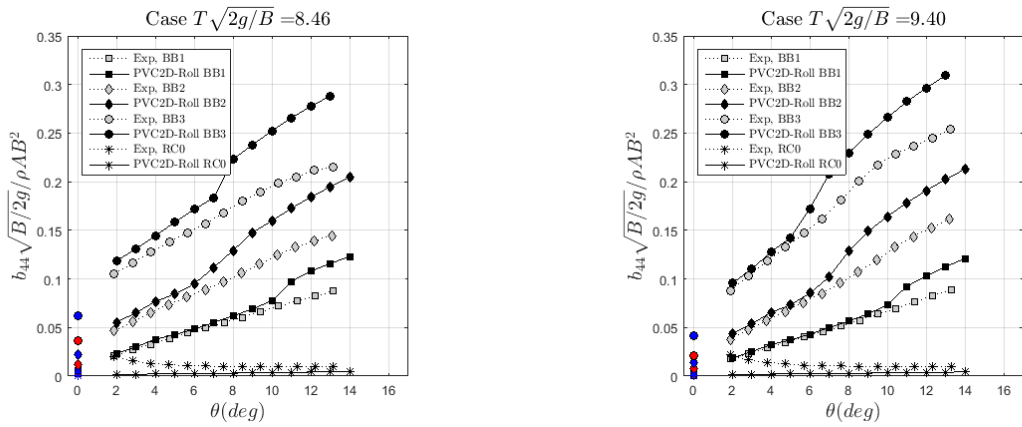
Figure B.2: Damping coefficients results for the varying bilge-boxes length case $T\sqrt{2g/B}$=8.46 and 9.40
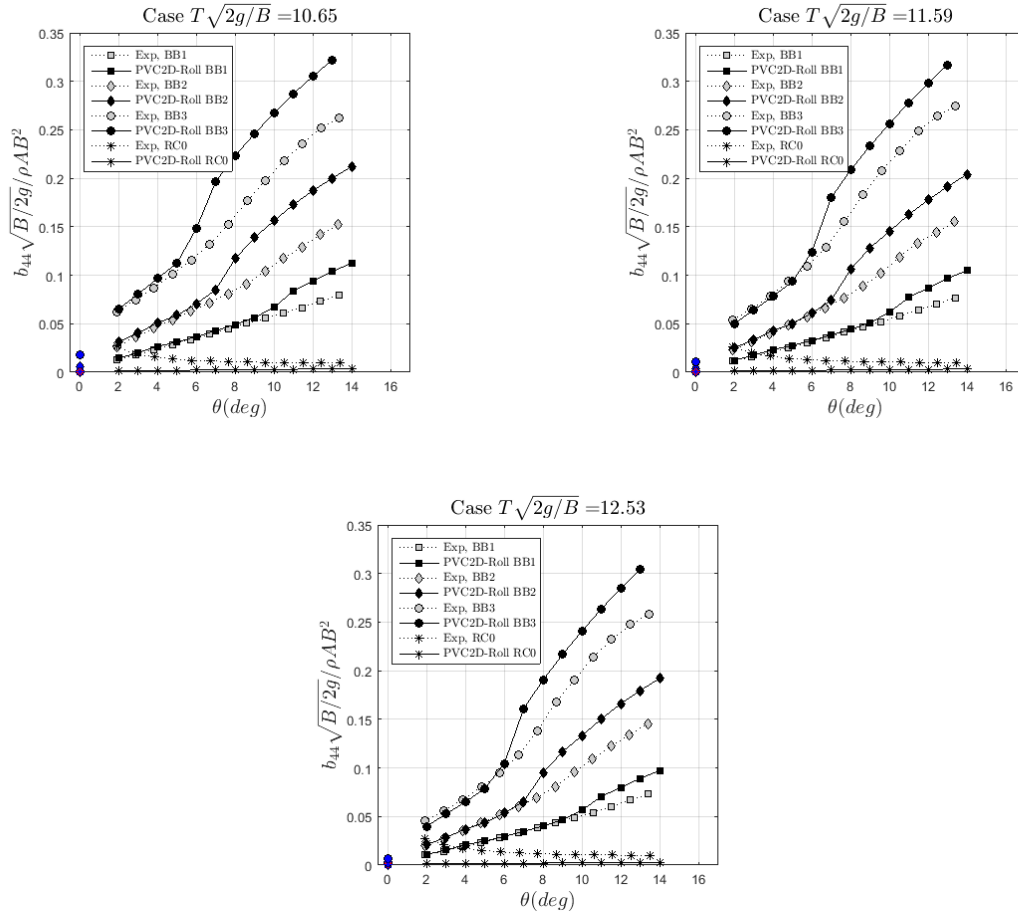
Figure B.3: Damping coefficients results for the varying bilge-boxes length case $T\sqrt{2g/B}$=10.65, 11.59 and 12.53
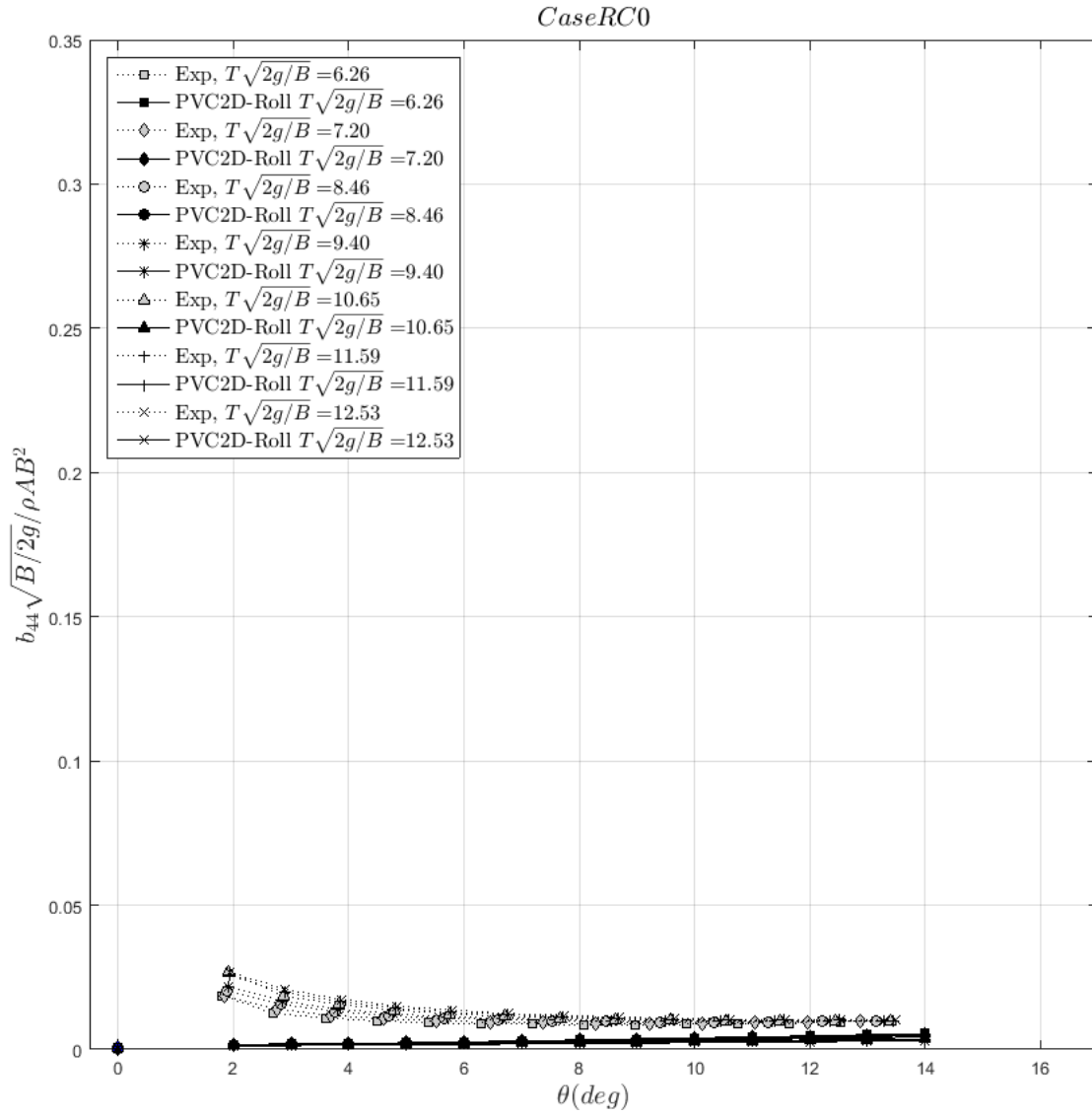
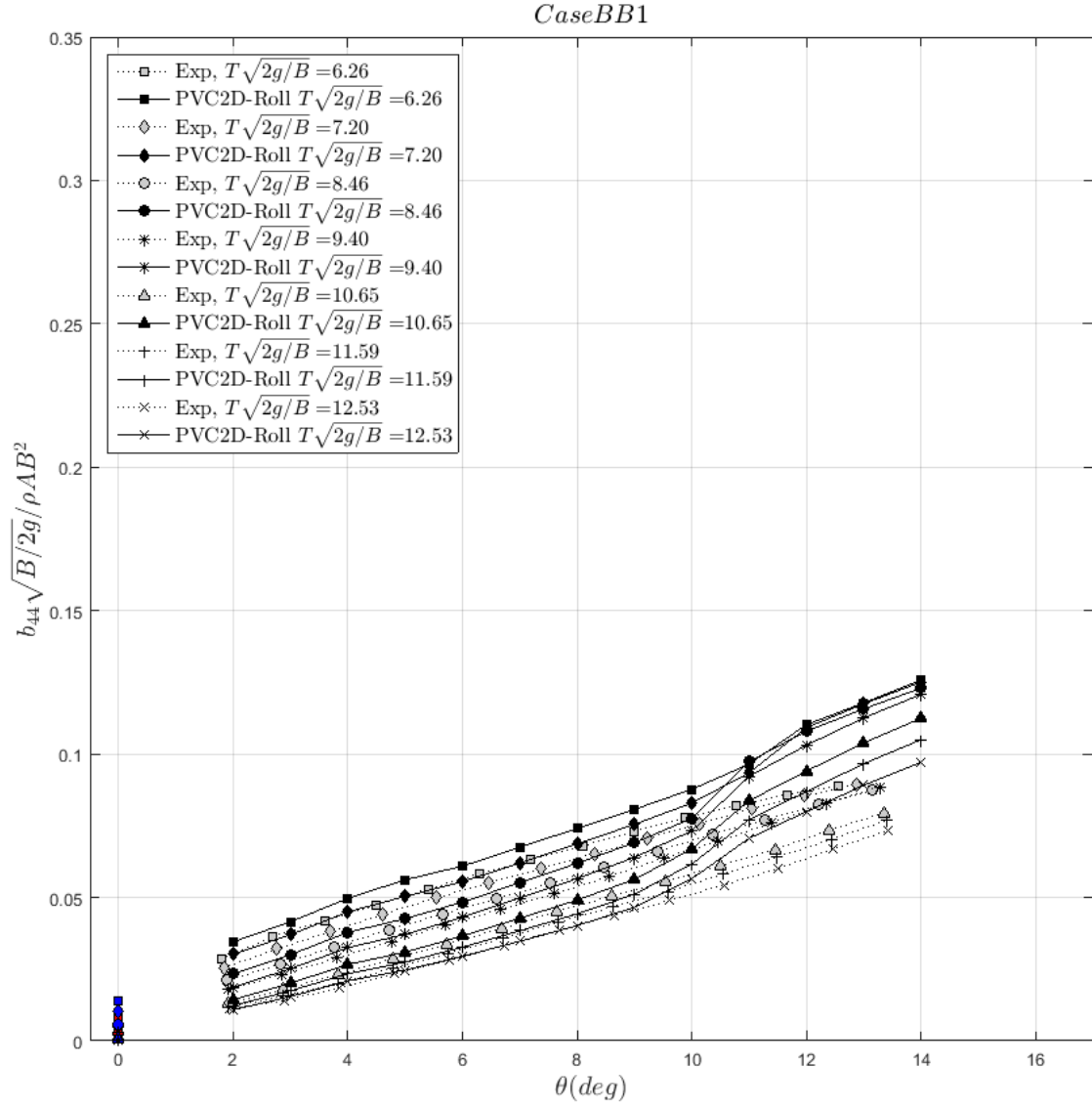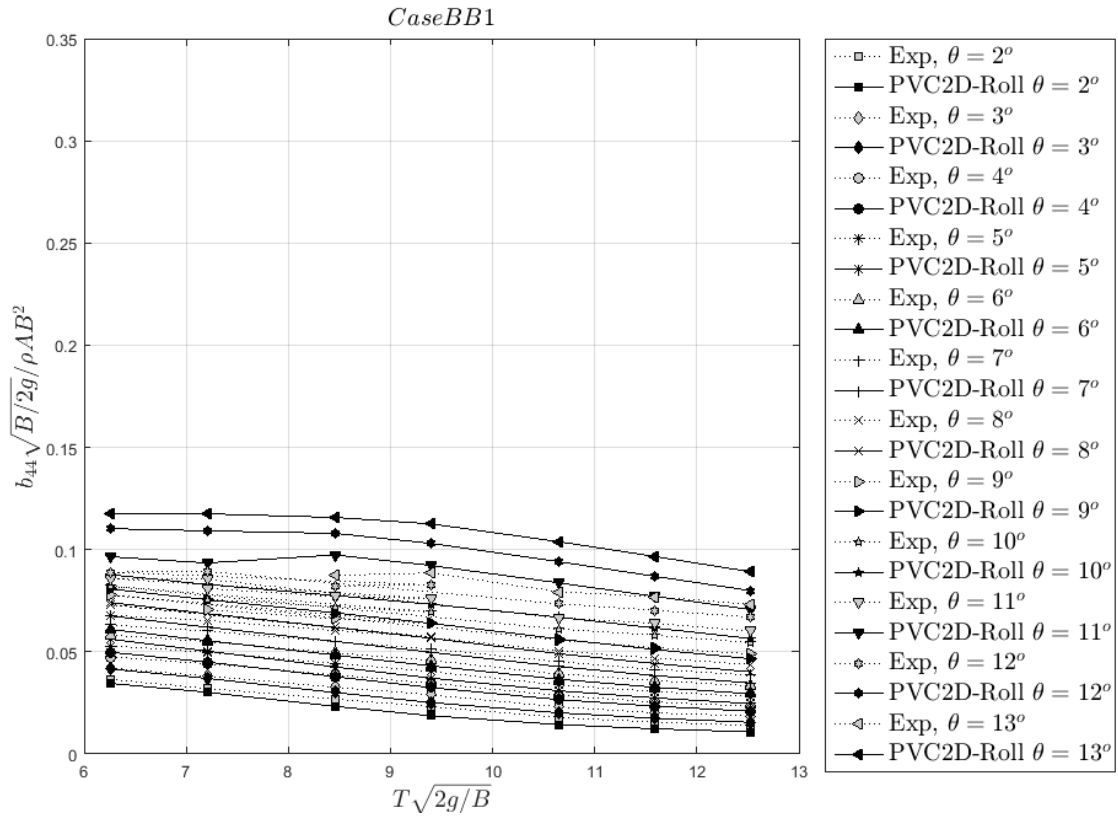Figure B.4: Damping coefficients results for RC0 case with respect to amplitude increases

Figure B.5: Damping coefficients results for BB1 case with respect to amplitude increases
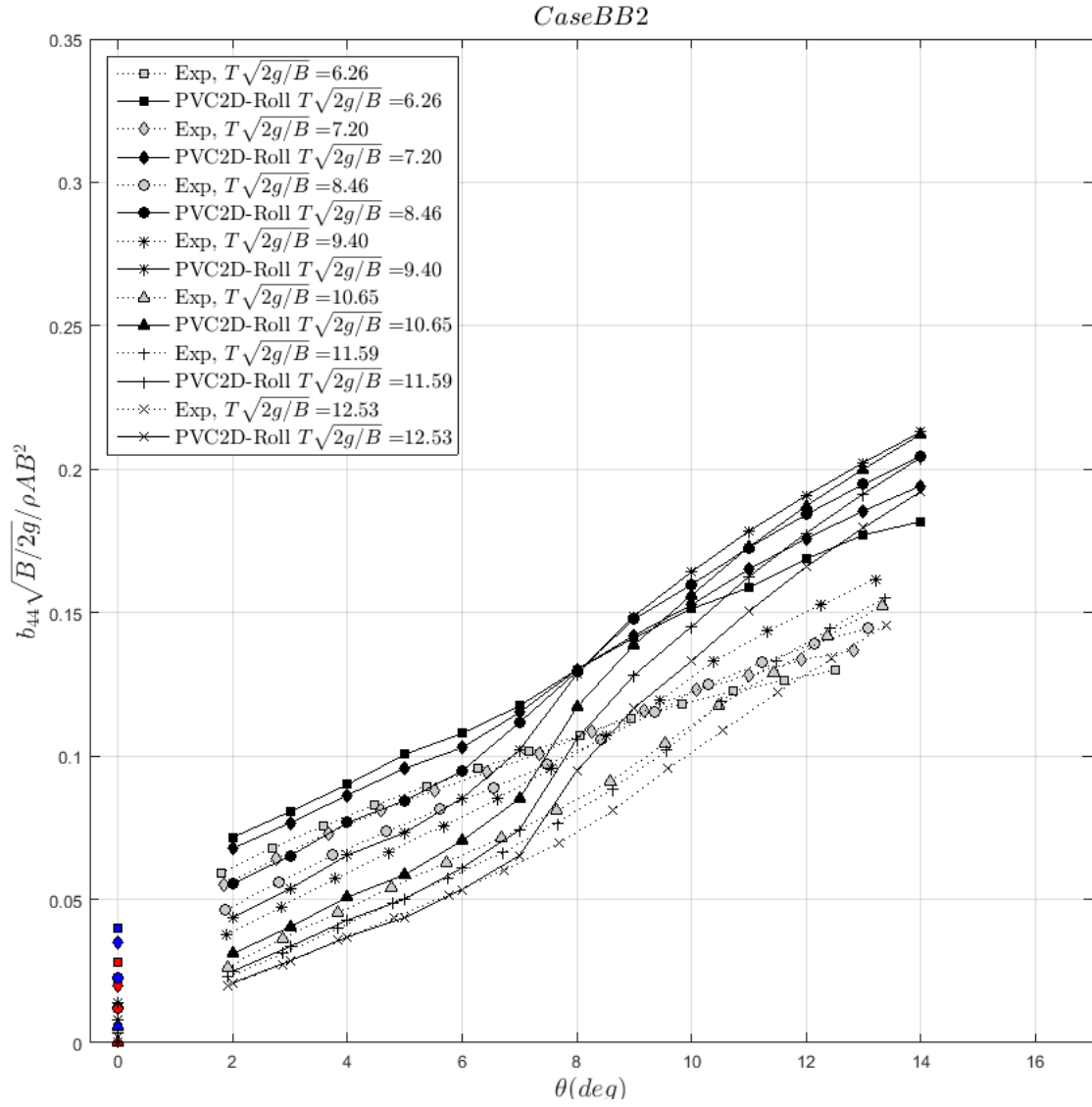
Figure B.6: Damping coefficients results for BB2 case with respect to amplitude increases
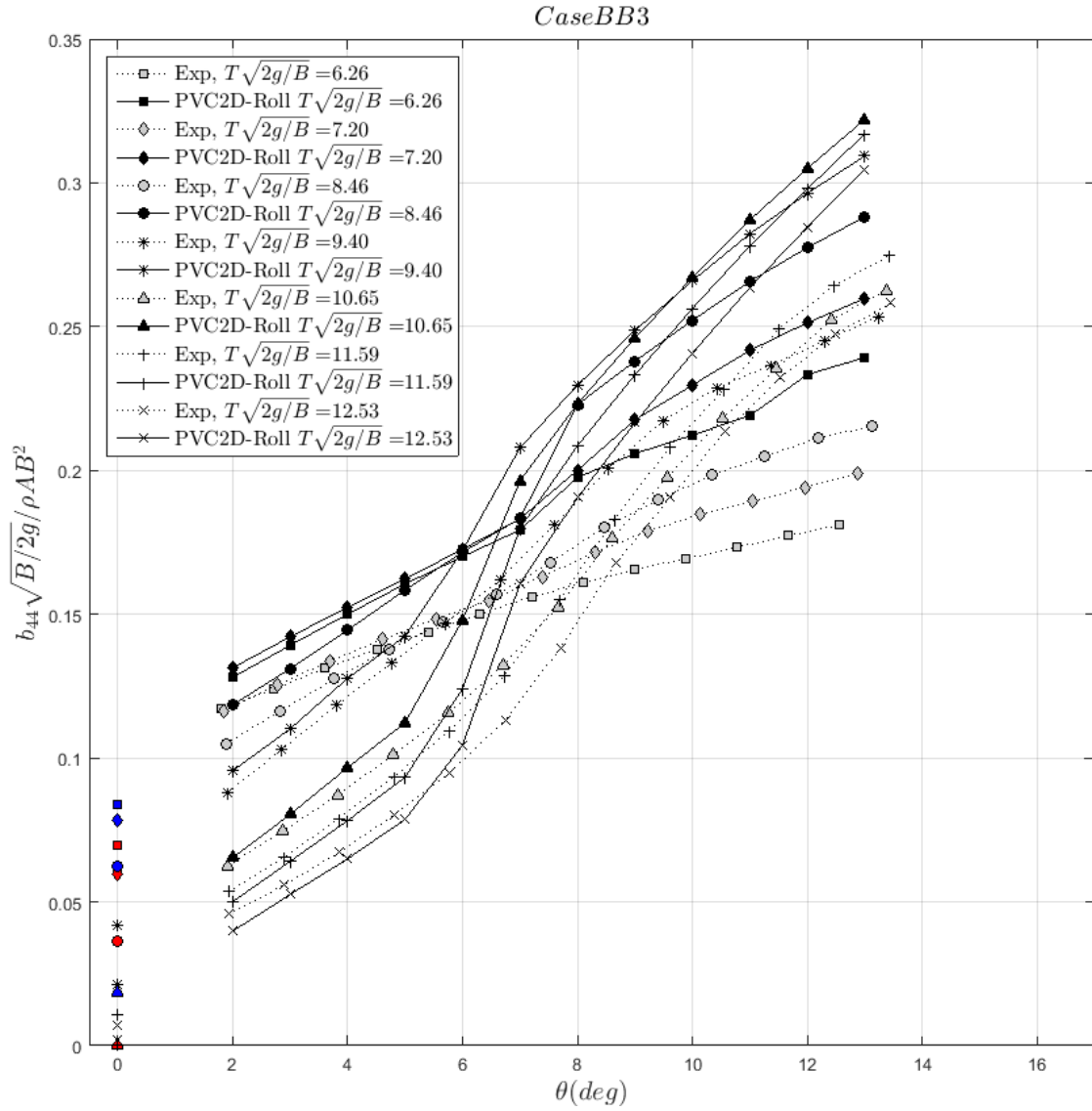
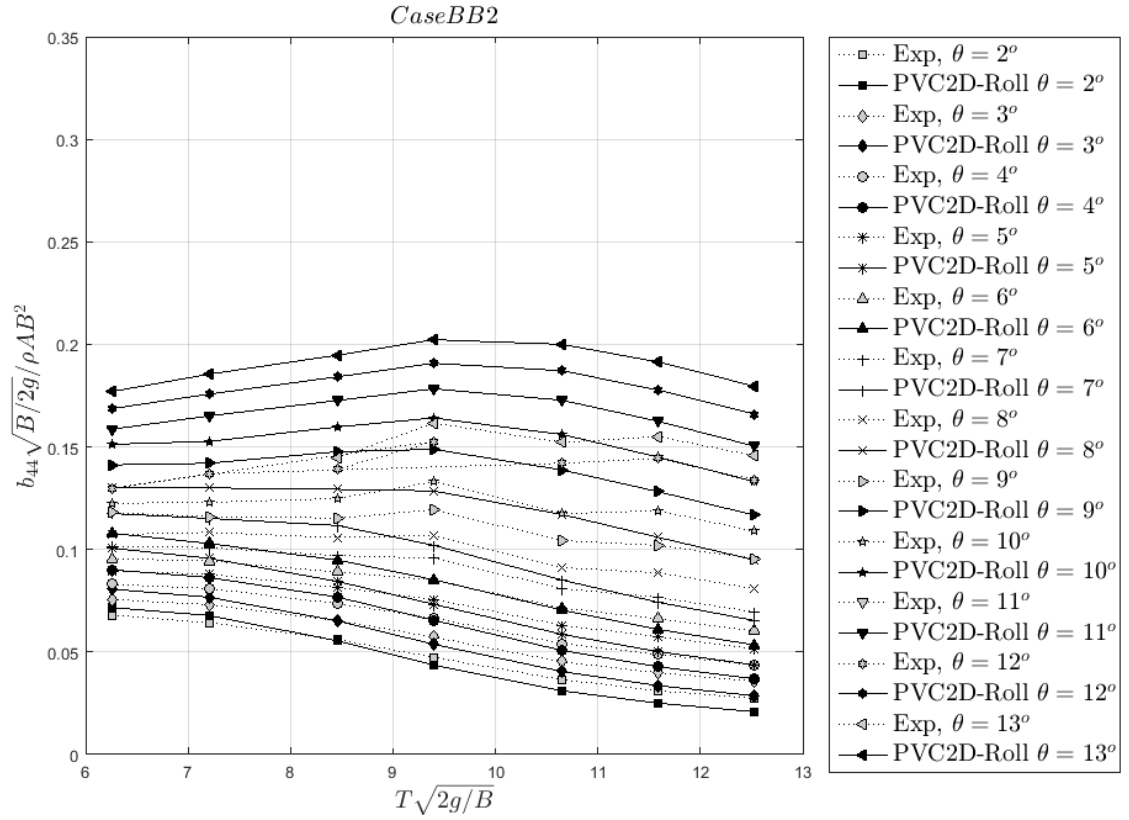Figure B.7: Damping coefficients results for BB3 case with respect to amplitude increases
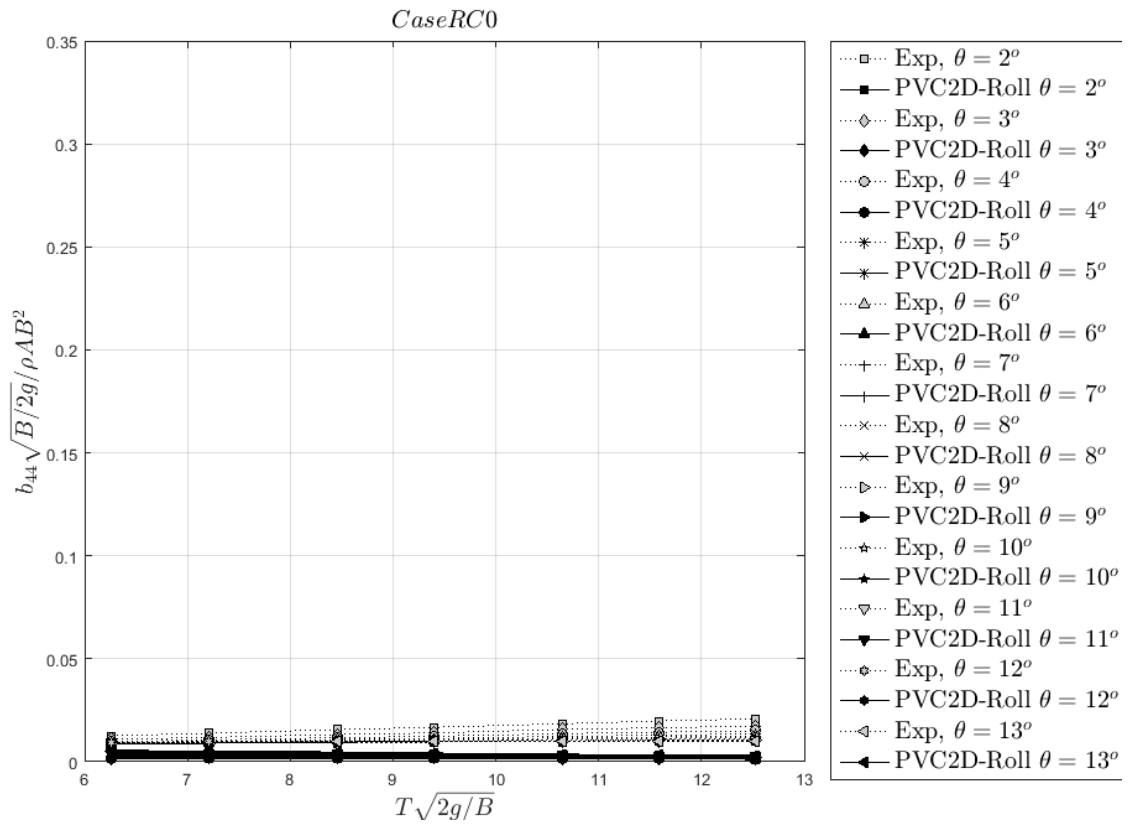
Figure B.8: Damping coefficients results for RC0 case with respect to period of oscillations increases

Figure B.9: Damping coefficients results for BB1 case with respect to period of oscillations increases

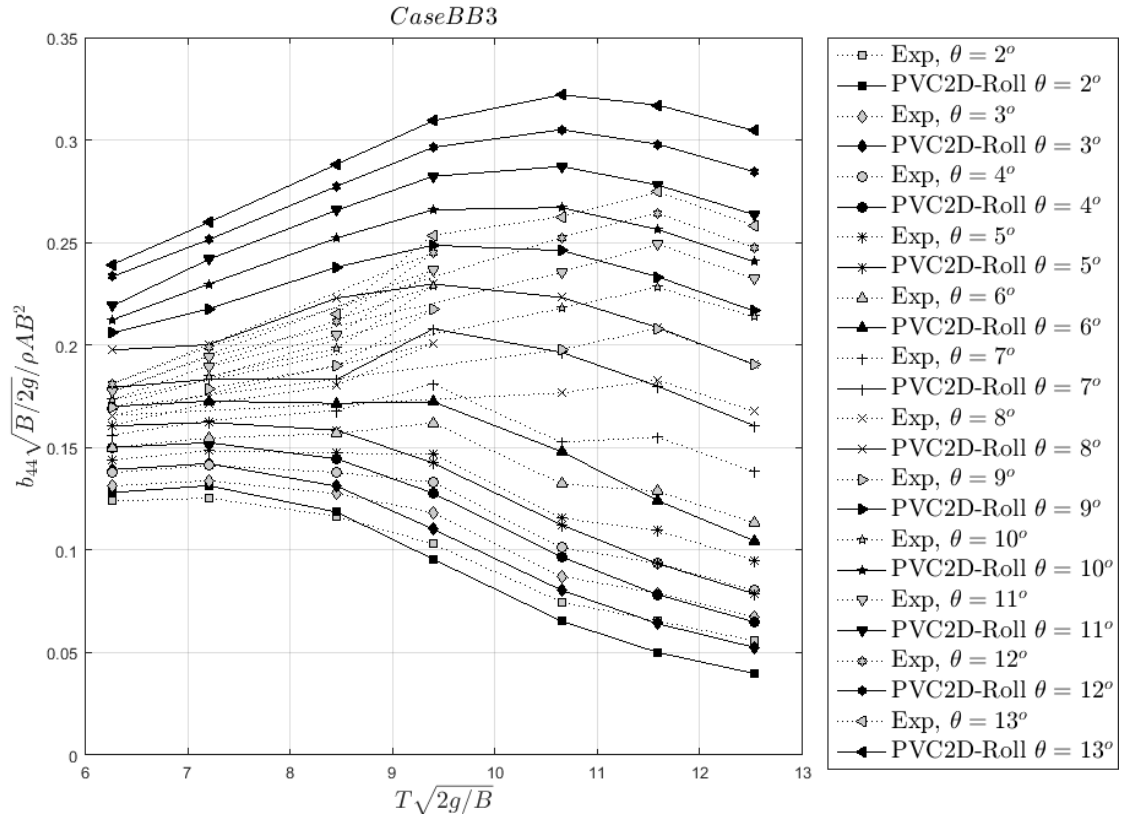Figure B.10: Damping coefficients results for BB2 case with respect to period of oscillations increases

Figure B.11: Damping coefficients results for BB3 case with respect to period of oscillations increases

Appendix C
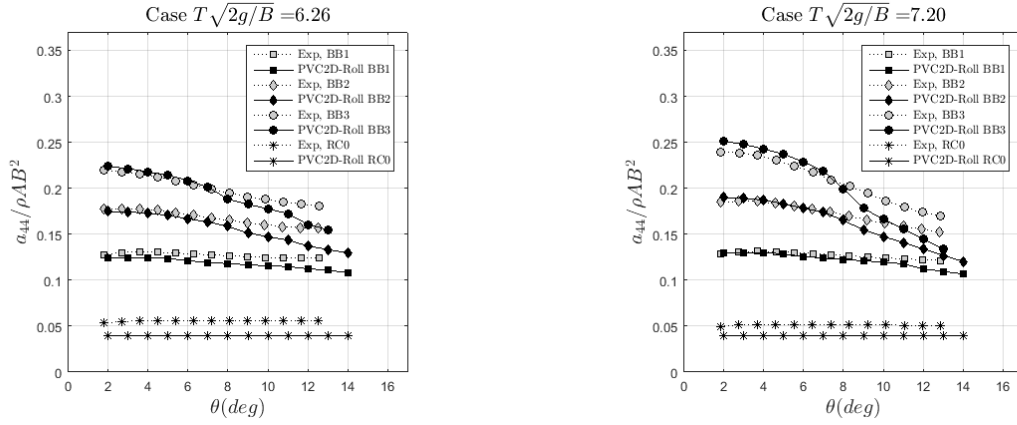
Added-Mass Coefficients Results

Figure C.1: Added-mass coefficients results for the varying bilge-boxes length case $T\sqrt{2g/B}$=6.26 and 7.20
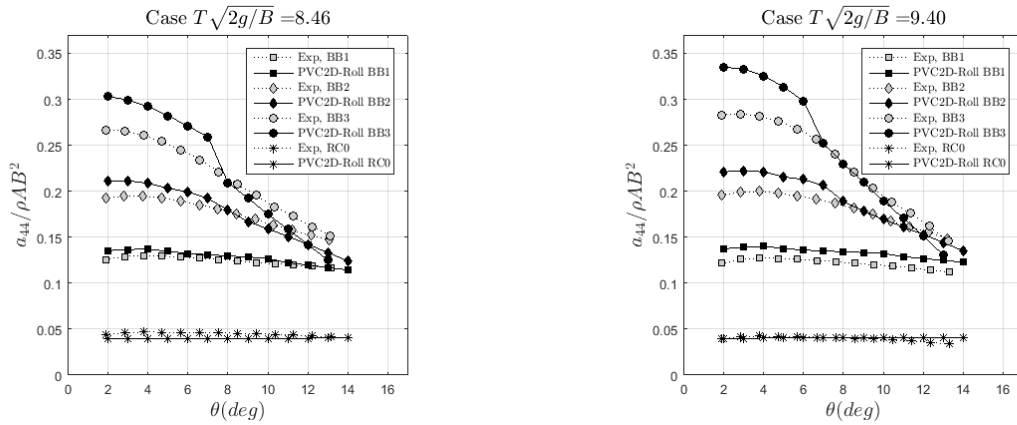

Figure C.2: Added-mass coefficients results for the varying bilge-boxes length case $T\sqrt{2g/B}$=8.46 and 9.40
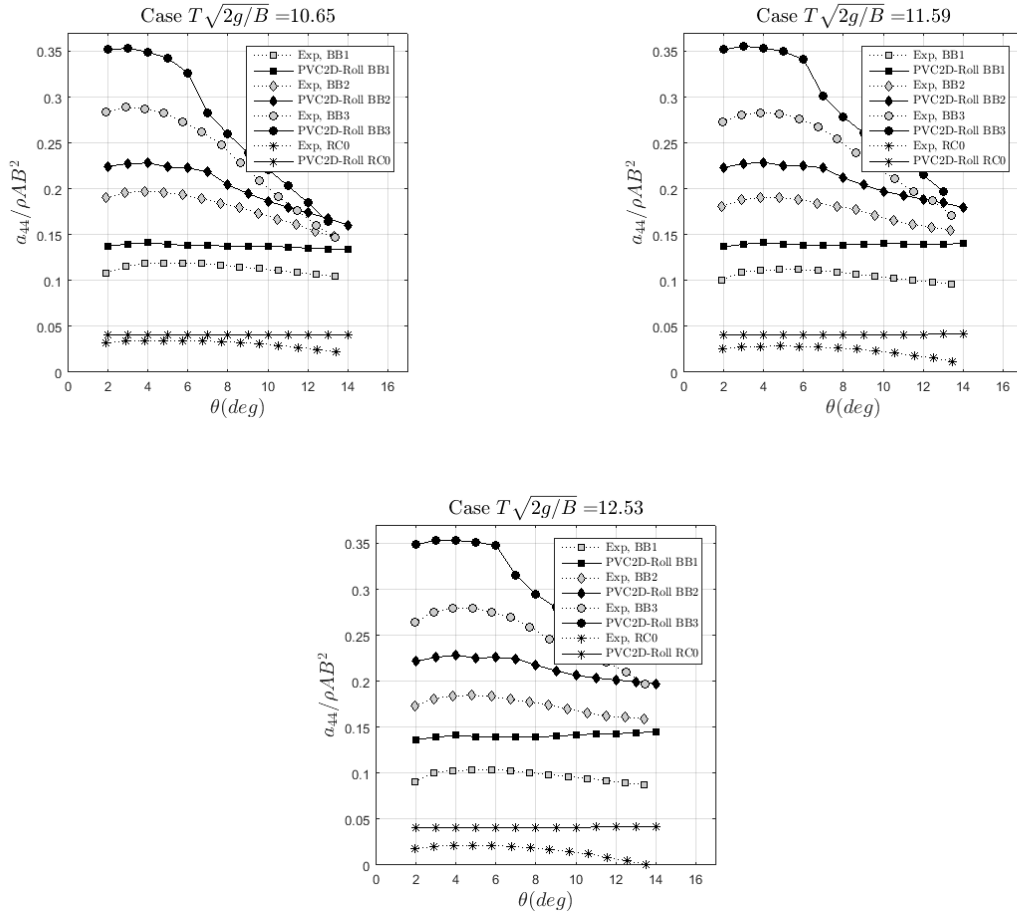
Figure C.3: Experiment results for the varying bilge-boxes length case $T\sqrt{2g/B}$=10.65, 11.59 and 12.53
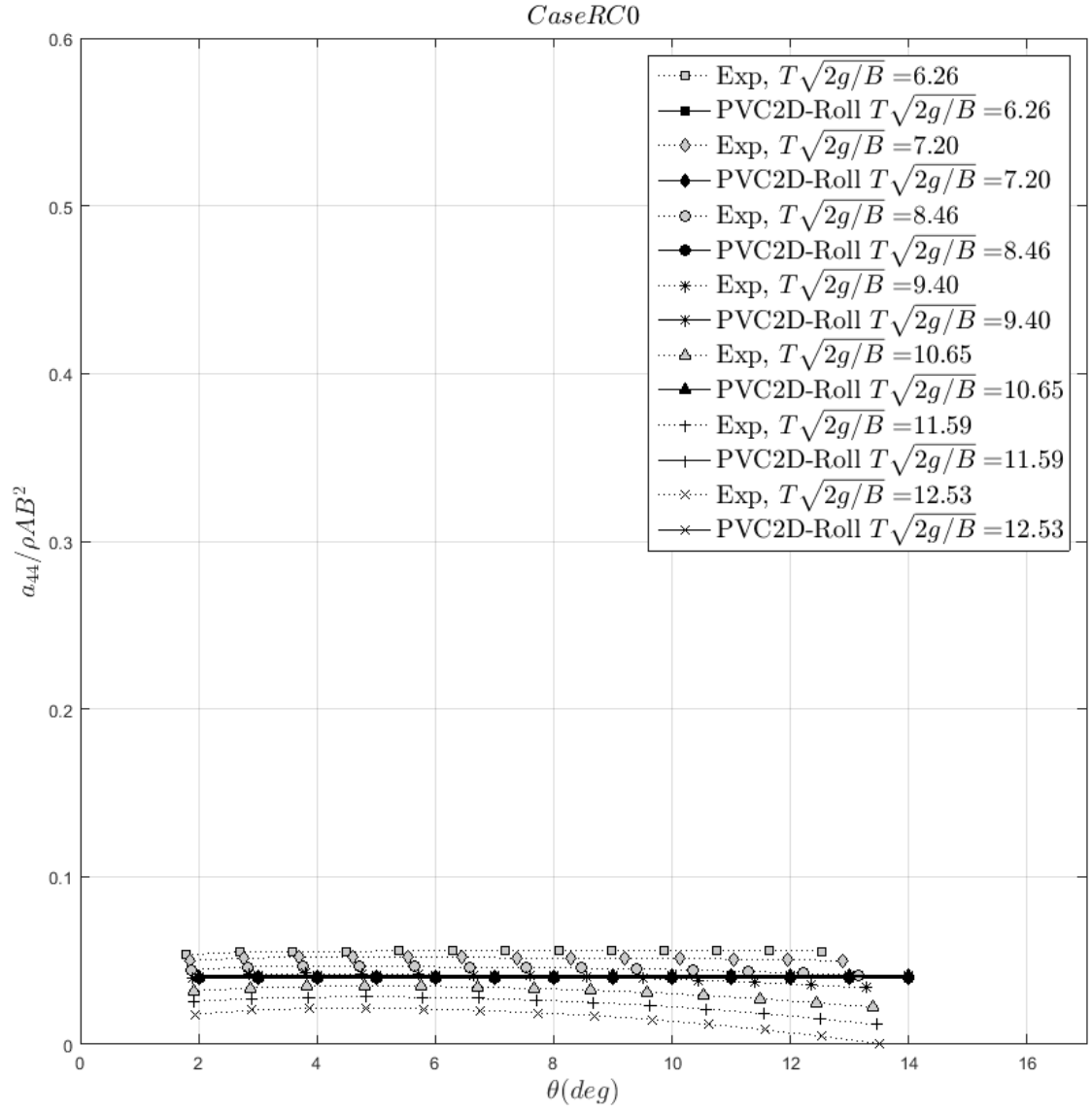
Figure C.4: Added-mass coefficients results for RC0 case with respect to amplitude increases
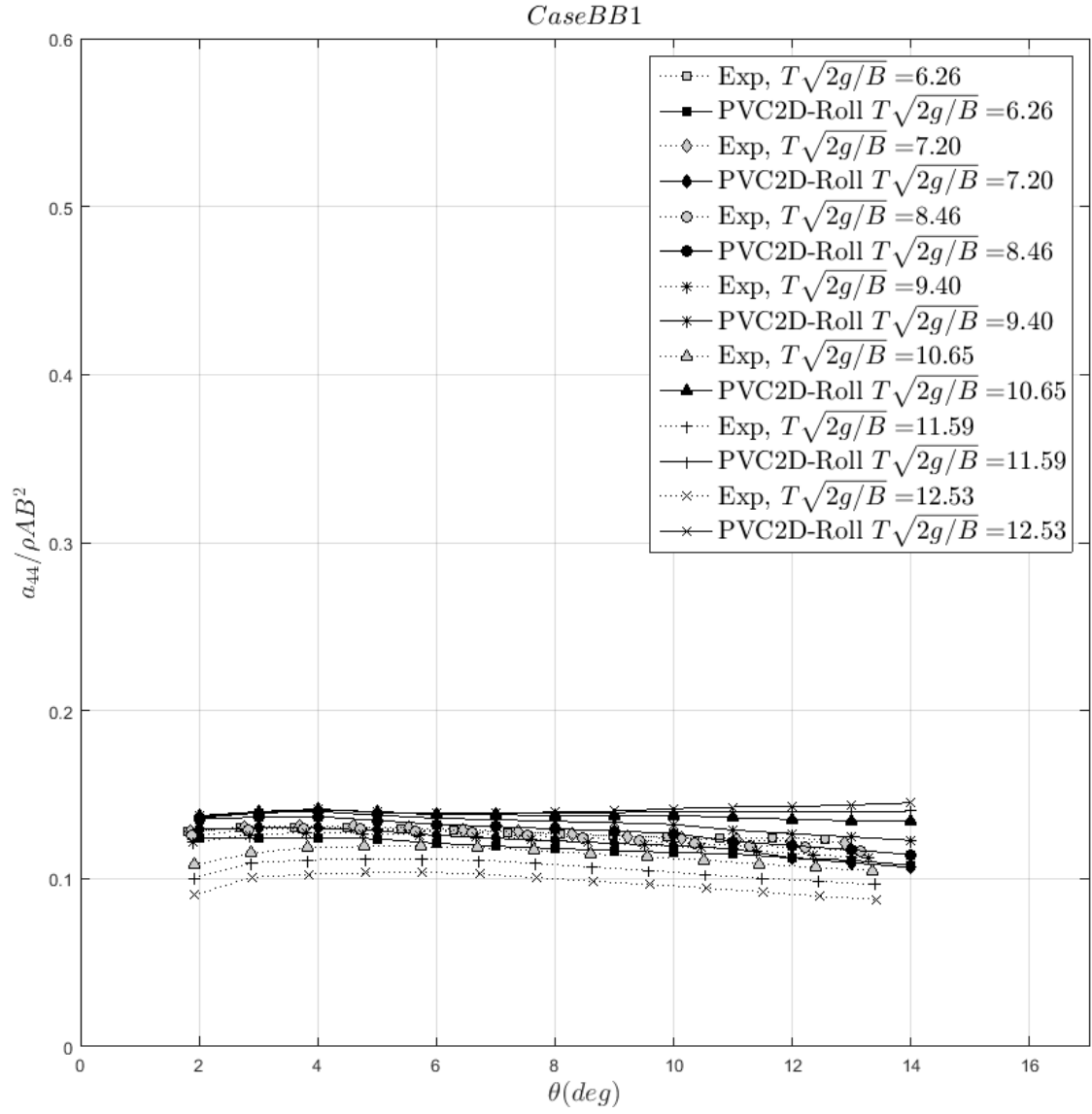
Figure C.5: Added-mass coefficients results for BB1 case with respect to amplitude increases
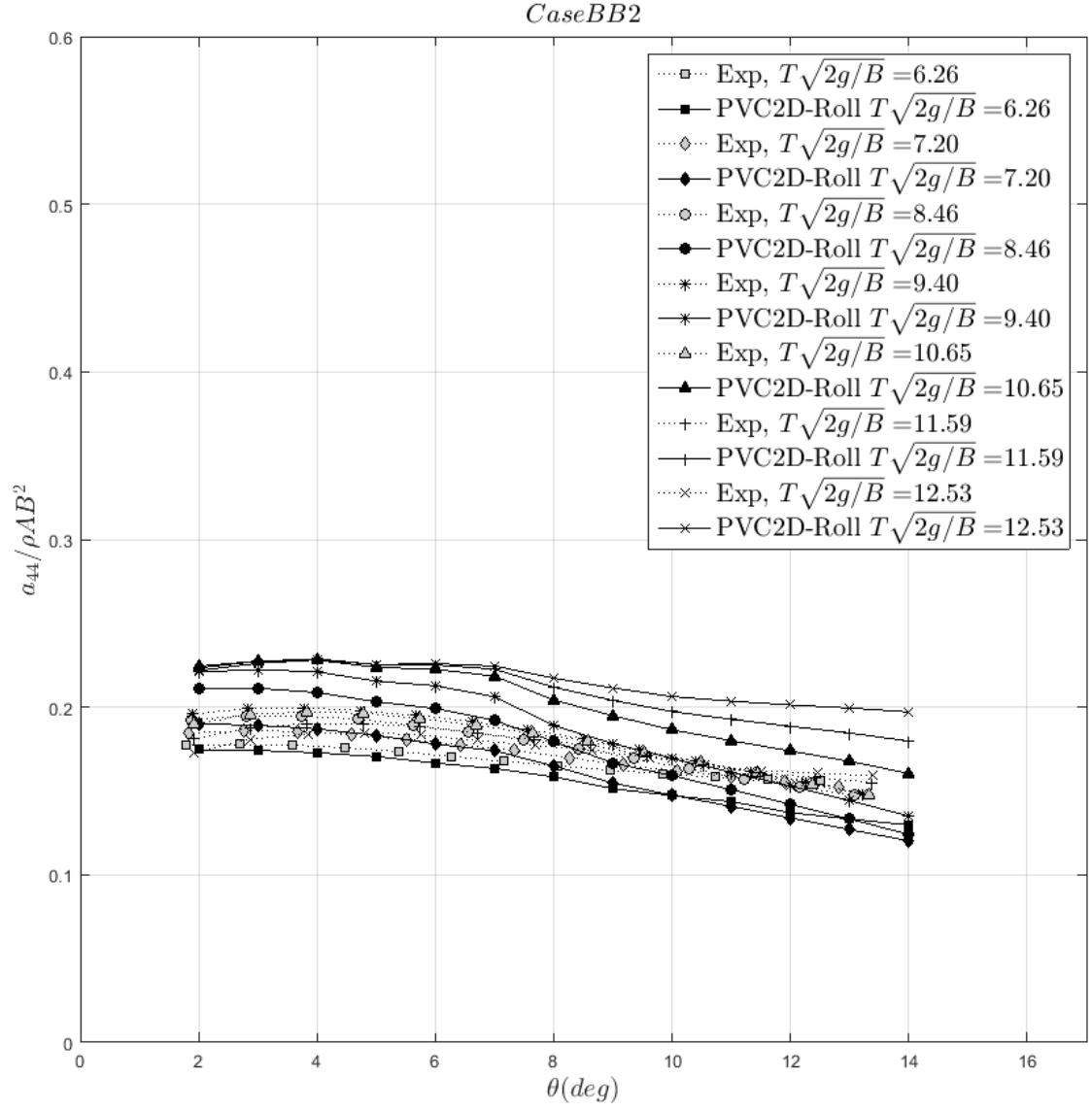
Figure C.6: Added-mass coefficients results for BB2 case with respect to amplitude increases

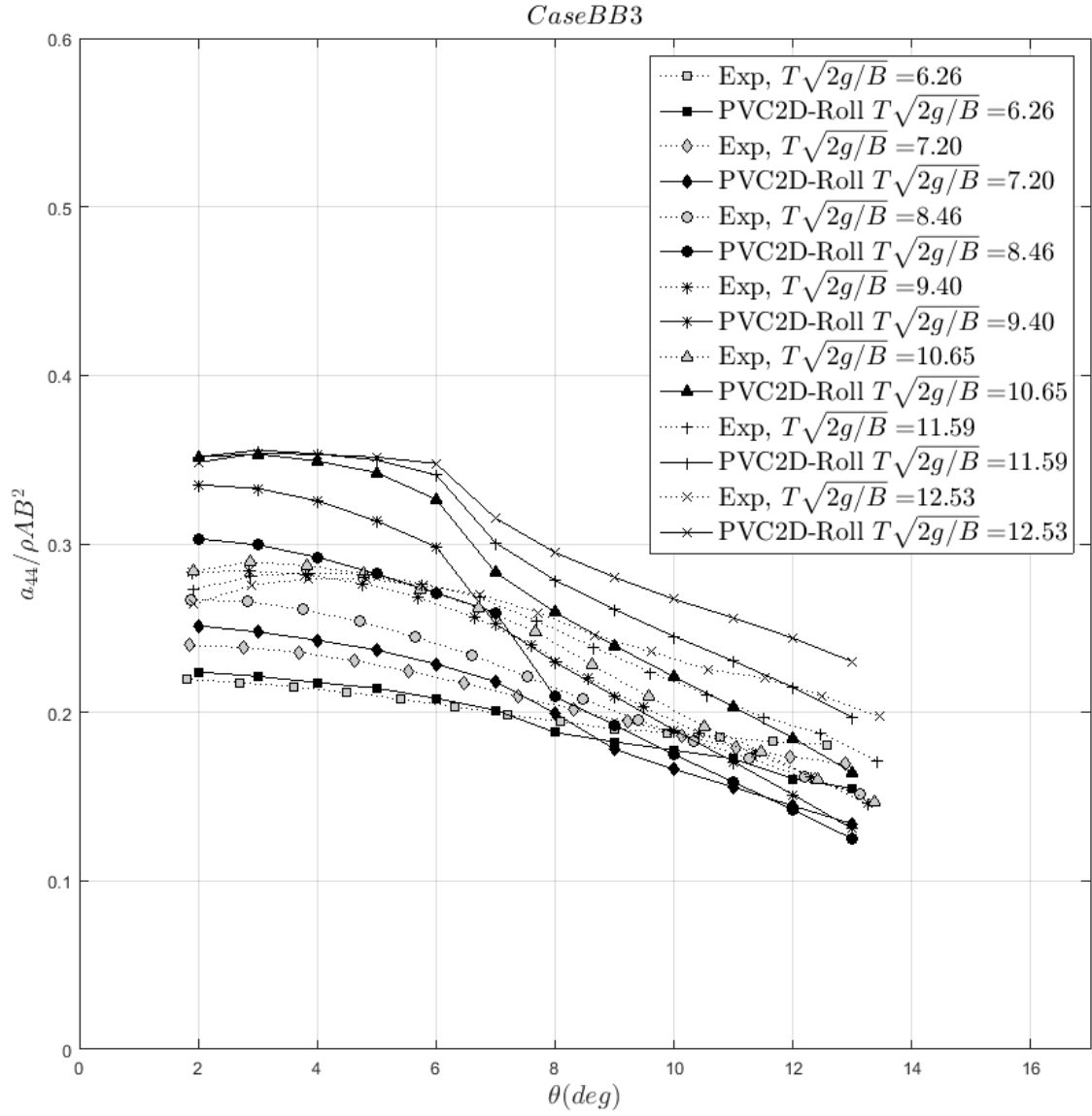Figure C.7: Added-mass coefficients results for BB3 case with respect to amplitude increases

Figure C.8: Added-mass coefficients results for RC0 case with respect to period of oscillations increases
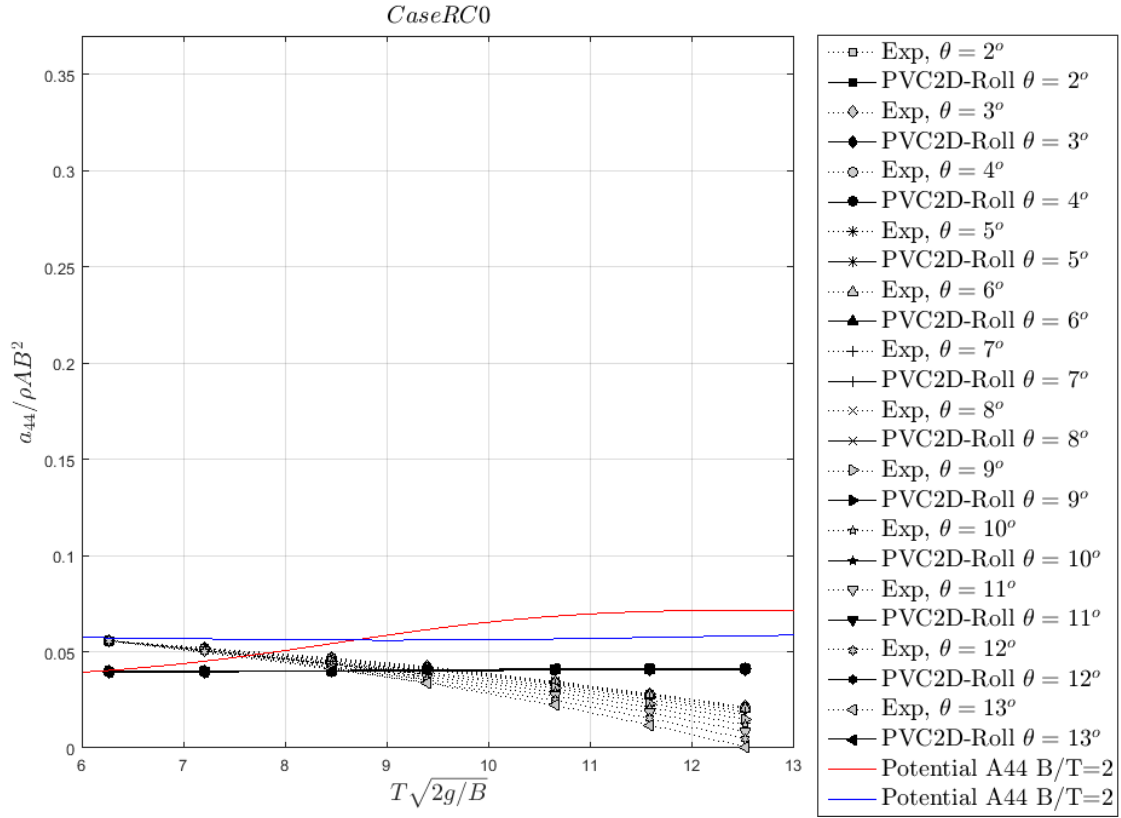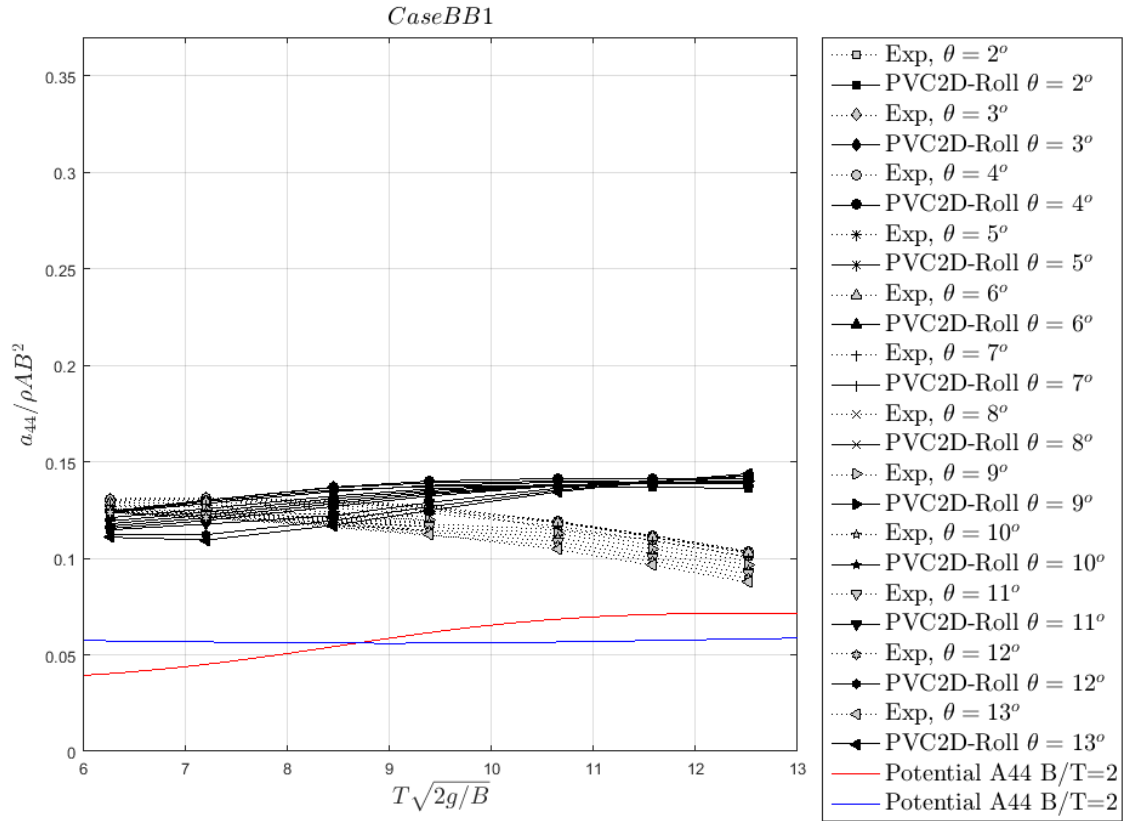
Figure C.9: Added-mass coefficients results for BB1 case with respect to period of oscillations increases
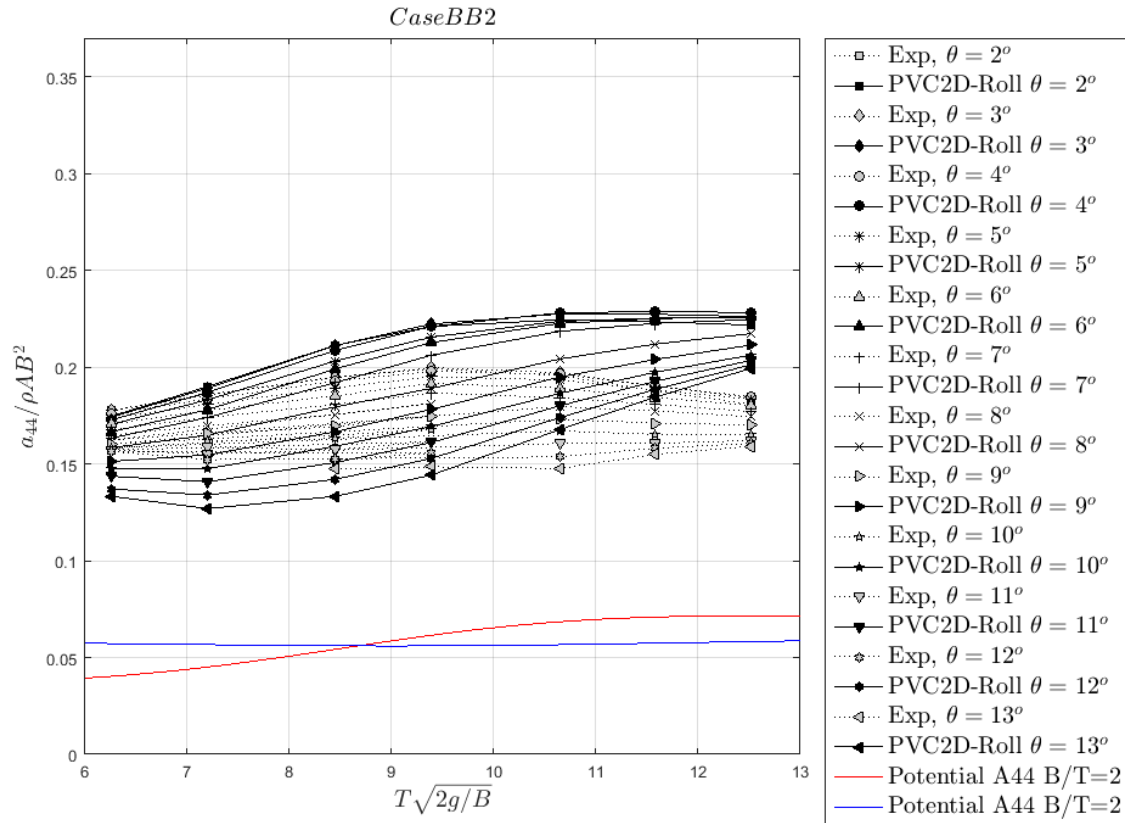
Figure C.10: Added-mass coefficients results for BB2 case with respect to period of oscillations increases

Figure C.11: Added-mass coefficients results for BB3 case with respect to period of oscillations increases

Appendix D

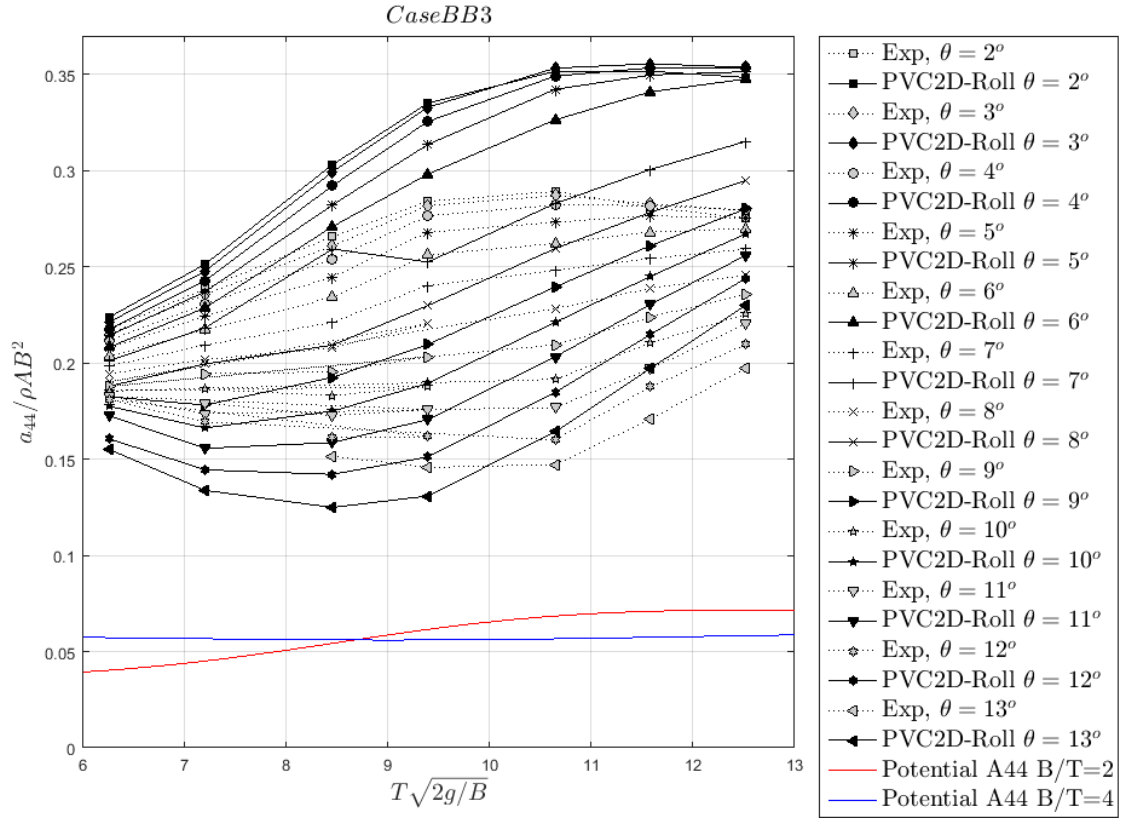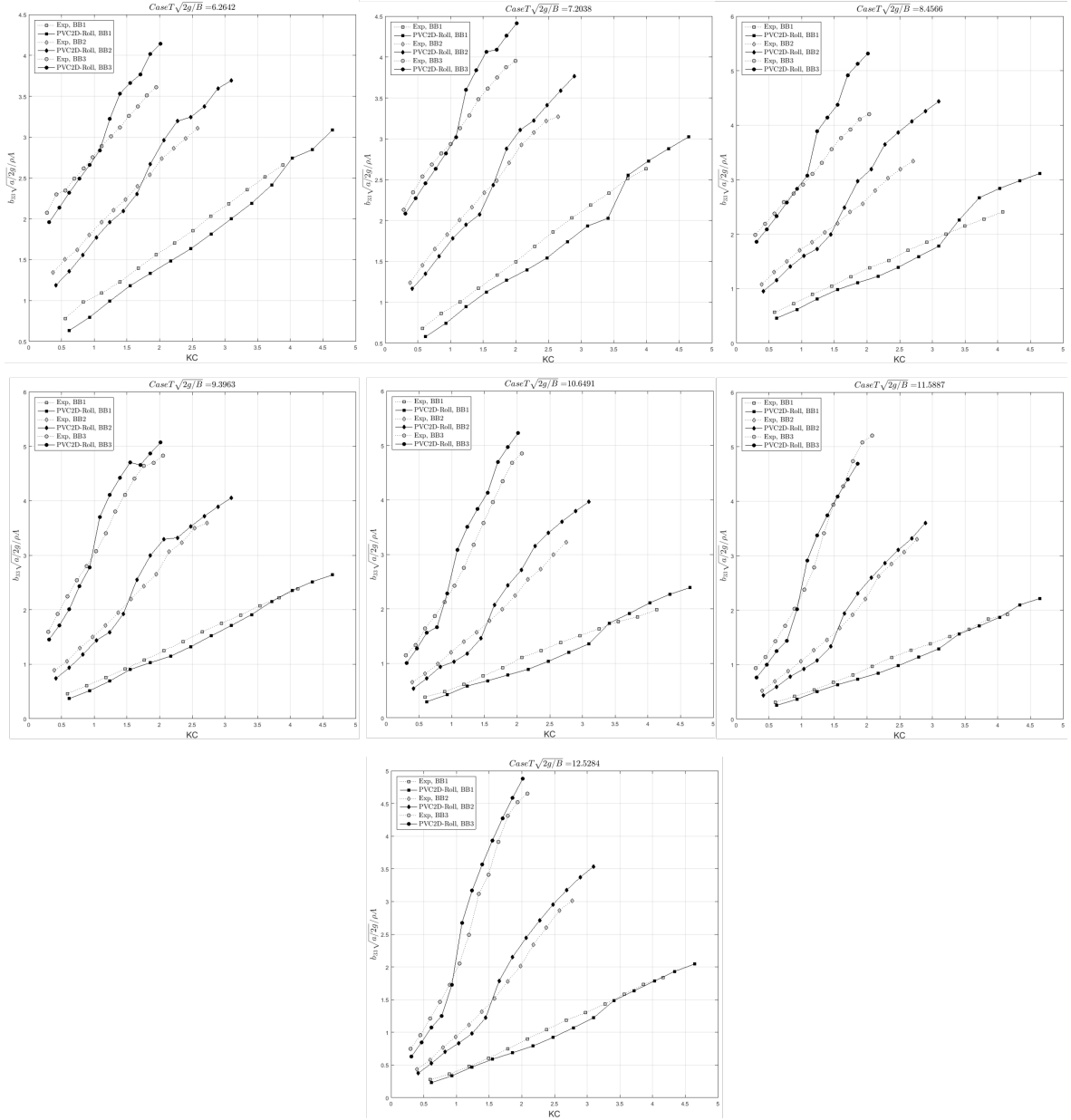# Bilge-Boxes Damping and Added-Mass Coefficients Results

Figure D.1: Damping coefficients results for varying bilge-boxes length case with respect to KC-number
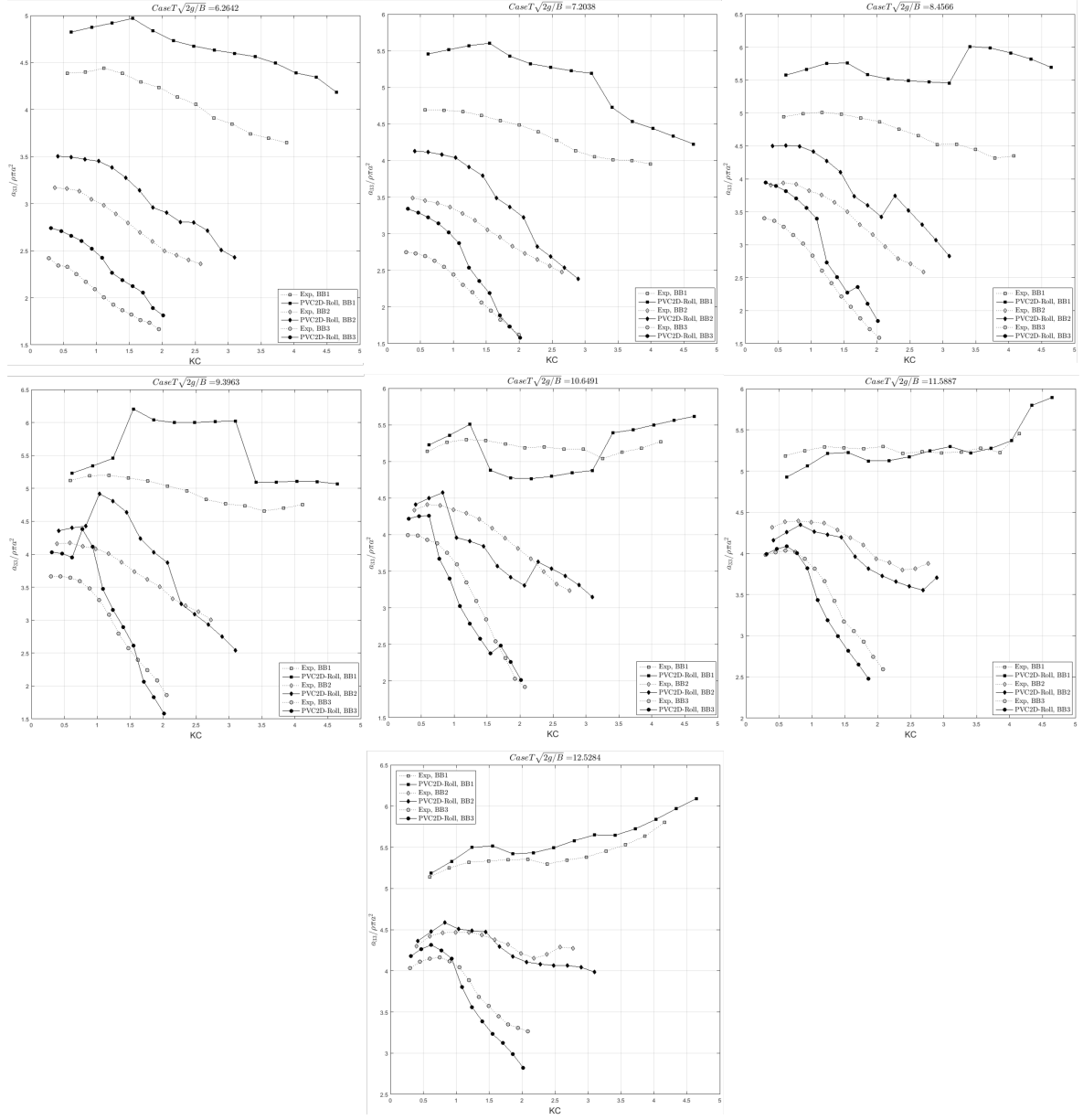
Figure D.2: Added-mass coefficients results for varying bilge-boxes length case with respect to KC-number

Bibliography

Bos, F. M. (2009). *Numerical simulations of flapping foil and wing aerodynamics*. PhD thesis, Technische Universiteit Delft.

Denis, M. S. and Pierson, W. J. (1953). On the motions of ships in confused seas. *The Society of Naval Architects and Marine Engineers*.

Falnes, J. (2002). *Ocean Waves and Oscillating Systems*. Cambridge University Press.

Faltinsen, O. and Pettersen, B. (1987). Application of a vortex tracking method to separated flow around marine structures. *Journal of Fluids and Structures*, 1(2):217–237.

Faltinsen, O. M. (1993). *Sea Loads on Ships and Offshore Structures*. Cambridge University Press.

Faltinsen, O. M. and Sortland, B. (1987). Slow drift eddy making damping of a ship. *Applied Ocean Research*, 9(1):37–46.

Faltinsen, O. M. and Timokha, A. N. (2009). *Sloshing*. CAMBRIDGE UNIV PR.

Ferziger, J. H. and Peric, M. (2001). *Computational Methods for Fluid Dynamics*. Springer-Verlag GmbH.

Fredriksen, A. G. (2015). *A numerical and experimental study of a two-dimensional body with moonpool in waves and current*. PhD thesis, Norwegian University of Science and Technology.

Froude, W. (1861). On the rolling of ships. *The Royal Institution of Naval Architects*, pages 247–249.

Gerritsma, J. (1958). An experimental analysis of shipmotions in longitudinal regular waves. Technical report, Netherlands Research Centre T.N.O. for Shipbuilding and Naviagation.

Greco, M. (2012). Tmr 4215 : Sea loads lecture notes.

Himeno, Y. (1981). Prediction of ship roll damping - a state of the art. Technical report, Naval Architecture & Marine Engineering, The University of Michigan.

Ikeda, Y., Himeno, Y., and Tanaka, N. (1976). On roll damping force of ship: Effects of friction of hull and normal force of bilge keels. *Journal of Kansai Society of Naval Architects.*

Ikeda, Y., Himeno, Y., and Tanaka, N. (1977a). On eddy making component of roll damping force on naked hull. *Journal of the Society of Naval Architects of Japan*, 1977(142):54–64.

Ikeda, Y., Himeno, Y., and Tanaka, N. (1978). A prediction method for ship roll damping. *Report of Department of Naval Architecture.*

Ikeda, Y., Komatsu, K., Himeno, Y., and Tanaka, N. (1977b). On roll damping force of ship - effect of hull surface pressure created by bilge keels. In *On Roll Damping Force of Ship -Effects of Hull Surface Pressure Created by Bilge Keels.*

Irkal, M. A. R., Nallayarasu, S., and Bhattacharyya, S. K. (2016). Cfd approach to roll damping of ship with bilge keel with experimental validation. In *Applied Ocean Research 55 (2016).* Elsevier.

Jaouen, F., Koop, A., and Vaz, G. (2011). Predicting roll added mass and damping of a ship hull section using cfd. In *Proceedings of the ASME 2011 30th International Conference on Ocean, Offshore and Arctic Engineering OMAE2011.*

Jasak, H. (1996). *Error Analysis and Estimation for the Finite Volume Method with Applications to Fluid Flows.* PhD thesis, Imperial College of Science, Technology and Medicine.

Journée, J. and Massie, W. (2001). Offshore hydromechanics. First Edition.

Keaney, I. (2015). *Evanescent Wave Reduction Using a Segmented Wavemaker in a Two Dimensional Wave Tank.* PhD thesis, National University of Ireland Maynooth.

Keulegan, G. and Carpenter, L. (1958). Forces on cylinders and plates in an oscillating fluid. *Journal of Research of the National Bureau of Standards*, 60(5):423.

Korvin-Kroukovsky, B. and Jacobs, W. R. (1955). Pitching and heaving motions of a ship in regular waves. *The Society of Naval Architects and Marine Engineers.*

Kristiansen, T. (2009). *Two-Dimensional Numerical and Experimental Studies of Piston-mode Resonance.* PhD thesis, Norwegian University of Science and Technology.

Kristiansen, T. and Faltinsen, O. M. (2012). Gap resonance analyzed by a new domain-decomposition method combining potential and viscous flow. *Applied Ocean Research*, 34:198–208.

Kristiansen, T., Ruth, E., Firoozkoohi, R., Borgen, H., and Berge, B. O. (2014). Experimental and numerical investigation of ship roll damping with and without bilge keels. In *Volume 1B: Offshore Technology.* ASME International.

Kristiansen, T., Sauder, T., Firoozkoohi, R., and Beretti, M. (2013). Validation of a hybrid code combining potential and viscous flow with application to 3d moonpool. In *32nd International Conference on Offshore Mechanics and Arctic Engineering (OMAE 2013)*. ASME International.

Martinussen, P. M. (2011). Parametric roll resonance of a fishing vessel as function of forward speed and sea state. Master's thesis, Norwegian University of Science and Technology.

Moreno, J., Thiagarajan, K. P., and Cameron, M. (2016). Hydrodynamic coefficients of hexagonal heave plates for floating offshore wind turbine platforms.

Newland, D. E. (2005). *An Introduction to Random Vibrations, Spectral & Wavelet Analysis: Third Edition*. DOVER PUBN INC.

Newman, J. N. (1977). *Marine Hydrodynamics*. MIT University Press Group Ltd.

Ommani, B., Fonseca, N., Kristiansen, T., Hutchison, C., and Bakksjø, H. (2016a). Bilge keel induced roll damping of an fpso with sponsons. In *Proceedings of the ASME 2016 35th International Conference on Ocean, Offshore and Arctic Engineering OMAE2016*.

Ommani, B., Kristiansen, T., and Faltinsen, O. M. (2016b). Simplified CFD modeling for bilge keel force and hull pressure distribution on a rotating cylinder. *Applied Ocean Research*, 58:253–265.

Ommani, B., Kristiansen, T., and Firoozkoohi, R. (2015). Nonlinear roll damping, a numerical parameter study. In *Proceedings of the Twenty-fifth (2015) International Ocean and Polar Engineering Conference (ISOPE)*.

Patankar, S. and Baliga, B. (1981). *Numerical heat transfer and fluid flow*. Hemisphere Publishing Corporation.

Salvesen, N., Tuck, E., and Faltinsen, O. (1970). Ship motions and sea loads. *The Society of Naval Architects and Marine Engineers*.

Sarpkaya, T. and O'Keefe, J. L. (1996). Oscillating flow about two and three-dimensional bilge keels. *Journal of Offshore Mechanics and Arctic Engineering*, 118(1):1.

Sarpkaya, T. and Shoaff, R. (1979). A discrete-vortex analysis of flow about stationary and transversely oscillating circular cylinders. In on Climate Change, I. P., editor, *Technical Report NPS-69 SL 79011*, pages 1–30. Naval Postgraduate School Monterey, California.

Shao, Y. (2010). *Numerical Potential-Flow Studies on Weakly-Nonlinear Wave-Body Interactions with/without Small Forward Speeds*. PhD thesis, Norwegian University of Science and Technology.

Shao, Y.-L., You, J., and Glomnes, E. B. (2016). Stochastic linearization and its application in motion analysis of cylindrical floating structure with bilge box. In *Proceedings of the 35th International Conference on Ocean, Offshore and Arctic Engineering*.

Tao, L. and Thiagarajan, K. (2003). Low kc flow regimes of oscillating sharp edges. ii. hydrodynamic forces. In *Applied Ocean Research 25 (2003) 53–62.*

Tasai, F. (1959). On the damping force and added mass of ships heaving and pitching. *Journal of Zosen Kiokai*, 1959(105):47–56.

Thiagarajan, K. P. and Braddock, E. C. (2010). Influence of bilge keel width on the roll damping of fpso. In *Journal of Offshore Mechanics and Arctic Engineering.*

Ursell, F. (1949). On the heaving motion of a circular cylinder on the surface of a fluid. *The Quarterly Journal of Mechanics and Applied Mathematics*, 2(2):218–231.

van't Veer, R., Schut, X., and Huijsmans, R. (2015). Bilge keel loads and hull pressures created by bilge keels fitted to a rotating cylinder. *Applied Ocean Research*, 53:1–14.

Vugts, I. J. H. (1968). The hydrodynamic coefficients for swaying, heaving and rolling cylinders in a free surface.

Vugts, J. H. (1970). *The hydrodynamic forces and ship motions in waves: De hydrodynamische krachten en scheepsbewegingen in golven.* Uitgeverij Waltman.

White, F. (2010). *Fluid Mechanics (Mcgraw-Hill Series in Mechanical Engineering).* McGraw-Hill Science/Engineering/Math.

White, F. M. (2005). *Viscous Fluid Flow.* McGraw-Hill Education Ltd.

Yeung, R., Roddier, D., Alessandrini, B., Gentaz, L., and Liao, S.-W. (2001). On roll hydrodynamics of cylinders fitted with bilge keels. *Twenty-Third Symposium on Naval Hydrodynamics.*

Yeung, R. W., Cermelli, C., and Liao, S. W. (1996). Vorticity fields due to rolling bodies in a free surface - experiment and theory. In *Twenty-First Symposium on Naval Hydrodynamics.*

Yeung, R. W., Liao, S. W., and Roddier, D. (1998). On roll hydrodynamics of rectangular cylinders. In *Proceedings of the Eighth (1998) International Offshore and Polar Engineering Conference.*

Yu, Y.-H., Kinnas, S. A., Vinayan, V., and Kacham, B. K. (2005). Modeling of flow around fpso hull sections subject to roll motions: Effect of the separated flow around bilge keels. International Society of Offshore and Polar Engineers.

Yuck, R. H., Lee, D. H., and Choi, H. S. (2003). A study on roll damping of 2-d cylinders. In *International Journal of Offshore and Polar Engineering.*